Organic Electronics on Fibers for Energy Conversion Applications

by

BRENDAN T. O'CONNOR

A dissertation submitted in partial fulfillment
of the requirements for the degree of
Doctor of Philosophy
(Mechanical Engineering)
in The University of Michigan
2009

Doctoral Committee:

Assistant Professor Kevin P. Pipe, Co-Chair
Assistant Professor Max Shtein, Co-Chair
Professor Peter F. Green
Assistant Professor Pramod Sangi Reddy

ACKNOWLEDGEMENTS

Foremost I would like to thank my advisors Max Shtein and Kevin P. Pipe. Their intelligence, creativity, and work ethic have been an inspiration. Max Shtein has been an invaluable resource in developing and interpreting successful experiments, and getting at the heart of a scientific problem. Kevin Pipe has also been a tremendous resource providing great advice that lead to many creative solutions to overcome research hurdles and elucidate interesting physics. I am forever indebted to them for taking me on as a research assistant and putting in a tremendous amount of effort to ensure my success. I would also like to thank the valued input from my other dissertation committee members Peter Green and Pramod Reddy.

I am also indebted to the many fellow students that I have worked with over the course of my doctoral studies who have provided fruitful discussions, an *enjoyable* work environment, and assistance with research including: Kwang Hyup An, Andrea Bianchini, Shaurjo Biswas, Peter Burgardt, Paddy Chan, Xi Chen, Chelsea Haughn, Steven Morris, Denis Nothern, Abhishek Yadav, Yiying Zhao, and many others. I would like to especially thank Xi Chen for her support throughout my PhD, helping me through many stressful days. To Yiying Zhao for getting me up to speed quickly in organic electronics research while having incredible patience. To Kwang Hyup An, who has been a great resource for questions pertaining to organic electronic device physics, and optics. To Xiangchun Zhang, who helped me through a very tough first year, and whose intelligence is only surpassed by his kindness.

Finally this thesis is dedicated to my parents Jeremiah and Joan O'Connor. Their love, support, and encouragement throughout my studies have made this thesis possible.

PREFACE

The work presented in this thesis aims to demonstrate and understand in detail novel organic optoelectronic device architectures: solar cells and light emitting devices on fibers. In carrying out the work on fiber-based devices, two additional contributions are made to the general field of organic photovoltaic (OPV) devices: the successful application of thin metal films as semitransparent electrodes to replace costly and brittle indium tin oxide, and the application of external dielectric coatings to improve the efficiency of OPV cells. The experimental work presented here is underpinned by self-consistent optical and electrical models that enable quantitative and predictive analysis of organic optoelectronic device performance. These models are used to guide the development of the fiber-based solar cells and light emitters to improve energy conversion efficiency, manufacturability, and versatility.

TABLE OF CONTENTS

CHAPTER

LIST OF TABLES

LIST OF FIGURES

LIST OF APPENDICES

LIST OF ABBREVIATIONS

BHJ	Bulk heterojunction
CRI	Color rendering index
DA	Donor – acceptor interface
EBL	Exciton blocking layer
FF	fill factor
FWHM	Full width half maximum
HID	High intensity discharge
HOMO	Highest occupied molecular orbital
ITO	Indium tin oxide
j_{SC}	short circuit current density
LCD	Liquid crystal display
LED	Light emitting device
L_D	Exciton diffusion length
LUMO	Lowest unoccupied molecular orbital
OPV	Organic photovoltaic
OLED	Organic light emitting device
PHJ	Planar heterojunction
RGB	Red-green-blue
RMS	Root mean square
SSL	Solid state lighting
V_{OC}	open circuit voltage
VTE	Vacuum thermal evaporator
η_{EQE}	external quantum efficiency
η_{IQE}	internal quantum efficiency
η_{IQE}’	modified internal quantum efficiency

Chemicals

PCBM	[6,6]-phenyl-C61-butyric acid methyl ester
P3HT	poly(3-hexylthiophene)
PEDOT:PSS	poly(styrene sulfonate)
CuPc	Copper Phthalocyanine
C60	Buckminsterfullerene
BCP	bathocuproine
Alq_3	aluminum hydroxiquinoline
NPD	N,N'-di-1-naphthyl-N,N'-diphenyl-1,1'-biphenyl-4,4'diamine
LiF	Lithium fluoride
PtOEP	Pt(III) Octaethylporphine
m-MTDATA	4,4’,4”-tris-(3-methylphenylphenylamino)triphenylamine

ABSTRACT

Currently, there is great demand for pollution-free and renewable sources of electricity. Solar cells are particularly attractive from the standpoint of sunlight abundance. However, truly widespread adoption of solar cells is impeded by the high cost and poor scalability of existing technologies. For example, while 53,000 mi^2 of 10% efficient solar cell modules would be required to supply the current U.S. energy demand, only about 50 mi^2 have been installed *worldwide*. Organic semiconductors potentially offer a route to realizing low-cost solar cell modules, but currently suffer from low conversion efficiency. For organic-based solar cells to become commercially viable, further research is required to improve device performance, develop scalable manufacturing methods, and reduce installation costs via, for example, novel device form factors.

This thesis makes several contributions to the field of organic solar cells, including the replacement of costly and brittle indium tin oxide (ITO) electrodes by inexpensive and malleable, thin metal films, and the application of external dielectric coatings to improve power conversion efficiency. Furthermore, we show that devices with non-planar geometries (e.g. organic solar cells deposited onto long fibers) can have higher efficiencies than conventional planar devices. Building on these results, we demonstrate novel fiber-based organic light emitting devices (OLEDs) that offer substantially improved color quality and manufacturability as a next-generation solid-

state lighting technology. An intriguing possibility afforded by the fiber-based device architectures is the ability to integrate energy conversion and lighting functionalities with textiles, a mature, commodity-scale technology.

Specific technical contributions described in the text include:

- A metal-organic-metal solar cell structure with efficiency comparable to conventional ITO-based devices (O'Connor, 2008a)
- Utilization of coherent light trapping in organic solar cells via external dielectric coatings, shown to be particularly beneficial when applied to the metal-organic-metal structures (O'Connor, 2006; O’Connor, in preparation)
- Modeling and experimental demonstration of fiber-based organic photovoltaic devices that can outperform their planar counterparts under diffuse illumination (O'Connor, 2008b)
- Modeling of light trapping in fiber device bundles, with optimized structures showing large predicted improvements in efficiency over conventional devices on ITO-glass substrates (O’Connor, in preparation)
- Modeling of bundles of narrow-band absorbing fibers, with color dispersion inherent to the bundle architecture that could increase the overall solar energy conversion efficiency (O’Connor, in preparation).
- Modeling and experimental demonstration of fiber-based OLEDs with directionally invariant electroluminescence spectra, particularly suitable for lighting applications (O'Connor, 2007).

CHAPTER 1

INTRODUCTION

1.1 Introduction

This chapter serves to motivate the pursuit of optoelectronic devices in the form of fibers for energy conversion applications, and also to motivate organic semiconductors as a particularly advantageous material basis to realize such devices. The current challenges of solar electric generation and solid-state lighting are first discussed, followed by a review of previously demonstrated electrically functional fibers and textiles. Organic optoelectronic devices (e.g. organic photovoltaic cells – OPVs, and organic light emitting devices – OLEDs) are then introduced. The discussion in this chapter is not meant to be an exhaustive review of these topics but rather it is intended to provide sufficient context for the work described in the remainder of the thesis.

1.2 The demand for novel solar cells and solid-state lighting sources

The global primary energy demand is currently 15 TW on average, of which the average energy demand in the U.S. exceeds 3.3 TW (Lewis N., 2007). This energy is largely derived from unsustainable fossil fuel sources, with renewable sources, in particular solar electricity, supplying a very small fraction (<0.1%) of the overall energy mix. However, the sun is an enormous energy resource ($\sim 1.2 \times 10^5$

TW/yr (Lewis N., 2007) and harnessing its energy with solar cells provides an opportunity to cleanly and sustainably meet a substantial portion of our energy needs.

While solar cells with conversion efficiency greater than 20% are already available in the marketplace, existing devices are far from being cost-effective, as shown in **Fig. 1.1**. Considerable demand therefore exists for new, low-cost solar cell technologies, among which organic-based photovoltaic (OPV) cells offer promise. The principles of operation and state-of-the-art for PV and OPV devices will be reviewed in greater detail in **Sections 1.2.1** and **1.2.2**, and in **Chapter 2**.

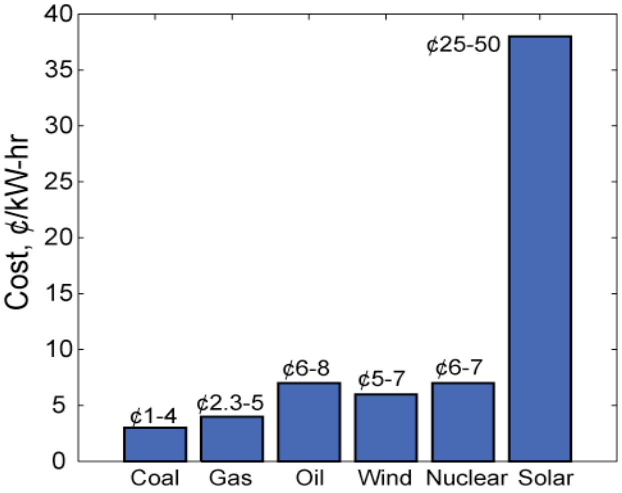

Figure 1.1. The production cost of electricity from the major fuel resources (Adapted from Lewis N., 2007).

In addition to providing efficient and cost-effective solutions for energy supply, it is important to develop technologies to mitigate the growing energy demand. One major use of primary fossil fuel energy is in generating electricity for lighting, which makes up over 20% of the U.S electricity demand (So et al., 2008). Area lighting based on organic LEDs has the potential to be cost-effective and efficient, achieving relatively high color rendering index (CRI) while also attaining efficiency rivaling that of fluorescent lighting. However, commercial implementation and widespread adoption of OLEDs for lighting require substantial further progress to be made in CRI, power efficiency, and manufacturing cost. The current status and challenges facing OLEDs for solid-state lighting (SSL) applications are discussed in **Section 1.2.4** and revisited in **Chapter 7**.

1.2.1 Current status of solar energy technologies

The record efficiencies of various solar cell technologies certified by the National Renewable Energy Lab over the past 30 years are provided in **Fig. 1.2**. The highest efficiencies are achieved in solar cells that are multi-junction devices, using semiconductors with multiple band gaps that allow the solar cell to absorb a greater portion of the solar spectrum than a solar cell with a single band gap. However, these devices are typically reserved for space applications or solar concentrator modules due to the very high cost of the cell itself. Over 90% of all commercial solar cells on the market are based on silicon, but the cost of electricity produced by these devices is significantly higher than that produced using fossil fuels. As a result, deployment is very limited; the total installed solar electricity capacity in the U.S. is 1,000 times smaller that what is needed to meet the energy demand, as illustrated in **Fig. 1.3**. The prohibitive cost of electricity generated by current solar cell technologies is the main driver in the search for an alternative solar cell technology.

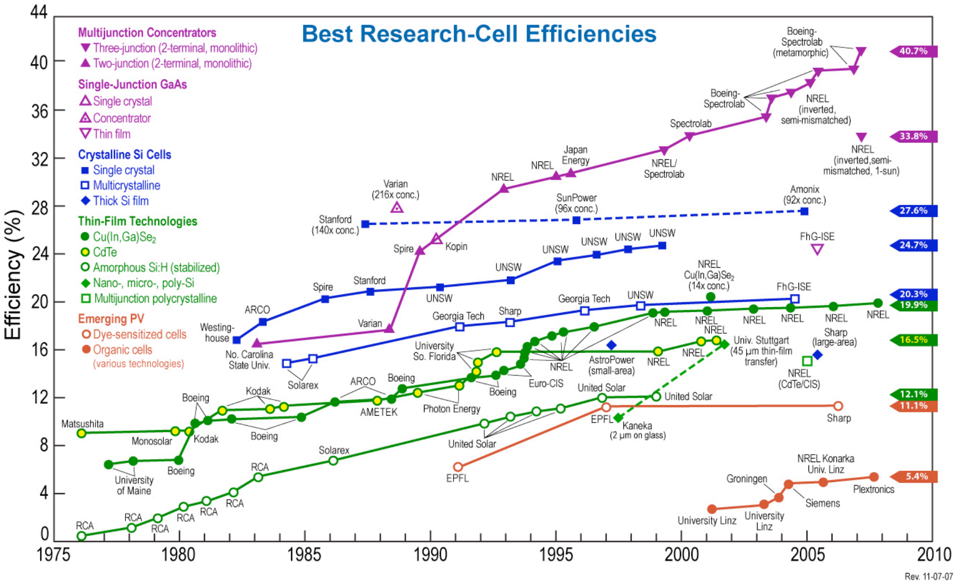

Figure 1.2. The best research-cell efficiencies that have been verified by the National Renewable Energy Research Laboratory (NREL) as of November 2007 (Kazmerski et al., 2007).

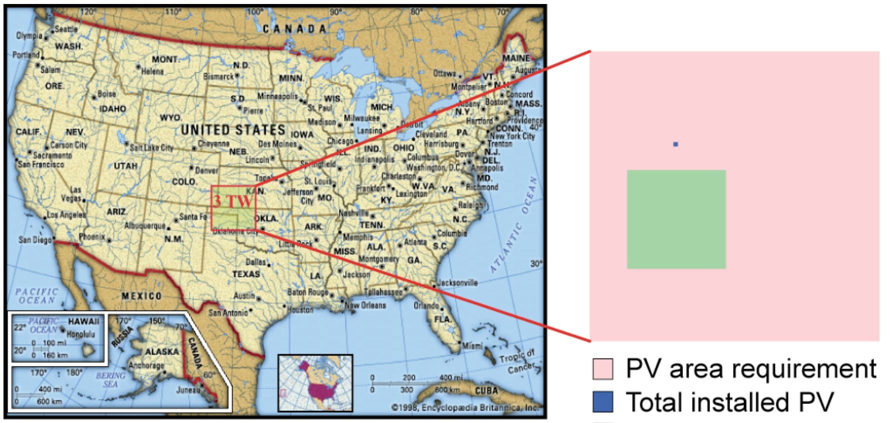

Prof. Nate Lewis (Caltech)

Figure 1.3. At left, a schematic view of the land requirement needed to meet the U.S. primary energy demand of 3 TW with solar cell modules that are 10% efficient (Lewis N., 2007). At right, a comparison of this area requirement with the total area of installed photovoltaics to date in the U.S. and our country's annual textile imports (Anderson K., 2008).

1.2.2 Organic solar cell technology and challenges

Organic solar cells have promise as a low-cost alternative to current solar cell technologies. Conjugated small molecular or polymeric semiconductors (examples in

Fig. 1.4) are of particular interest because they absorb light very strongly, are easily synthesized, and are ubiquitous in low-cost pigments (e.g. plants, colored plastics, etc.). Furthermore, because organic thin films can be rapidly deposited with high optical quality on virtually any kind of substrate without regard for lattice matching, such devices could in principle be manufactured using low-cost fabrication techniques.

In the development of organic solar cells, two main branches of technology have been pusued: devices based on polymers and devices based on small molecular active layers. For polymer-based OPV cells, the highest reported power efficiencies to date have reached 5.6% for a single junction cell and 6.5% for a tandem cell configuration (Kim et al., 2007). For small molecular OPV devices, the best reported in the literature have reached 4.2% (Xue et al., 2004), with over 6% claimed commercially by Heliatek Inc. (Germany). These efficiencies have been achieved through intensive research over the past 20 years, when interest in organic solar cells was renewed after Tang et al. demonstrated a landmark 1% efficient planar-heterojunction organic solar cell in 1986 (Tang, 1986). The performance and structure of this cell are shown in **Fig. 1.5** (The principles of organic solar cell operation are discussed in detail in **Chapter 2**.)

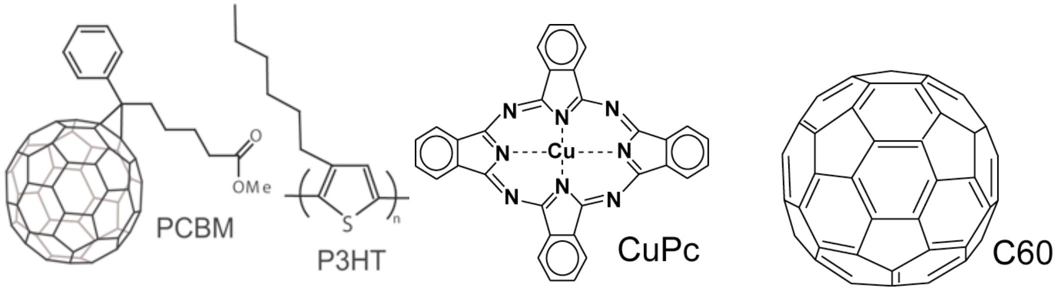

Figure 1.4. Polymeric and small molecular and semiconductors commonly used in organic solar cells. From left, PCBM is [6,6]-phenyl-C61-butyric acid methyl ester, P3HT is poly(3-hexylthiophene), CuPc is copper phthalocyanine, and C60 is Buckminsterfullerene.

It is likely that for organic solar cells to become economically viable, power efficiencies of at least 10% will be required in a scalable production process that yields operational lifetimes exceeding 10 years (Forrest, 2005). In this work, the focus is on small molecular organic PV cells, proposing and demonstrating proof-of-principle devices that can help lower device costs and improve power conversion efficiency.

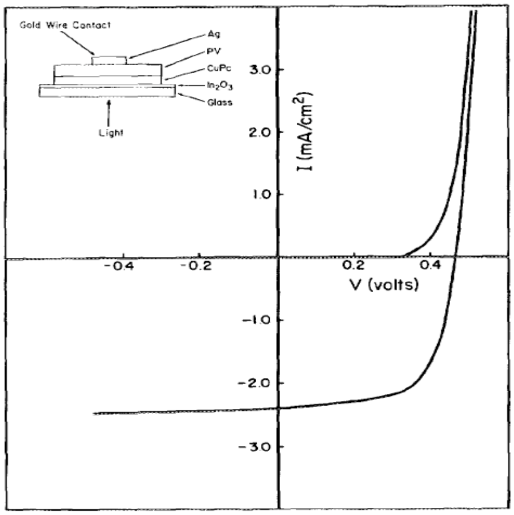

Figure 1.5. Current-voltage relationship for a planar-heterojunction solar cell demonstrated by Tang in 1986. The structure of the cell is shown in the inset and consisted of a glass substrate followed by ITO, 25 nm CuPc, 45 nm parylene tetracarboxylic derivative (PV) and roughly 60 nm of Ag (Tang, 1986).

1.2.3 Current status of solid-state lighting

There are three lighting technologies that currently dominate the market: incandescent, fluorescent, and high intensity discharge (HID) lamps. The market share in terms of energy consumption from these technologies is given in **Fig. 1.6**. In 1879 Thomas Edison developed the first incandescent lamp, which lasted approximately 100 hours with an efficacy of 1.4 lm/W (Navigant Consulting Inc., 2009). Over time, the efficacy of these lamps has increased to 15 lm/W with a lifetime of approximately 1,000 hours. Today, incandescent lamps dominate residential lighting and make up one-quarter of commercial lighting. HID lamps have efficacies that range from 45-150 lm/W depending on lamp type and wattage. These lamps are capable of being very bright yet suffer from poor light quality, limiting their implementation being limited to outdoor, industrial, and suitable commercial applications. Fluorescent lamps currently have efficacies ranging from 65-100 lm/W and much longer operational lifetimes than incandescent bulbs; and fluorescent lights have been adopted widely in commercial lighting applications (i.e. office buildings, factory floors, etc.). Adoption in the residential sector has been substantially limited, however, due to high purchase costs and poor light rendering quality compared with incandescent lamps (i.e. CRI < 65 vs. CRI = 100). Here the CRI is the color rendering index, which is a quantitative measurement of how well a light source is able to reproduce colors of objects as compared to a reference (ideal) light source.

These three dominant lighting technologies have developed over the past 40 years or more, and significant further gains in performance are not expected (Navigant Consulting Inc., 2009). Instead, industry analysts predict that LED and

OLED-based solid-state lighting (SSL) can improve today's lighting efficiency by a factor of two or more (Navigant Consulting Inc., 2009).

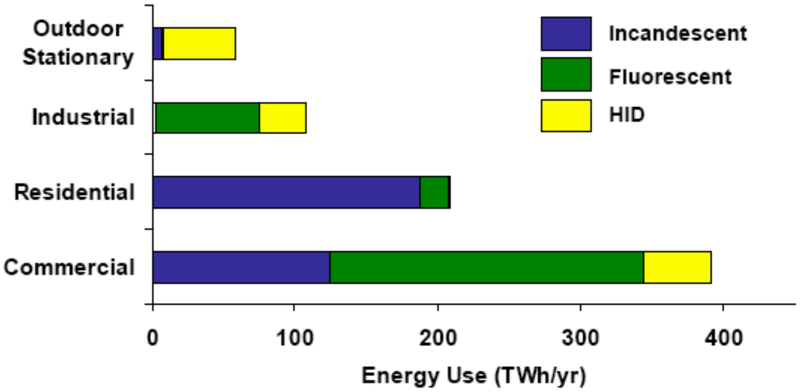

Figure 1.6. Lighting energy consumption in the U.S. by sector and source (Navigant Consulting Inc., 2009).

1.2.4 Organic light emitting device technology and challenges

Organic light emitting devices (OLEDs) are actively being commercialized in flat-panel displays as replacements for LCD technology. OLEDs have many unique properties that make them attractive not only for displays but also for SSL applications. Organic semiconductors can be synthesized with electroluminescent properties tailored for a specific application. Combinations of red, green, and blue emitters, for example, can produce a high CRI at power efficiencies which meet or exceed those achieved by rival technologies (e.g. fluorescent, incandescent, or inorganic LEDs), as shown in **Fig. 1.7** (Navigant Consulting Inc., 2009).

To achieve broad commercialization of OLEDs for SSL, there is a need to develop high luminance OLEDs with improved operational lifetimes, and methods for low-cost manufacturing (So et al., 2008). In this work, fiber-based OLEDs are demonstrated as a potential method to lower manufacturing costs and improve luminance.

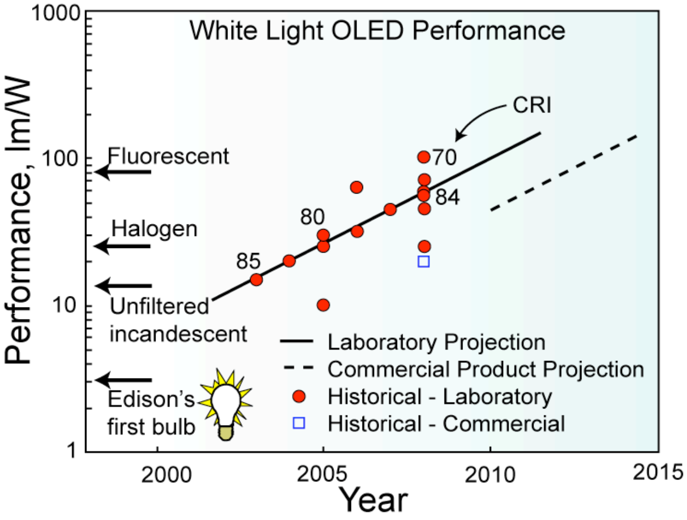

Figure 1.7. The performance of white light OLEDs, with other technologies listed at left. Reproduced from Navigant Consulting Inc., 2009.

1.3 Fiber and textile electronics

Historically, textiles have been used for protection from the surrounding environment, comfort, and artistic expression. The oldest known woven material dates back 27,000 years; since then, fibers and textiles have continually made scientific and engineering advancements that have made them a ubiquitous part of society (Schoeser, 2003). Today, textiles are integrated into all aspects of our daily life in applications ranging from the mundane (e.g. clothing, drapes, rugs, and seat covers) to the specialized (e.g. woven carbon fibers in aircraft such as the Airbus A380). More recently, *smart textiles* have been engineered to sense, react to, and show enhanced physical characteristics under specific environmental conditions, as well as incorporate electronic functionality.

Electro-active textiles can be divided into two technological approaches, top-down and bottom-up. A top-down approach takes existing electronic components and embeds them into a textile (Marculescu et al., 2003; Park, Jayaraman, 2003; Schubert, Werner, 2006), while a bottom-up method designs electronic function into the individual fibers that make up the textile (Bayindir et al., 2004; Yadav et al., 2008; Lee, Subramanian, 2005). An example of a top-down approach is shown in **Fig. 1.8**, with LEDs embedded into textiles. An example of a bottom-up approach is shown in **Fig. 1.9**, with individual photodetecting fibers woven into a light detecting fabric (Bayindir et al., 2004). Top-down electronic textiles are currently required for certain application (e.g. computation where transistor speed is critical), however the bottom-up approach allows for seamless integration of electronics into textiles.

Figure 1.8. Demonstrations of Phillips' light emitting Lumalive® fabric. Low-cost LEDs are laminated onto a durable and flexible plastic panel and then embedded beneath the surface of textiles (Harold P., 2006).

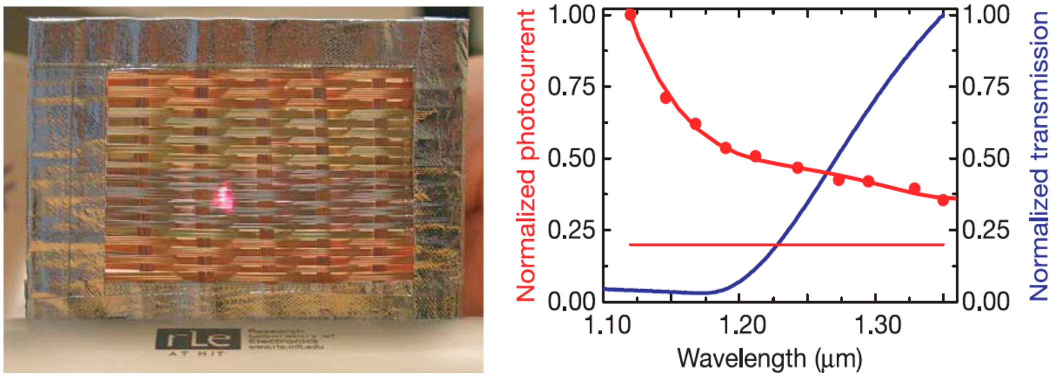

Figure 1.9. Left, demonstration of a bottom-up photodetecting fabric, made from pulled fiber photodetectors having a metal-insulator-semiconductor structure. Right, the normalized photocurrent of an 890 μm diameter fiber. The horizontal red line indicates the dark current level (Bayindir et al., 2004).

Here, our focus is on bottom-up approaches for developing optoelectronic textiles, which have many applications for not only smart textiles but also integration in structural composites and optical communications systems. Recent developments in electronic fibers for energy applications include batteries (Wang et al., 2006), piezoelectrics (Qin et al., 2008), solar cells (Liu et al., 2007; O'Connor et al., 2008b), photodetectors (Bayindir et al., 2004), and thermoelectrics (Yadav et al., 2008).

In particular, the past 3 years has seen considerable development of fiber-shaped solar cells including proof-of-concept devices based on silicon, organic semiconductors, and dye-sensitized technologies. Polycrystalline silicon solar cells deposited using chemical vapor deposition onto glass substrates were fabricated with a power conversion efficiency of 1.35% under specific illumination directions (Kuraseko et al., 2006). Images of the devices along with performance characteristics are given in **Fig. 1.9**. A solution-processed dye-sensitized solar cell fiber was demonstrated with an estimated power conversion efficiency of approximately 0.19% (Fan et al., 2008). A viewgraph of this device is given in **Fig. 1.10**, showing a Cu wire counterelectrode twisted together with a dye-sensitized and CuI-coated working electrode. Lui et al. demonstrated a fiber-based organic solar cell with solution-coated active polymer layers on a silica fiber with an indium tin oxide anode and Al cathode (2007). In this design, light is coupled into the silica fiber core and then outward into the active layers of the device, as illustrated in **Fig. 1.11**. In our work, on the other hand, organic solar cells described in this work were deposited using vacuum thermal evaporation onto polyimide coated silica fibers, with light incident upon the cell normal to the fiber length, as discussed at length in **Chapter 5** (O'Connor et al., 2008b). Finally, there has been a recent demonstration of a solution-coated polymer solar cell fiber with the structure illustrated in **Fig 1.12**. This most recent work features an encapsulated active fiber with consistent device performance over long lengths of fiber and a reported efficiency of between 2.79 – 3.27%; this reported efficiency, however, overestimated device efficiency by a factor of 2.5 or greater (Lee et al., 2009). While the above discussion shows that a considerable body of work exists in the realm of fiber-based solar cells, little quantitative work has been published on the understanding of how these devices operate, what limits their efficiency, and to what extent their performance can be improved. This thesis attempts to fill this gap by providing a more sound quality basis for understanding and further evolving fiber-based device performance.

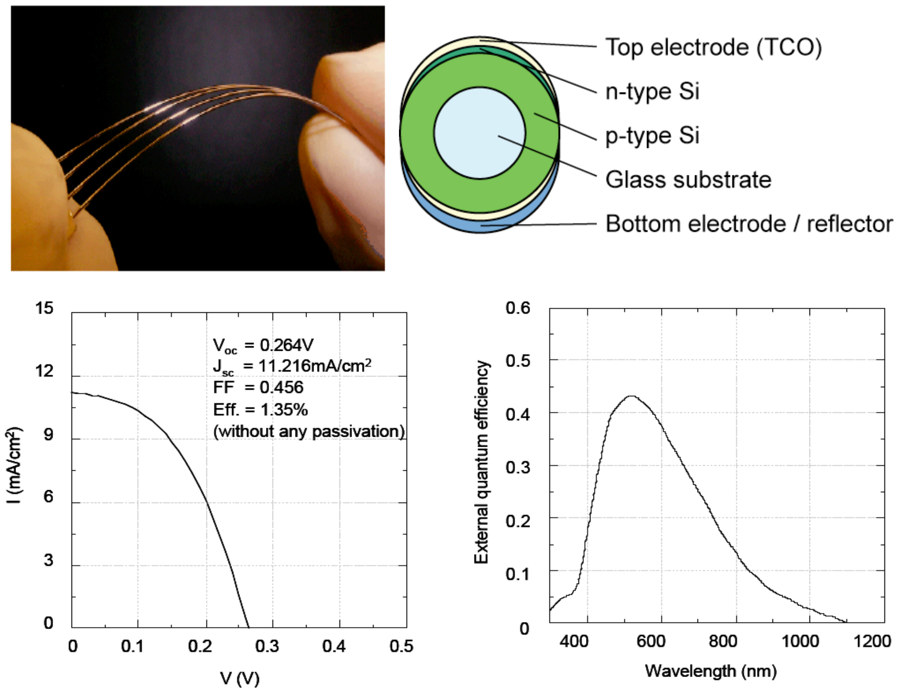

Figure 1.10. Top left, photograph of polycrystalline silicon based solar cell. Top right, an illustration of the fiber structure. Bottom left, the current voltage relationship for the fiber PV cells. Bottom right, the external quantum efficiency (Kuraseko et al., 2006).

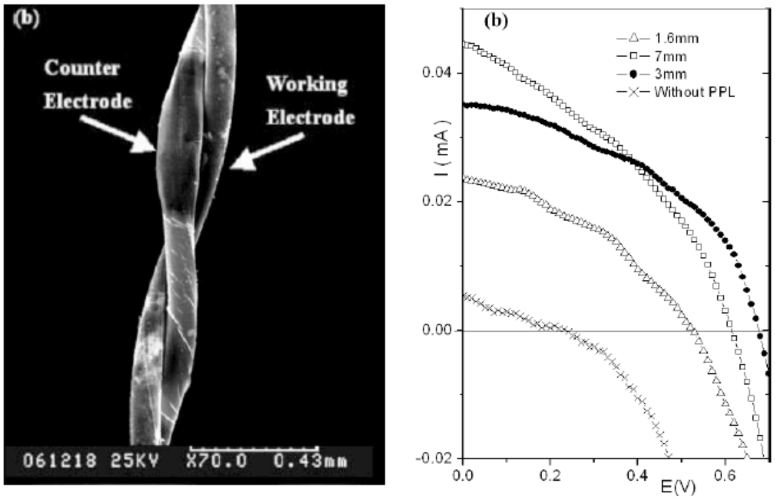

Figure 1.11. Demonstration of a wire-shaped dye sensitized solar cell. At left, SEM image of the wire consisting of a Cu wire counterelectrode twisted together with a dye-sensitized and CuI-coated working electrode. At right, current voltage relationship for cells with varying electrode screw pitch-length (Fan et al., 2008).

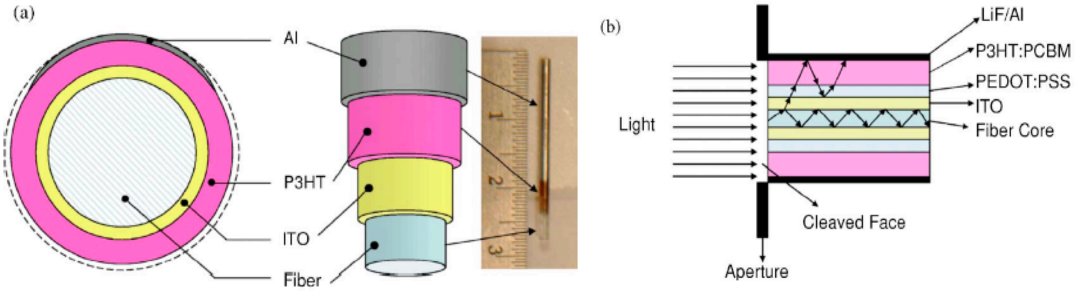

Figure 1.12. (a) Structure of a polymer based fiber solar cell structure demonstrated by Liu et. al. (b) Schematic view of how light interacts with the fiber PV (Liu et al., 2007).

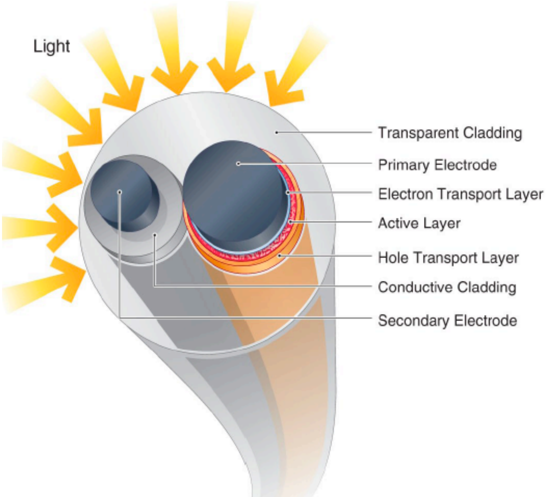

Figure 1.13. Illustration of the device structure of a recent organic solar cell fiber based on polymeric active layers. The active solar cell layers are solution coated on one fiber, with a counter electrode then wrapped around the initial fiber to complete the circuit. The entire fiber is then encapsulated in a transparent cladding (Lee et al., 2009).

There has been considerably less work in the development of fiber-based light-emitting devices. Fiber based organic light-emitting devices (OLEDs) are of interest due to their wide range of potential applications from fabric-integrated light sources to low cost solid-state lighting. The fiber geometry provides an opportunity for low-cost red-green-blue (RGB) lighting technology that replaces expensive lithography techniques by placing individual RGB light sources in close proximity to one another to generate white light in the far field. Additionally, schemes to couple light from a device on the exterior of an optical fiber into its core may find applications in optical communications and microscopy. The work presented here is the first (to our knowledge) demonstration of fiber-based organic light-emitting devices. RGB fiber OLEDs are demonstrated with detailed device characterization in **Chapter 7**.

1.4 Organization of the thesis

The chapters composing this thesis follow a progression of concepts that address challenges facing OPVs and OLEDs. A set of questions is provided below to outline this progression and motivate the individual chapters.

How do OPV cells work, and which parameters limit their performance?

Chapter 2 reviews the principal concepts of organic solar cell operation. Within this chapter an optoelectronic model is outlined that assists in understanding device performance and aids in new device designs. This model is used throughout the text to examine the replacement of indium tin oxide (ITO) with thin metal films (**Chapter 3**), design external coatings to improve device performance (**Chapter 4**), and assist with understanding of fiber-based OPV (**Chapter 6**).

Why replace indium tin oxide in OPV cells and why use thin metal films?

Electrodes are required in solar cells to transport charge to bus-lines and subsequently to an external circuit. In thin-film OPV devices, continuous electrodes are necessary due to the limited electrical conductivity of the adjacent organic semiconductors. One of these electrodes must also effectively couple incident light into the active layers. To date, the most widely employed transparent electrode has been indium tin oxide (ITO). However, ITO has significant shortcomings for low-cost and large-area device applications, including the rising cost of indium, brittleness, the need for high growth temperature, and indium diffusion that may degrade device performance (Fortunato et al., 2007). In **Chapter 3**, these challenges are addressed by replacing ITO with a non-patterned thin metal film. This ability to use non-patterned metal films as transparent electrodes potentially offers a number of advantages, including compatibility with low-cost roll-to-roll fabrication (Bishop, 2007), low-temperature processing (Fortunato et al., 2007), the ability to deposit on non-planar substrates (O'Connor et al., 2008b), and improved mechanical flexibility (Lewis et al., 2004). General guidelines for metallic electrode design are provided, and an OPV cell deposited onto a silver anode is shown to achieve parity with an analogous cell deposited onto ITO.

Why haven't others used thin metal films as electrodes more often?

Transparent conductor materials are typically chosen for conductivity and far-field transmission over the visible spectrum, and even metal films that are very thin suffer from lower far-field transmission than ITO. However, because they are very reflective, metals with certain optical constants can be chosen to engineer the optical intensity distribution within the organic layers to maximize efficiency. Some metals also offer good band alignment with adjacent organic layers, reducing barriers to charge transport. Finally, although light in-coupling is somewhat reduced when switching from ITO to thin metal films, applying external dielectric coatings to metal-electroded OPV cells can be very effective at improving light in-coupling efficiency and can yield device efficiencies greater than those with optimized ITO electrodes.

How do external dielectric coatings improve efficiency?

External dielectric coatings are very similar to anti-reflection coatings used in many optical applications. However, the optical analysis and coating design is more detailed; we must account for optical coherence in very thin OPV layers, and must optimize the optical field intensity distribution so that excitons are generated in favorable locations within the active organic layers. Additionally, the coating should be designed specifically to maximize the quantum efficiency of the solar cell and the resulting photocurrent, which makes these quantities a function of near-field rather than far-field optics. The design thus takes into account the specific organic solar cell structure and materials as well as the spectral distribution of solar radiation. This is the subject of **Chapter 4**.

For low-cost, low-efficiency applications, where organic PV surely fits, balance-of-system costs should be as low as possible. How should this be addressed?

The ability to fabricate semiconductor devices on a fiber substrate, coupled with the commodity scale of fiber and textile technology can have significant implications for realizing cost-effective, large-scale solar energy conversion devices. **Figure 1.3** compares the area of textiles annually imported into the U.S. with the total solar cell area required to meet our country's primary energy demand. These imported textiles only make up roughly 37% of all textiles purchased in the U.S. annually. Combining domestically produced textiles and imported textiles in one-year results in a nearly equivalent area of that required to meet our energy needs with solar energy (Anderson K., 2008). The ability to utilize this very large and mature industry provides an opportunity to scale up solar cell technology to the necessary area requirements.

When considering fiber-based photovoltaics specifically, organic semiconductors have several characteristics that make them an ideal material system. The archetypal OPV cell is on the order of 100 nm, which adds negligible thickness to a fiber substrate. Organic devices are inherently flexible and compatible with conformal textiles. Furthermore, organic solar cells have a very high power density and can add energy harvesting capability to a textile with minimal added weight. **Table 1.1** compares the typical power densities of organic solar cells with other commercially available solar cell technologies.

Table 1.1. Power density of several solar cell technologies under standard AM1.5G illumination conditions. Also compared is the power density of a typical jet engine (Data courtesy of Max Shtein, University of Michigan).

	Density, g/cm^2	Thickness, μm	η_p, %	Power Density, W/kg
Crystalline Si	2.3	100	25	1,000
GaInP/GaAs/Ge	5	5	30	10,000
Organic	2	0.2	6	130,000
Jet Engine	-	-	35	10,000

This concept is interesting, but what are the efficiencies that can be achieved for fiber-OPV devices?

The single-fiber OPV cell demonstrated in this dissertation exhibits roughly half the efficiency of the archetypal ITO-glass OPV cell under normal illumination. However, this very pessimistic finding quickly gives way to substantial efficiency, cost and utilization advantages when considering systems of fibers. The fiber geometry opens up unique opportunities to push efficiencies beyond those achieved with the glass-ITO structure. In particular, multi-fiber bundles can be designed to efficiently trap light, leading to large gains in short circuit current. Further gains are expected for a volumetric distribution of microcavity-tuned narrowband fiber PV cells. Here, individual fibers are designed to be very efficient over a narrow part of the solar spectrum. When multiple fibers of varying optimized optical bandwidths are combined in a volumetric system, the total system quantum efficiencies can be very high. This is the subject of **Chapter 6**.

How is this fiber concept useful for organic light-emitting devices as well?

Fiber-based organic light-emitting devices (OLEDs) are of interest for applications ranging from fabric-integrated light sources to low-cost solid-state lighting. The fiber geometry provides an opportunity for cost-effective white lighting based on separately optimized and subsequently assembled red-, green-, and blue-emitting (RGB) channels. Expensive lithography techniques can be avoided entirely by placing individual red-, green-, and blue-emiting OLED fibers in closely spaced arrays. In addition to lighting applications, optical communications and microscopy applications can benefit from OLEDs on fibers that couple light into the fiber core. **Chapter 7** provides a sound physical understanding of the impact that the fiber geometry has on device performance.

The relationships between the main topics discussed in this work are illustrated graphically in **Fig. 1.14**. For example, the development of multi-fiber OPV systems in **Chapter 6** uses the device designs of the fiber OPV cell demonstrated in **Chapter 5** and the external dielectric coating designs of **Chapter 4**. The fiber-based OPV cells in **Chapter 5** use a thin metal electrode film, which is the topic of

Chapter 3. As previously mentioned, the optical and carrier transport models outlined in **Chapter 2** are used throughout to study and predict OPV performance.

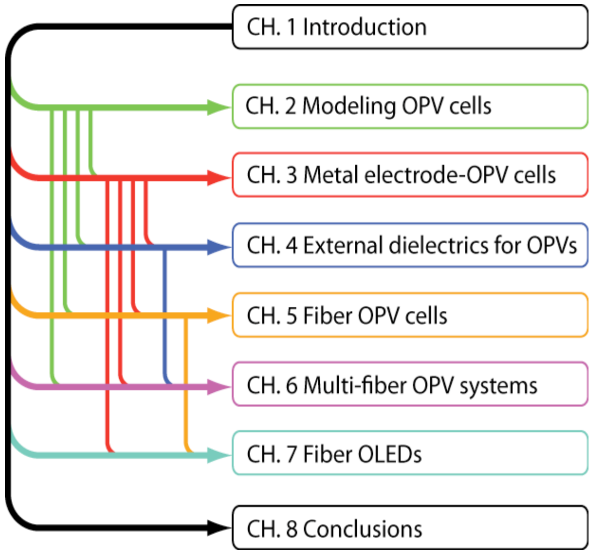

Figure 1.14. The layout of the thesis, illustrating the progression and interconnections between chapters.

CHAPTER 2

MODELING ORGANIC SOLAR CELL PERFORMANCE

2.1 Introduction and motivation

This chapter focuses on predicting the performance of organic photovoltaic cells using a combination of optical and exciton transport models. The emphasis is on the behavior of incident light within the device layers, namely the optical field intensity distribution versus wavelength and position for an arbitrary combination of optical constants and layer thicknesses. The diffusion and dissociation of excitons, which are still actively researched and debated processes, are treated here phenomenologically by assimilating the relevant parameters from experimental results available from our lab and the literature. From an analysis of the optical behavior of a given OPV device, performance limitations of the device structure and constituent materials can be ascertained, assisting in device design and optimization.

Because basic optical modeling of organic solar cells has been previously treated in some detail, it will be reviewed only briefly here (Peumans, et al., 2003b; Petterson, et al., 1999). A relatively novel aspect of the models discussed here is the generalization of the relevant physics to include incident illumination angle. In addition, absorption within the constituent materials is visualized in a way that helps clarify how incident solar energy is partitioned within the solar cell. An analysis of the variables that dominate conversion efficiency is presented and limitations of the model are discussed.

2.2 Organic photovoltaic efficiency

Photovoltaic cells convert energy from light into electrical current with an electronic potential that can drive an external load. The details of this conversion process for an organic solar cell are illustrated in **Fig. 2.1**. The seven processes illustrated in **Fig. 2.1** start with photon absorption (Step 1) followed by excited state relaxation of the electron-hole pair forming an exciton (Step 2). The second process releases energy through phonon emission. Phonon emission during free carrier relaxation is a major source of heating in solar cells made from inorganic materials such as silicon; however, the limited energy bandwidth of allowed states in organic semiconductors reduces the photon absorption energy band to closely match the bandgap of the organic semiconductor, leading to a relatively smaller amount of phonon emission. The generated exciton is a neutral quasi-particle that exhibits lifetimes ranging from nanoseconds to micro- and milliseconds (Shao, Yang, 2005). As an exciton diffuses, it can recombine (i.e. decay) through photon or phonon emission (Step 3). If the exciton diffuses to the interface between the donor and acceptor layer (Step 4), it will dissociate into free charges (Step 5), provided there exists a net thermodynamic driving force for forming the charge-separated state, and provided the transition to free charges overcomes the Coulombic binding energy of the exciton, which can range between 0.1 and 2 eV (Peumans, Forrest, 2004). Finally, the free charges diffuse to the electrodes where they are collected (Step 7). This process typically involves further energy losses though bulk Joule heating (phonon emission) and also depends on the interface resistance between the organic layer and the electrode, as discussed in further detail in **Chapter 3**. The free charges may also recombine before being extracted from the device due to several possible mechanisms including impurity trap states (Step 6).

Below, the definitions of power conversion efficiency and quantum efficiency of organic solar cells are briefly explained.

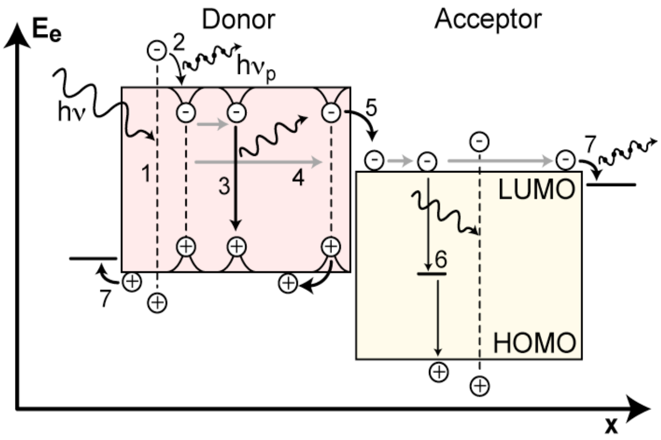

Figure 2.1. Energy band diagram of the organic layers in an organic photovoltaic cell showing the basic processes involved in converting incident light into electrical energy.

Power efficiency and the current-voltage relationship

The power conversion efficiency (η_p) is obtained from the current-voltage relationship of the solar cell, and is defined as follows:

$$\eta_p = \frac{j_{SC}V_{OC}FF}{P_{inc}} = \frac{j_{\max}V_{\max}}{P_{inc}} \tag{2.1}$$

Here P_{inc} is the incident optical power density, j_{SC} is the short circuit current density, V_{OC} is the open circuit voltage, and FF is the fill factor. **Figure 2.2** shows a typical current-voltage relationship of a solar cell under illumination, highlighting the relevant parameters. The *FF* is defined as the ratio of the area of the largest rectangle that can be drawn within the *j-V* curve to the area defined by j_{SC} and V_{OC}. The solar irradiance is given in **Fig. 2.3** for standard AM1.5G conditions, and when integrated over all wavelengths gives $P_{inc} \approx 100$ mW/cm^2.

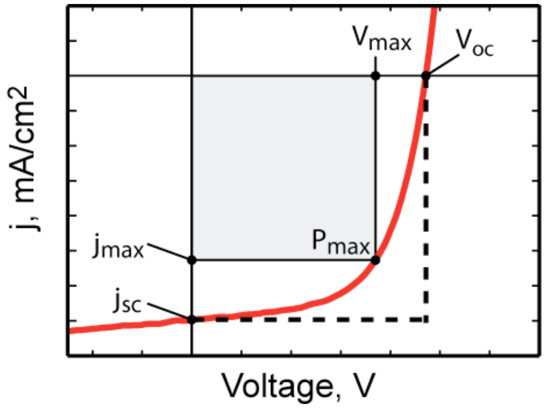

Figure 2.2. Typical current-voltage relationship of a solar cell under illumination. The fourth quadrant of the plot is power output from the cell with the maximum power output $P_{max}=V_{max}j_{max}$.

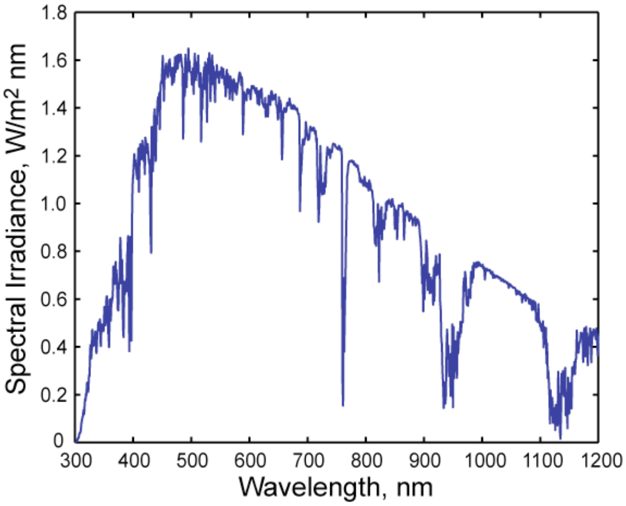

Figure 2.3. The standard AM1.5G solar irradiance spectrum over a limited range of wavelengths.(ASTM G-173-03)

External and internal quantum efficiency

The external quantum efficiency, η_{EQE}, is defined as the number of electrons collected by an external circuit divided by the number of photons incident upon the solar cell, and is usually given as a function of incident light wavelength. The external quantum efficiency can be further decomposed as follows:

(2.2) $$\eta_{EQE} = \eta_A \eta_{IQE} = \eta_A \eta_{ED} \eta_{CT} \eta_{CC}$$

where η_A is the absorption efficiency of incident light by the active organic layers and η_{IQE} is the internal quantum efficiency; the latter is defined as the number of electrons extracted per photon absorbed in the organic layers. The absorption efficiency is illustrated as Step 1 in **Fig. 2.1**. The internal quantum efficiency can be broken down into several steps: the exciton diffusion efficiency (η_{ED} ~ (1 - Step 3/Step 4)), the charge transfer efficiency (η_{CT} ~ Step 5), and the charge collection efficiency (η_{CC} ~ 1 - Step 6/Step 7). The loss mechanism for η_{CT} is geminate electron-hole pair recombination at the interface, which is not illustrated in **Fig. 2.1** (Peumans, Forrest, 2004). Of these processes, η_{CT} and η_{CC} have been shown to approach 100% for the small molecular heterojunction systems that are primarily discussed in this work (**Peumans et al., 2003b)**. This results in $\eta_{EQE} \approx \eta_A \eta_{ED}$.

Another way to define η_{EQE} is by a modified absorption efficiency, η_A', multiplied by a modified internal quantum efficiency: η_{IQE}': $\eta_{EQE} = \eta_A' \cdot \eta_{IQE}'$ where η_A' is defined as the total absorption by all layers of the photovoltaic cell (not just the active organic layers) and η_{IQE}' is the fraction of electrons collected for photon absorption by all cell layers. Defining η_{EQE} with these modified terms is useful for quantifying the effective utilization of reflected or transmitted light, and will be reviewed in more detail later in this chapter and applied in **Chapter 6**.

The short circuit current density (j_{SC}) is derived from the quantum efficiency via

(2.3) $$j_{SC} = q \int \eta_{EQE} S(\lambda) d\lambda,$$

where S(λ) is the wavelength-dependent photon flux.

Voltage and Fill Factor

Although the basic mechanisms that define V_{OC} are still not fully understood, it is generally agreed that it is limited by the difference between the LUMO level ($E_{L,A}$) of the acceptor materials and the HOMO level ($E_{L,D}$) of the donor materials (Riede et al., 2008). One model representation of the V_{OC} is (Cheyns et al., 2008a):

(2.4) $$qV_{OC} = |E_{L,A}| - |E_{H,D}| + BB_D + BB_A - \Delta\phi_A - \Delta\phi_D,$$

where q is electron charge, BB is the net band bending in the electrostatic potential, and $\Delta\phi$ is the energy offset at the contact, with subscripts A and D referring to the acceptor layer and donor layer, respectively. There are several other similar approaches used to predict V_{OC} which show good agreement with experimental results and are based on equivalent circuit models, self-consistent solutions to the Poisson and drift-diffusion equations, and Monte Carlo simulations (Riede et al., 2008).

The fill factor (FF) of an organic solar cell can be understood quantitatively by considering the classical diode equation that includes parasitic losses in the device from series resistance (R_S), shunt resistance (R_{SH}), and non-ideal diode behavior (m), this equation can be written as (Nelson, 2003):

(2.5) $$j = j_{SC} - j_o[\exp(q(V + jAR_S)/mk_B T) - 1] - \frac{V + jAR_S}{R_{SH}},$$

where j is the current density, A is the device area, k_B is the Boltzmann constant, and T is the absolute temperature. The losses in the equation reduce the overall power conversion efficiency, altering the maximum power point and *FF*.

2.3 Optical intensity distribution in organic solar cells

Charge transport in organic semiconductor films is typically slower than that in conventional inorganic semiconductors (e.g. Si or GaAs), but optical absorption is stronger (e.g. $\alpha_{\mathrm{Si}} \sim 5\times10^3$/cm, $\alpha_{\mathrm{Organics}} \sim 1\times10^5$/cm) (Peumans et al., 2003b; Nelson, 2003). Slow transport implies that the charge transport layers must be thin to maximize charge extraction efficiency. The strong absorptivity leads to the fact that a 500 nm thick organic film will often absorb nearly 100% of the incident photons within its absorption spectrum. Together, these factors limit the maximum practical thickness of the active layers in organic solar cells to be less than 200 nm. However, another restriction on optimum layer thicknesses exists due to the trade-off between light absorption and exciton transport. The absorptive layers should be thinner than twice the exciton diffusion length ($2L_D$) to ensure efficiency exciton dissociation*; for C60 and other organic semiconductors, L_D typically shorter than 40 nm. Given these general guidelines for practical layer thicknesses, a detailed electromagnetic wave analysis that models the optical intensity distribution inside the OPV can reveal powerful pathways for improving device performance.

---

* This has motivated the development of bulk-heterojunction organic solar cells that employ interdigitated organic layers. Modeling of these devices is discussed briefly in Chapter 3.

While incident sunlight is generally incoherent, the OPV layers are thinner than the sunlight's coherence length (~800 nm) (Hoppe, et al. 2003) and optical interference effects therefore arise. The optical field intensity $|E|^2$ can be determined as a function of position within the solar cell using a transfer matrix formulism. Transfer matrix calculations for thin films have been derived in detail by Heavens (1965), and applied to OPV devices by Petterson (1999) and Peumans (2003b). Techniques to determine the optical intensity distribution are reviewed here, closely following the work of Petterson with modifications to explicitly determine the optical intensity distribution as a function of illumination angle.

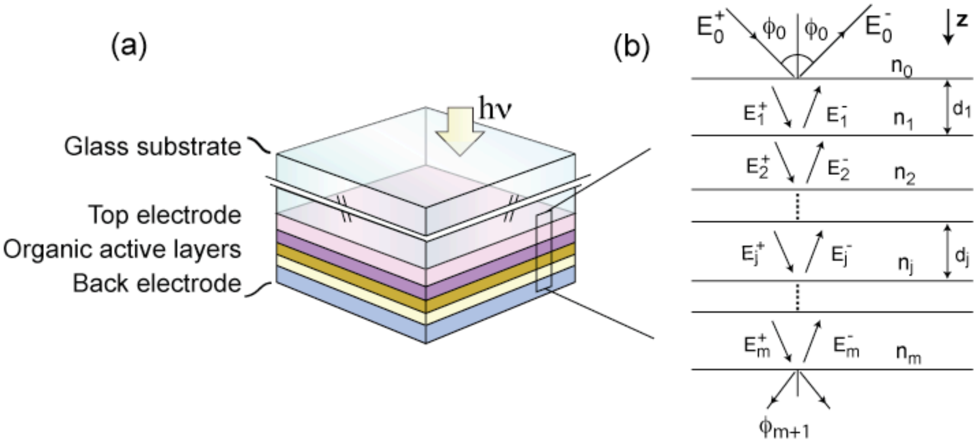

Figure 2.4. (a) A schematic of an organic solar cell on a glass substrate. (b) The geometry of a multi-layer stack (that may make up an organic solar cell). Layers 0 and m+1 are considered semi-infinite media. Each layer j (j = 1,2,…m+1) has a thickness d_j, and the optical field at any point in layer j is represented by two components: one propagating in the positive z direction and one in the negative z direction, E_j^+ and E_j^- respectively. Figure adapted from Heavens, 1965.

For simplicity, we assume homogeneous and isotropic material properties described by a complex index of refraction $\tilde{n} = n + ik$. The interfaces between layers are assumed to be optically flat, and light is modeled as an electromagnetic plane wave. Reflection and transmission at critical interfaces is determined by applying boundary conditions to the solutions of Maxwell's equations; the boundary conditions require that the tangential components of both the electric and magnetic vectors be continuous across the boundary in question.

Within the multilayer stack, the optical field at any point can be decomposed into two components, one propagating in the positive *z* direction and one propagating in the negative *z* direction. As illustrated in **Fig. 2.4b**, at position *z* in layer *j* these fields are denoted by $E_j^+(z)$ and $E_j^-(z)$. To define these forward and backward propagating waves across a boundary from layer *j* to layer *k*, we calculate an interface matrix,

$$I_{jk} = \frac{1}{t_{jk}} \begin{bmatrix} 1 & r_{jk} \\ r_{jk} & 1 \end{bmatrix}. \tag{2.6}$$

with *r* and *t* being the Fresnel reflection and transmission coefficients. These coefficients depend on polarization, and for *s*-polarized light are given by:

$$r_{jk} = \frac{q_j - q_k}{q_j + q_k}, \tag{2.7}$$

and

$$t_{jk} = \frac{2q_j}{q_j + q_k}, \tag{2.8}$$

while for *p*-polarized light they are given as

$$r_{jk} = \frac{\tilde{n}_k^2 q_j - \tilde{n}_j^2 q_k}{\tilde{n}_k^2 q_j + \tilde{n}_j^2 q_k}, \tag{2.9}$$

(2.10) $$t_{jk} = \frac{2q_j}{q_j + q_k},$$

where

(2.11) $$q_j = \tilde{n}_j \cos(\phi_j) = [\tilde{n}_j^2 - \tilde{n}_0^2 \sin^2(\phi_0)]^{1/2},$$

and ϕ is the incident illumination angle relative to the surface normal. The phase matrix that describes the propagation through layer j is given by

(2.12) $$L_{jk} = \begin{bmatrix} e^{-i\xi_j d_j} & 0 \\ 0 & e^{i\xi_j d_j} \end{bmatrix},$$

with

(2.13) $$\xi_j = \frac{2\pi}{\lambda} q_j,$$

where d_j is the thickness of layer j. The interface phase matrices can be used to determine the total system transfer matrix $\mathbf{S}$, which relates the electric fields at the ambient side and substrate side by:

(2.14) $$\begin{bmatrix} E_0^+ \\ E_0^- \end{bmatrix} = \mathbf{S} \begin{bmatrix} E_{m+1}^+ \\ E_{m+1}^- \end{bmatrix},$$

with

(2.15) $$\mathbf{S} = \begin{bmatrix} S_{11} & S_{12} \\ S_{21} & S_{22} \end{bmatrix} = \left(\prod_{v=1}^{m} I_{(v-1)v} L_v \right) I_{m(m+1)}.$$

Here $\mathbf{S}$ depends on polarization, and application of the appropriate Fresnel coefficients is implied. For the multi-layer stack, the total reflection and transmission coefficients are $r = E_0^- / E_0^+ = \mathbf{S}_{21} / \mathbf{S}_{11}$ and $t = E_{m+1}^- / E_{m+1}^+ = 1/\mathbf{S}_{11}$, respectively. The transmissivity for the multi-layer film is then $\mathrm{T} = |t|^2 \bar{n}_{m+1} / \bar{n}_0$ and the resistivity is R = $|r|^2$.

In contrast to light in the thin layers composing the electrodes and organic films, light in the much thicker glass substrate (~ 1 mm) of a typical organic solar cell must be treated as incoherent. Multiple passes through the glass determine the cumulative intensity transferred to the glass/ITO interface, calculated as

$$I_{glass-ITO} = I_0 \frac{(1 - R_{air-glass}) e^{-2\pi k/\lambda}}{1 - R_{air-glass} R_{cell} e^{-2\pi k/\lambda}}, \tag{2.16}$$

where $I_{glass\text{-}ITO}$ is the light intensity in the glass just before reaching the glass-ITO interface, $R_{air\text{-}glass}$ is the reflectivity of the air-glass interface, and R_{cell} denotes the total reflectivity of the glass-multilayer interface.

To obtain the electric field within layer j, the total transfer matrix can be re-expressed as:

$$\mathbf{S} = \mathbf{S}'_j L_j \mathbf{S}''_{\mathbf{j}}, \tag{2.17}$$

with

$$\mathbf{S}'_j = \left(\prod_{v=1}^{j-1} I_{(v-1)v} L_v \right) I_{(j-1)j} \tag{2.18}$$

and

$$\mathbf{S}''_j = \left(\prod_{v=j+1}^{m} I_{(v-1)v} L_v \right) I_{m(m+1)}. \tag{2.19}$$

The electric field propagating in the positive z direction in layer j at the top interface is

(2.20) $$\mathbf{t_j^+} = \frac{E_j^+}{E_0^+} = \frac{1/\mathbf{S'_{j,11}}}{1 + \frac{\mathbf{S'_{j,12}S''_{j,21}}}{\mathbf{S'_{j,11}S''_{j,11}}}\exp(i2\xi_j d_j)},$$

and similarly the electric field propagating in the negative z direction at the top interface is

(2.21) $$\mathbf{t_j^-} = \frac{E_j^-}{E_0^+} = \mathbf{t_j^+}\frac{\mathbf{S''_{j,21}}}{\mathbf{S''_{j,11}}}\exp(i2\xi_j d_j).$$

To determine the total electric field at an arbitrary position inside layer *j*, we consider each component of the electric field vector separately $E_x(z)$, $E_y(z)$, and $E_z(z)$, and distinguish polarization explicitly (Ohta, Ishida, 1990):

(2.22) $$E_x(z) = [E_p^+(z) + E_p^-(z)]\cos(\phi_j) = (t_j^+ e^{i\xi_j z} + t_j^- e^{-i\xi_j z})\overline{E}_0^+ \cos(\phi_0)$$

(2.23) $$E_y(z) = E_s^+(z) + E_s^-(z) = (t_j^+ e^{i\xi_j z} + t_j^- e^{-i\xi_j z})\overline{E}_0^+$$

(2.24) $$E_z(z) = [E_p^+(z) + E_p^-(z)]\sin(\phi_j) = (t_j^+ e^{i\xi_j z} - t_j^- e^{-i\xi_j z})\overline{E}_0^+ \sin(\phi_0)$$

The electric field intensity components normalized by the incident intensities are given by:

(2.25) $$F_x(z) = \left|E_x(z)\right|^2 \Big/ \left|E_{0p}^+\right|^2$$

(2.26) $$F_y(z) = \left|E_y(z)\right|^2 \Big/ \left|E_{0s}^+\right|^2$$

(2.27) $$F_z(z) = \left|E_z(z)\right|^2 \Big/ \left|E_{0p}^+\right|^2$$

If the incident light is not polarized (e.g. sunlight) then the total field intensity at a point z is given by

(2.28) $$F(z) = [F_x(z) + F_y(z) + F_z(z)]/2.$$

The electric field intensity distribution within an archetypal organic photovoltaic (OPV) cell is given in **Fig. 2.5** of the following section. Light enters the cell from the left, through the 1 mm glass substrate and 150 nm ITO electrode. The remainder of the structure is 20 nm CuPc, 40 nm C60, 7 nm BCP, and 100 nm Ag. The optical constants for each layer are provided in Appendix I. This OPV structure will be used throughout the rest of this chapter to serve as an example.

2.4 Absorption of light within multi-layer thin films

Having modeled the electric field intensity as a function of depth (*z*) within the cell, we can now calculate the fraction of light absorbed in any region of the device, allowing for detailed and quantitative device optimization to be performed. In general, the total absorptance is given by $A = 1 - R - T$. However, this does not provide any information about where the light is absorbed in the stack. To accomplish this we turn to the Poynting vector $S = \left[\overline{E} \times \overline{H}\right]$, which gives the energy flow of an EM wave through a unit area. For electromagnetic plane waves, the intensity can be derived from *S* as $I = (1/2)c\varepsilon n\left|E\right|^2$, from which the time-averaged absorbed power as a function of position can be written as

$$Q_j(z) = g_j \frac{c\varepsilon_0}{2}\left|E_j(z)\right|^2, \tag{2.29}$$

where

$$g_j = \frac{4\pi k_j n_j}{\lambda n_0 \cos(\phi_0)}. \tag{2.30}$$

The relationship between the electric field distribution and the absorbed power for the archetypal solar cell is shown in **Fig. 2.5**. Similarly, the differential absorptance *dA* within a differential thickness *dz* at a given depth *z*, which is proportional to incident intensity, is given by

(2.31) $$dA = g_j F(z) dz.$$

For Equation 2.30, g_j is defined for a transparent initial medium. If the initial layer is not transparent (such as a incoherently thick substrate of polymer with a non-zero extinction coefficient) then g_j can be generalized as:

(2.32) $$g_j = \frac{4\pi}{\lambda} \mathrm{Re}\left(\frac{\tilde{n}_j \cos(\phi_j)}{\tilde{n}_0 \cos(\phi_0)} \right) \mathrm{Im}(\tilde{n}_j \cos(\phi_j)).$$

The partial absorptance within a given layer between a depth z_1 and another depth z_2 is given by

(2.33) $$A(z_1 < z < z_2) = \int_{z1}^{z2} g_j F(z) dz.$$

The wavelength-dependent absorption of light for each component of the archetypal ITO-OPV cell is shown in **Fig. 2.6**. Note that ITO is often considered transparent in device modeling, but may actually absorb up to 10% of the incident light when using the full optical properties given in **Appendix I**. The absorption spectra of CuPc and C60 constituent materials are also very evident in the device absorption spectra.

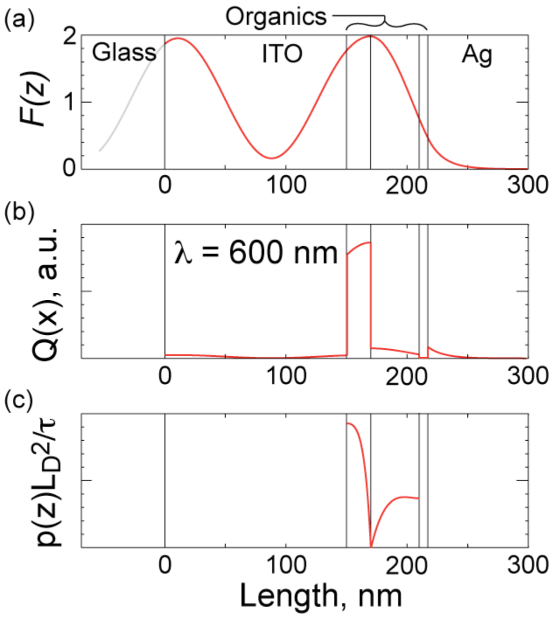

Figure 2.5. For an archetypal solar cell with light entering from left through a glass substrate (a) the electric field intensity distribution within the cell is for λ = 500 nm, (b) the power absorbed by the constituent layers, and (c) the exciton density p(*z*) within the organic layers.

2.5 Calculating the external quantum efficiency

Once the absorbed power distribution within the active layers is calculated, the exciton generation rate can be determined by $G_j(z) = (\lambda/hc)Q_j(z)$. To determine the number of excitons that reach the donor-acceptor (DA) interface and dissociate into electrons and holes, the exciton diffusion equation must be solved:

$$L_{D,j}^2 \frac{\partial^2 p}{\partial z^2} - p + \tau_j G_j = 0, \tag{2.34}$$

where $L_{D,j}$ is the characteristic exciton diffusion length layer j, p is the exciton density, and τ is the exciton lifetime. In the calculations presented here, the exciton diffusion equation is solved using a finite difference method with a node separation of 0.2 nm. The boundary conditions for the diffusion equation are 100% efficient charge transfer at the D-A interface (i.e. $p_{DA} = 0$), and zero exciton diffusion ($\partial p_{DA} / \partial z = 0$) at the opposite boundary. The subscript "DA" denotes the value being evaluated at the donor-acceptor interface, where $z = z_{\mathrm{DA}}$. The exciton density distribution for the ITO-glass OPV cell is shown in **Fig. 2.5(c)**. The contribution to the photocurrent for layer j is

(2.35) $$J_j = q \frac{L_{D,j}^2}{\tau_j} \left| \frac{\partial p}{\partial z} \right|_{DA} .$$

Also, the external quantum efficiency contribution for layer j is

(2.36) $$n_{EQE,j} = \frac{2J_j}{qc\varepsilon_0 \left| E_0^+ \right|^2} .$$

Note that the current and quantum efficiencies depend on the polarization of incident light via the optical field intensity distribution. Changes in the equations used to calculate the optical field intensity for *p*- and *s*-polarized light are implied. Modeled and experimental values of the external quantum efficiency of the ITO-glass OPV cell for a range of illumination wavelengths are shown in **Fig. 2.6(b)**. The diffusion lengths for CuPc and C60, from fitting with experimental results, are $L_{D,CuPc} = 5.7$ nm and $L_{D,C60} = 16$ nm. These values are well within the range reported in the literature (Peumans et al., 2003b). The experimental and calculated η_{EQE} show very good agreement. As described previously, integrating the product of external quantum efficiency and photon flux over all incident wavelengths gives the short circuit current of the cell:

(2.37) $$j_{SC} = q \int \eta_{EQE} S(\lambda) d\lambda .$$

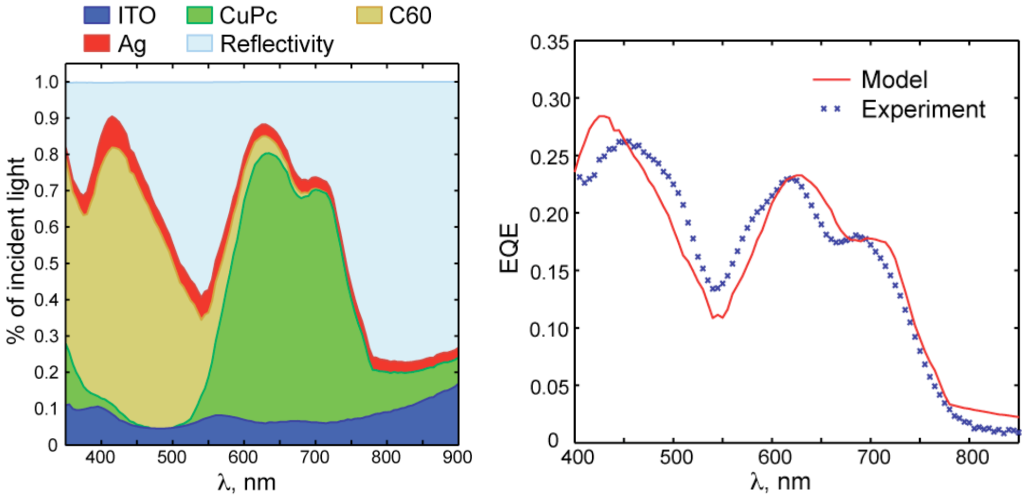

Figure 2.6. (a) The absorption contribution of the ITO-OPV cell layers along with the remaining light reflected from the cell. (b) The resulting external quantum efficiency for the OPV structure. The model is compared with experiment using exciton diffusion lengths as fitting parameters set as $L_{D,C60}$ = 16 nm and $L_{D,CuPc}$ = 5.7 nm.

The angular dependencies of absorption and η_{EQE} for the glass-ITO cell are given in **Fig. 2.7**. The external quantum efficiency is given for an average of *s*- and *p*-polarized light. We see that for *s*-polarized light there is actually an increase in the absorption at small off-normal angles, and that the averaged η_{EQE} is rather insensitive to illumination angle. The increase in η_{EQE} for s-polarized light for small off-normal angles is attributed to constructive interference of the reflected in transmitted waves at each interface, where the phase length of the plane wave has an angular dependence. However, note that the incident light intensity at the cell surface drops off as cos(ϕ) due projection as illustrated in **Fig. 2.8**. Thus, as will be discuss in **Chapter 6**, the current density of planar OPV cells drops off roughly as cos(ϕ).

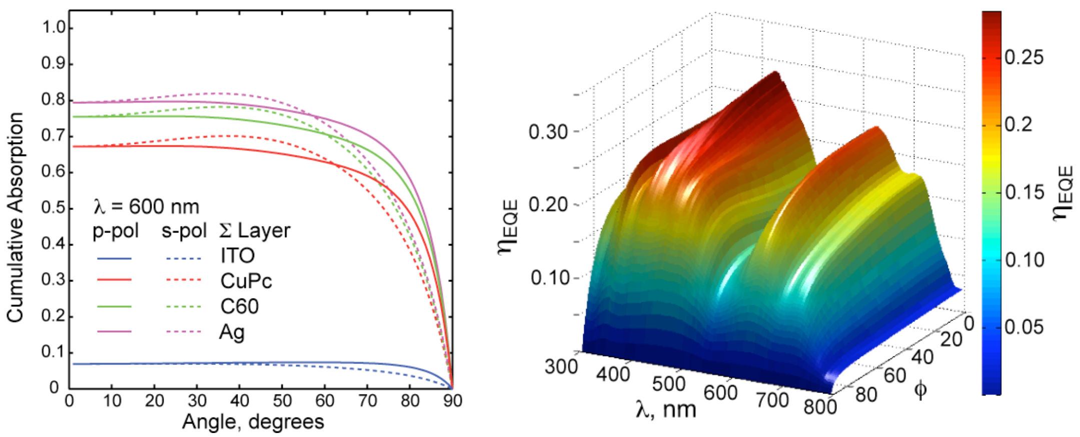

Figure 2.7. (a) The cumulative absorption in each of the layers with variation in illumination angle for p- and s-polarized light for 600 nm incident light. The absorption for each layer is summed with the previous layers. Combining absorption from all layers and reflectivity sums to unity. (b) The external quantum efficiency with change in incident light wavelength and angle.

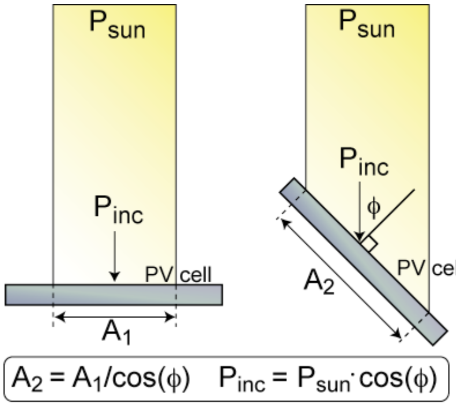

Figure 2.8. Illustration of the change in incident irradiance on a PV cell with angle. The intensity reduces with cos(ϕ) for collimated light such as direct sunlight.

Finally, as discussed in **Section 2.2**, the quantum efficiency can be defined as external quantum efficiency (η_{EQE}), internal quantum efficiency (η_{IQE}), or modified internal quantum efficiency (η_{IQE}'). These three quantities are plotted together for the glass-ITO OPV cell in **Fig. 2.9**. It is observed that η_{IQE}' is smaller than η_{IQE}, as is expected since η_{IQE}' takes into account light that is absorbed in the electrodes, which do not participate in the energy conversion process. This parameter is unimportant for single layer devices but becomes important for systems that re-use light not absorbed by the active layers. For example, semitransparent OPV cells could be used as window coatings, balancing transmission through the cell with absorption by the active layers. Also, an opaque cell in which reflected light is incident upon another PV cell performs best when minimizing parasitic absorption as will be discussed in detail in **Chapter 6**.

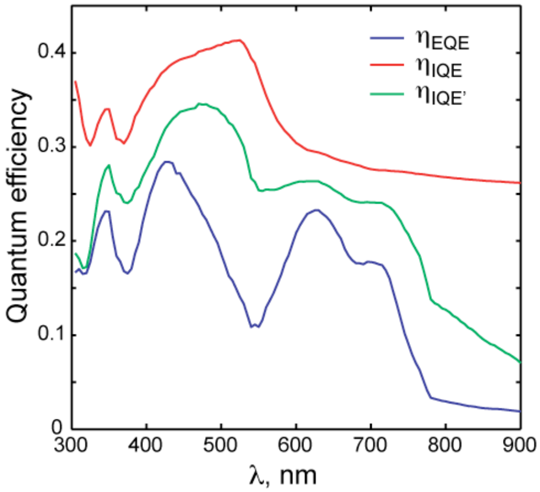

Figure 2.9. Comparison of the external quantum efficiency, the internal quantum efficiency and the modified internal quantum efficiency defined in **Section 2.5**, for the ITO-glass OPV device.

2.6 Model limitations

As mentioned in the beginning of this chapter, the optical modeling used here is not unique to this work; similar models have been applied in a number of recent studies to provide valuable insight into device performance as well as methods to optimize device structure (Peumans et al., 2003b; Cheyns et al., 2008b; Mapel et al., 2007; Tong et al., 2008). As with these other models, it contains several key parameters and several assumptions that should be reviewed to determine the impact they have on the predicted solar cell performance. These parameters include (1) the layer thicknesses and film roughness, (2) exciton diffusion length, (3) material optical properties, and (4) the boundary condition applied to the numerical solution of the exciton diffusion equation (Eq. 2.34). There is always uncertainty in the deposited layer thicknesses (e.g. +/- 5% for vacuum deposited films is typical). Furthermore, surface roughness depends on the deposition conditions and crystallinity of the layers, which together with material purity can modify the exciton diffusion lengths and optical constants of the films. In fact, the measured exciton diffusion lengths reported for CuPc and C_{60} range from 5-15 nm and 10-40 nm, respectively (Peumans et al., 2003b; Mapel et al., 2007).

(1) *Layer thickness and film roughness*

Variation in film thickness results in a phase change of light traversing the layer, and the amount of light attenuation if it is an absorbing film. In addition, the exciton collection efficiency depends on the distance between the location of exciton formation (light absorption) and the DA interface (Rim, Peumans 2008). These effects can dramatically change the optical field distribution and internal quantum efficiency of the PV cell. **Figure 2.10(a-b)** shows the changes in predicted η_{EQE} with variation in the CuPc and C60 layer thickness. It is observed that not only does the magnitude of the spectrum vary but also there is a shift in the wavelength where energy conversion is most efficient. This shift is in large part due to the change in the optical field intensity distribution when varying layer thickness.

Thin films are typically considered optically flat if the film roughness is much smaller than the wavelength of light. The root-mean-square roughness of vacuum deposited thin organic and metal films is typically between 2-10 nm. As this roughness is smaller than wavelengths in the visible range (300-900 nm), roughness is not included in the model. However, scattering can be included in the optical model by modifying the reflection coefficients to include a Gaussian distribution characterized by the film RMS roughness (Filinski, 1972). This model is an attempt to account for phase variations of the optical field distribution due to film roughness. Incorporating film roughness in thin devices with strong internal microcavities can result in a sizeable redistribution and broadening of the optical field intensity distribution (An et al., 2009).

(2) *Exciton diffusion length*

The greater length the exciton diffusion length, the more likely it will reach the DA interface and dissociate into charge. This parameter is one of the most critical features of the model, but also a widely varying value in the literature. The exciton diffusion length (L_D) strongly depends on film quality, purity, and crystallinity; measurements of diffusion lengths can vary by up to 200% (Peumans et al., 2003b). In this work L_D is used as a fitting constant between the optical model developed in this chapter and experimental results for OPV cells developed in later chapters (Terao et al., 2007). Due to the sensitivity of the diffusion length to multiple parameters, variations in the diffusion lengths will also be seen in this work (although all fall within the range observed in literature). Changing the values of L_D for C60 and CuPc in the model for the ITO-glass OPV cell alters the magnitude of η_{EQE} without inducing wavelength-dependent shifts, as shown in **Fig. 2.10(c-d)**. This is expected, since in the approximation used here it affects the probability of energy conversion equally at all wavelengths over the absorption band of a material. Many physical features can be hidden within the chosen exciton diffusion lengths that are material (or interface) specific but not wavelength dependent. For example, a poor electronic interface between an organic layer and its adjacent electrode will lower the device η_{EQE}, which can be indirectly compensated for by lowering the L_D. Detailed measurements of the organic semiconductor the L_D used to make a given device along with the application of the diode equation (2.5) can help decouple resistive losses from the exciton behavior of the material in a device.

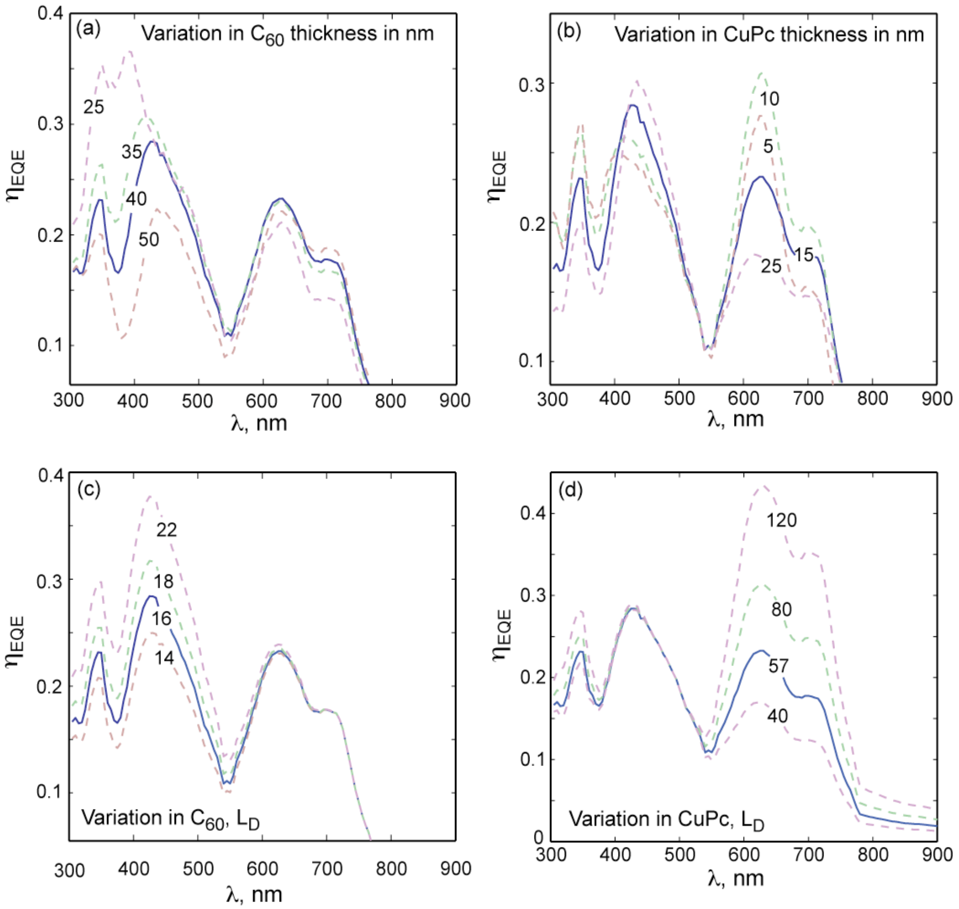

Figure 2.10. The change in the η_{EQE} spectrum for the glass ITO-OPV cell with changes in the (a) C60 layer, and (b) CuPc layer thicknesses. Also shown are the change in the η_{EQE} spectrum for the same PV cell with changes in the L_D of (c) C60 and (d) CuPc. The blue line in all curves is the same as shown in **Fig. 2.6** for the model-experiment comparison.

(3) Optical properties of materials

The refractive indices of all materials used in device modeling are provided in Appendix I. There are dependencies on film thickness, crystallinity and film quality for the measured optical properties of some organic materials (Peumans et al., 2003b). One major assumption in the model with regard to the optical properties of the materials is that the films are isotropic and homogeneous. Optical anisotropy has been observed in organic films with high levels of crystallinity such as CuPc.

However, the grain size of CuPc films is small enough that anisotropic characteristics are not typically observed in device applications (Cheyns et al., 2008b).

(4) *Boundary conditions*

The boundary condition applied to the exciton diffusion equation were that all excitons which reach the DA interface dissociate into free charges, with zero exciton flux at the opposite side of the active layer film. However, there may be quenching at the opposite interface, especially if the organic layer is in contact with a metal electrode. The change in η_{EQE} for complete quenching of excitons at both sides of each organic active layer is shown in **Fig. 2.11**. The result is similar to the change in L_D, where a change in the probability of absorbed light being converted to extracted charge resulting only in a shift in η_{EQE} magnitude. This suggests that varying both the boundary condition assumptions and L_D can provide a fit to experimental data for the magnitude of η_{EQE}.

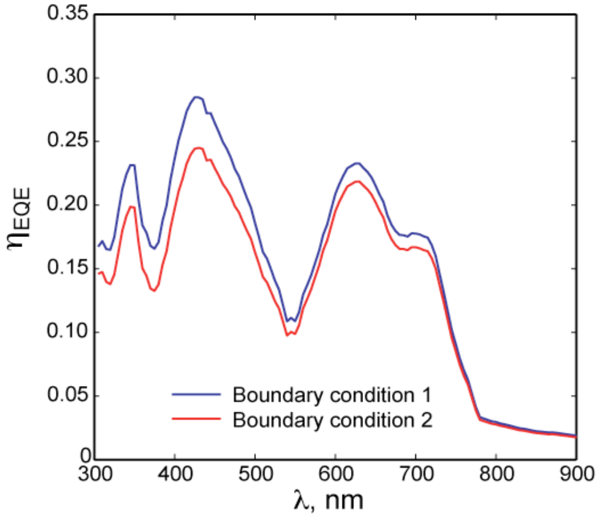

Figure 2.11. The η_{EQE} spectrum for two different boundary conditions applied to the exciton diffusion equation. Boundary condition 1: compete exciton quenching at the DA interface (p_{DA}

= 0), and zero exciton diffusion at the opposite boundary ($\partial p_{DA} / \partial z = 0$). Boundary condition 2: complete exciton quenching at all interfaces for both the donor and acceptor layer.

CHAPTER 3

ORGANIC PHOTOVOLTAIC CELLS WITH METAL-ORGANIC-METAL STRUCTURE

3.1 Introduction and motivation

In thin film organic photovoltaic (OPV) devices, continuous electrode films are used to transport charge carriers to bus-lines, which subsequently deliver them to an external circuit, as illustrated in **Fig. 3.1**. The continuous electrodes are necessary due to the limited conductivity of the adjacent organic semiconductors. One of these electrodes must also effectively transmit incident light into the active layers. To date, the most widely employed transparent electrode has been indium tin oxide (ITO), but it has significant shortcomings for low-cost and large-area device applications including the rising cost of indium, brittleness (shown in **Fig. 3.2**), the need for high growth temperature, and indium diffusion that may degrade device performance (Fortunato et al., 2007). Research concerning ITO replacements in organic photovoltaic (OPV) devices has included work on other conducting oxides (Fortunato et al., 2007; Yang, Forrest, 2006), carbon nanotubes (Rowell et al., 2006), graphene (Wang et al., 2008; Wu et al., 2008), highly conductive polymers (Zhou et al., 2008; Ahlswede et al., 2008), metallic micro-grids combined with conducting polymers

(Tvingstedt, Inganas, 2007; Kang et al., 2008), and thin metal films (Al-Ibrahim et al., 2005; Oyamada et al., 2007).

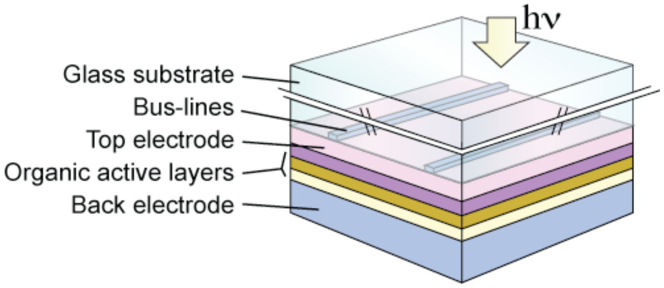

Figure 3.1. Illustration of an organic PV cell with transparent electrode including bus-lines. Note that the figure is not to scale; the thickness of bus-lines are typically much larger than the thin films that make up the cell.

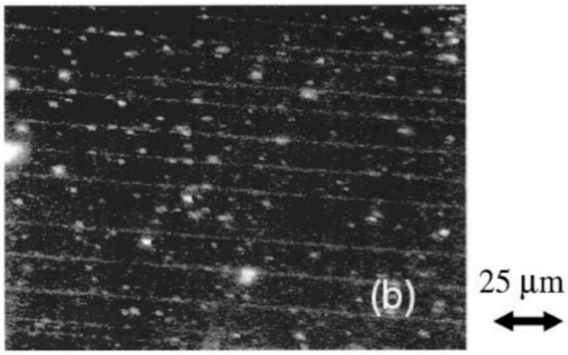

Figure 3.2. Optical micrograph of a 105 nm thick sample of ITO coated PET at 2.5% strain, showing crack formation in the ITO coating. At a strain of 4%, sheet resistance is increased by over 140 times compared to the unstrained film (Cairns, Crawford, 2005).

Table 3.1 summarizes the performance of OPV cells that utilize these alternative electrodes along with data for reference devices using ITO when provided. This list is not an exhaustive literature summary, but provides an overview of recent developments in alternative transparent conducting electrodes. Similarly, alternative electrodes are important for OLED applications (Li et al., 2004; Pode et al., 2004;

Klauk et al., 2000), but are not considered here. In **Table 3.1** it is observed that very few of these alternative electrodes perform as well as their ITO counterpart. One of the more promising alternatives is ZnO:Al with gold nanoparticles; however, this material is still a brittle oxide that is unsuitable for use in flexible devices or deposition on flexible substrates. Furthermore, the gold nanoparticles may be thermally unstable and prone to aggregation over time. The silver-grid with conductive polymer also performs well, yet the fabrication process will likely be difficult to scale while maintaining low production cost.

Here we investigate in detail the application of simple non-patterned ultra-thin metal films as the light-incoupling electrode in planar heterojunction (PHJ) and bulk heterojunction (BHJ) OPV cells. The ability to use non-patterned metal films as transparent electrodes potentially offers a number of advantages, including compatibility with low-cost roll-to-roll fabrication (Bishop, 2007), low-temperature processing (Fortunato et al., 2007), the ability to deposit on non-planar substrates (O'Connor et al., 2008b), and improved mechanical flexibility (Lewis et al., 2004). This chapter systematically examines thin metal electrodes from the standpoint of electrical resistivity, which depends on electrode composition and thickness, and from the standpoint of performance in OPV cells. Using the optical models developed in **Chapter 2**, we develop design rules for metallic electrodes in devices. To validate these predictions, we then fabricate test devices consisting of ITO-organic-metal and metal-organic-metal (m-o-m) configurations deposited on glass. Cells using the m-o-m configuration with a silver anode of proper thickness are shown to achieve parity with an analogous cell deposited onto ITO. Lastly, metal-organic-metal structures in which light enters from the opposite side of the substrate are discussed (i.e. “top-illuminated”); such devices are important in the context of deposition on low-cost, opaque and possibly temperature-sensitive substrates (e.g. metal foils and/or plastic films).

Table 3.1. Summary of the best results for organic photovoltaic cells with alternative transparent conducting electrodes. Comparative performance of OPV cells with the alternative electrode and ITO is shown when provided in the literature.

Device	j_{sc}, mA/cm^2	V_{oc}, V	FF	η, %	P_{inc}, mW/cm^2	R_{sh}, Ω/sq	Ref
Alternative transparent conducting oxide							
glass/ZnO:Al/Au/CuPc/C60/Alq3/Al	-	-	-	1.4	100	10	[1]
glass/ITO/Au/CuPc/C60/Alq3/Al	-	-	-	1.4	100	10	
glass/GZO/CuPc/C60/BCP/Ag	9.0	0.5	0.35	1.25	100	-	[2]
No reference comparison							
glass/SnO:F/CuPc/C60/BCP/Ag	10	0.47	0.55	2.5	100	-	[3]
glass/ITO/CuPc/C60/BCP/Ag	10.25	0.5	0.6	3.5	100	15	[4][*]
Highly conductive polymer							
glass/polymer[**]/P3HT:PCBM/Al	8.5	0.575	0.52	2.6	100	250	[5]
glass/ITO/P3HT:PCBM/Al	9.0	0.59	0.62	3.5	100	15	
glass/PEDOT:PSS:Sorbital/MEH-PPV/PCBM/Al	1.6	0.75	0.24	0.36	100	10^3	[6]
glass/ITO/PEDOT:PSS/MEH-PPV/PCBM/Al	2.1	0.75	0.23	0.46	100	20	
Metal grid with polymer							
glass/Ag-grid/PEDOT/AFPO-G/PCBM/LiF/Al	3.67	0.58	0.47	1.0	100	-	[7]
glass/ITO/PEDOT/APFO-G/PCBM/LiF /Al	3.63	0.58	0.43	0.83	100	-	
glass/nano-Ag/PEDOT/CuPc/PtCBI/BCP/Ag	1.83	-	-	0.42	65	16	[8]^
glass/ITO/CuPc/PtCBI/BCP/Ag	1.54	-	-	0.38	65	15	
Carbon nanotubes and graphene							
PET/SWNT/PEDOT:PSS/P3HT:PCBM/Al	7.8	0.61	0.52	2.5	100	200	[9]
glass/ITO/PEDOT:PSS/P3HT:PCBM/Al	8	0.61	0.61	3.0	100	15	
glass/TGF/CuPc/C60/BCP/Ag	2.1	0.48	0.34	0.4	85	10^4	[10]
glass/ITO/CuPc/C60/BCP/Ag	2.8	0.47	0.54	0.84	85	15	
Thin metal film – inverted cells							
Si/Ti/P3HT:PCBM/PEDOT:PSS/Au	6.25	0.55	0.33	1.12	100	-	[11]
PET/ITO/PEDOT:PSS/P3HT:PCBM/Al	6.6	0.6	0.39	1.54	100	-	
Si/MgAu/MoO$_3$/CuPc/C60/BCP/Ag/MgAg	3.68	0.52	0.55	1.05	100	-	[12]
glas/ITO/CuPc/C60/BCP/Ag	3.65	0.49	0.61	1.15	100	-	

[*] Alternative electrode device structure is compared to ITO based device previously published.

[**] The polymer is PEDOT:PSS with a combination of additive high-boiling temperature, polar compounds.

^Active layers are thicker than that for optimal performance to prevent shorting from the rough Ag-nanowire
[1] (Bernede et al., 2008), [2] (Yang,Forrest, 2006), [3] (Yang,Forrest, 2006), [4] (Xue et al., 2004), [5] (Ahlswede et al., 2008), [6] (Zhou et al., 2008), [7] (Tvingstedt,Inganas, 2007), [8] (Lee et al., 2008), [9] (Rowell et al., 2006),
[10] (Wu et al., 2008), [11] (Al-Ibrahim et al., 2005), [12] (Oyamada et al., 2007)

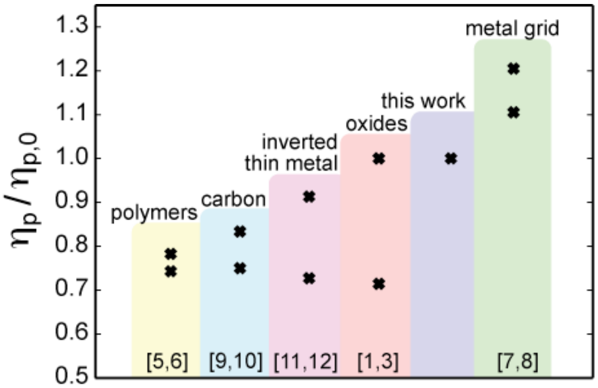

Figure 3.3. The efficiency of the alternative electrode given in **Table 3.1** normalized by the efficiency of the control PV cell using ITO. The references in the figure correspond to those listed in **Table 3.1**. Note that although the metal grid devices give the best relative performance, low cost scale-up may be a challenge as discussed in the text.

3.2 Optimization of thin metal films: conductivity, transparency, and electronic interface with organic semiconductors

If a thin metal film replaces ITO, a thickness adjustment is required to optimize the trade-off between conductivity and transparency. In addition, resistance to charge transfer from the organic layer to the metal electrode must be minimal. These requirements are addressed in the following subsections.

3.2.1 Thin metal film resistivity

Achieving low sheet resistance of the light in-coupling electrode is important for OPV cell scale-up, in order to reduce losses in transporting charge to external circuitry via bus-lines. As sheet resistance increases, bus-line spacing must be reduced, increasing cell shading (Rowell et al., 2006). Therefore, we first consider the resistivity of several thin metal films that have been previously demonstrated in OPV devices including Ag, Au, and Al (Peumans et al., 2003b; O'Connor et al., 2008b). **Figure 3.4** plots the sheet resistance versus film thickness for these metals using data compiled from our laboratory, as well as from the literature; film deposition methods included vacuum thermal evaporation (VTE) and sputtering, both of which are compatible with high throughput processing on foils (Camacho, Oliva, 2006; Devries, 1988; Romanyuk et al., 2007; Noge et al., 1995; Hatton et al., 2003).

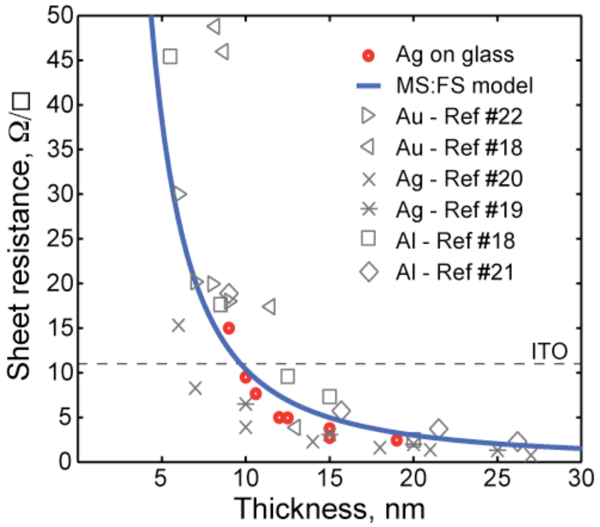

Figure 3.4. A plot of experimentally determined sheet resistance versus metal films thickness for Ag, Al, and Au, compared to a nominal sheet resistance of ITO. The solid line is a fit to the experimental data for Ag films, based on the Mayadas-Shatzkes' and Fuchs-Sodheimer's models (**Eqs. 3.1-3**). Variations in sheet resistance at a particular thickness value are mainly due to varying film morphology, itself affected by substrate surface treatments and metal film deposition conditions.

Thinner films generally exhibit higher resistance due to geometric effects, but also higher resistivity, due to electron scattering from the surface and grain boundaries. These processes are taken into account by the Fuchs-Sodheimer (FS) and Mayadas-Shatzke (MS) models, respectively (Mayadas et al., 1969; Camacho, Oliva, 2006). A line fit based on these models is plotted as an example for the measured Ag on glass data in **Fig. 3.4**, given by:

(3.1)
$$\rho_{FS} = \rho_{bulk}\left[1 - \frac{3}{2k}\int_0^1 du(u-u^3)\frac{(1-p)[1-\exp(-k/u)]}{1-p\exp(-k/u)}\right]^{-1},$$

(3.2)
$$\rho_{MS} = \frac{\rho_{bulk}}{3}\left[\frac{1}{3}-\frac{1}{2}\alpha+\alpha^2-\alpha^3\ln(1+1/\alpha)\right]^{-1},$$

(3.3)
$$\rho = \rho_{FS} + \rho_{MS} - \rho_{bulk},$$

where $k = t/\lambda_e$, $\alpha = (\lambda_e/D)\cdot(R/1\text{-}R)$. The modeling constants for Ag include the electron mean free path $\lambda_e = 52$ nm, the bulk resistivity $\rho_{bulk} = 1.59$ μΩ-cm (Ashcroft, 1976), a surface reflection coefficient $p = 0.6$, and a grain boundary reflection coefficient $R = 0.78$. The grain size D is proportional to film thickness t via $D = 4.87\cdot t$, determined empirically. Surface roughness exacerbates scattering and increases the likelihood of parasitic current shunting in a PV cell (Yang, Forrest, 2006; Lee et al., 2008). Note that the thin Ag films deposited in this study exhibit a RMS roughness of 2 - 4 nm as measured by atomic force microscopy (compared to 7 nm found for ITO on glass) and show no correlation between film roughness and thickness, as shown in **Fig. 3.5**. Note also that a film thickness of approximately 10 nm or greater is typically required to maintain a sheet resistance equivalent to or better than ITO.

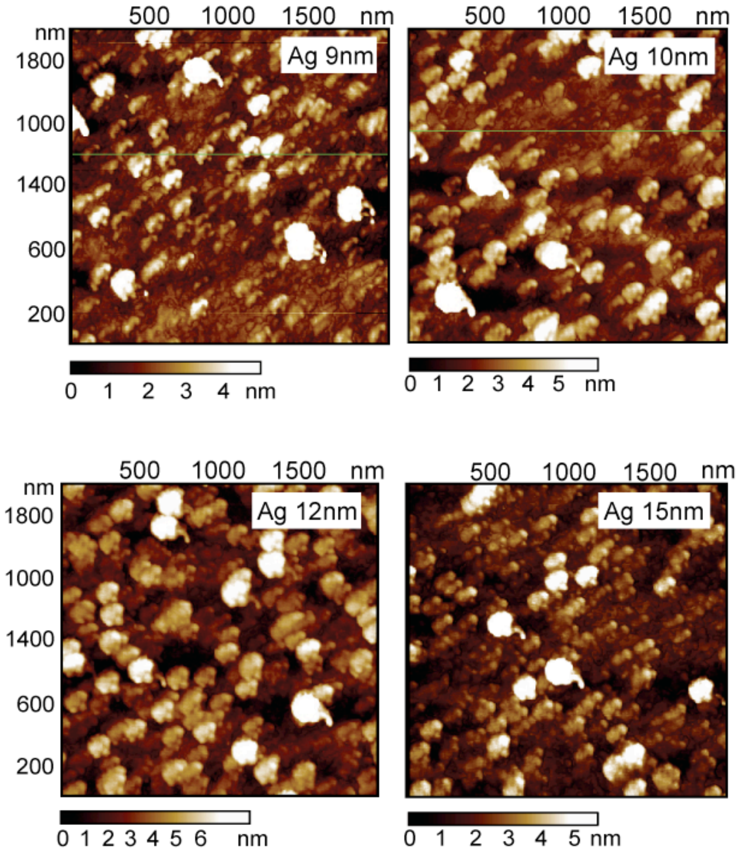

Figure 3.5. Atomic force microscope images of silver films with varying thickness deposited on glass substrates using vacuum thermal evaporation at 10^{-6} torr and deposition rates of 0.2-0.3 nm/s.

3.2.2 Predicted short circuit current

To investigate the expected change in short circuit current density (j_{SC}) produced n a device when switching from an ITO electrode to a thin metal film, we turn to optoelectronic modeling of both planar heterojunction (PHJ) and bulk heterojunction (BHJ) OPV cells, the structures of which are shown in the insets of **Fig. 3.6(a)** and **3.6(b)**. For both cells, j_{SC} is predicted using the formalism discussed in **Chapter 2**. The boundary conditions for solving the exciton diffusion equation are: 1) complete exciton dissociation at the electron donor-acceptor (DA) interface, and 2) zero exciton diffusion rate at the electrode boundaries. The exciton diffusion lengths of CuPc and C60 are taken as $L_{D,CuPc}$ = 9 nm and $L_{D,C60}$ = 16 nm. Following exciton dissociation at the DA interface, 100% charge collection efficiency at the electrodes is assumed (Peumans et al., 2003b). For the BHJ cell, exciton dissociation is assumed to be 100% efficient with an external quantum efficiency given by $\eta_{EQE}(\lambda) = G(\lambda)exp(-L/L_C)$, where G is the exciton generation rate, L is the organic layer thickness, and L_C is a characteristic carrier collection length that is set as 167 nm, which is used as a fitting parameter (Agrawal, Peumans, 2008). The short circuit current density, j_{SC}, is predicted by integrating the product of external quantum efficiency and incident photon flux over the solar spectrum (AM1.5G, truncated between 300-900 nm). The optical constants for all layers used in modeling are taken from literature and tabulated in Appendix I (Peumans et al., 2003b; Rand et al., 2004; Filmetrics, 2002).

Figures 3.6(a) and **3.6(b)** show the range of predicted values of j_{SC} for a 10 nm thick light in-coupling electrode having a given refractive index (n) and extinction coefficient (k) for the PHJ and BHJ cells, respectively. Also shown are the locations of the optical constants for common electrode materials, including metals Al, Au, Ag, and Mg, and conducting oxides ITO, SnO_2:F and AlZnO, with the n and k values averaged between 300-900 nm and weighted by the incident photon flux across the AM1.5 solar spectrum (Cerac, 2008; Tachibana et al., 2007). The values of j_{SC} calculated using dispersion-free optical constants differ by less than 6% from j_{SC} values calculated using the actual wavelength-dependent values for Ag, Au, and oxide electrodes. The difference is greater for Al, but the trend shown is correct and the j_{SC} when using Al is much lower than the other materials. Note that the oxide electrodes employed in OPV cells are typically 100-200 nm thick, while a 10 nm thickness is assumed for all materials in the analysis in **Fig. 3.6;** the resulting j_{SC} for the thin oxide electrodes, however, is similar to values found for typical oxide thicknesses.

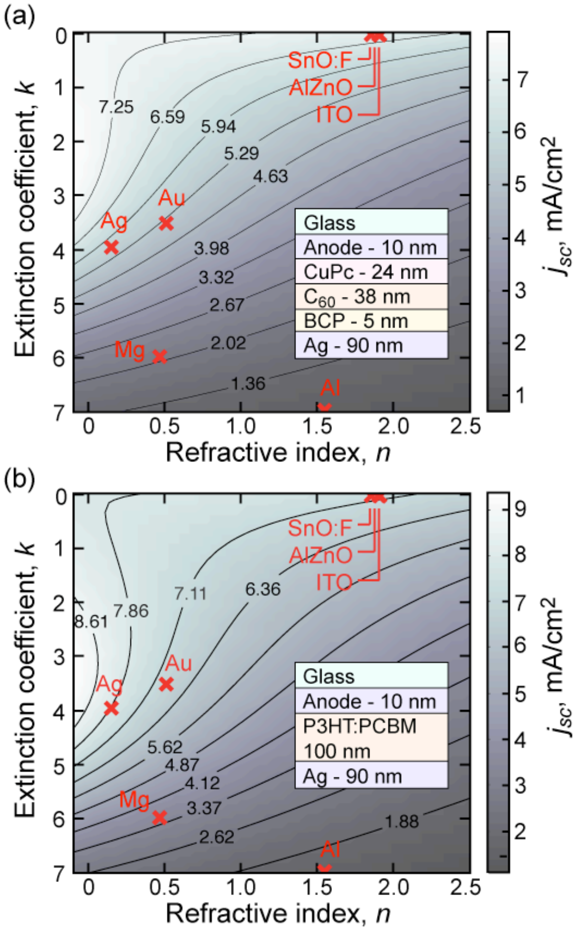

Figure 3.6. The predicted j_{SC} for a 10 nm thick semitransparent electrode (anode) for varying refractive index and extinction coefficient ($\tilde{n} = n + i^*k$) for (a) a PHJ cell, and (b) a BHJ cell, where the structure of each cell is given in the repective inset. The predicted values are compared with the optical constants of several metals and conducting oxides, with the *n* and *k* values averaged over the 300-900 nm wavelength range and weighted by the photon flux across the solar spectrum. The oxide electrodes are typically much thicker in practice (100-200 nm), but their optical constants are shown here nevertheless for comparison purposes.

For the BHJ cell we find that the optimal electrode material should have a very low *n* and a non-zero *k* of approximately 2, with *k* shifted towards smaller values for the PHJ cell. The unique values of *n* and *k* are a result of optimizing the electric field phase shift and the Fresnel coefficient, effectively moving the anti-node of the electric field closer to the donor-acceptor junction (in a planar cell) while maximizing the optical intensity within the device over the absorption band of the active layers. Due to the large extinction coefficients of metal films, the effect of increasing metal thickness is dominated by increased light absorption and the optimal *k* values in **Fig. 3.6(a)** and **(b)** shift to smaller values.

3.2.3 Organic-metal interface

In addition to low sheet resistance allowing low-cost lateral transport of the collected charge to an external circuit, the metal electrode must also have a low contact resistance with the adjacent organic layer. A high contact resistance will reduce the solar cell's power conversion efficiency through increased solar cell series resistance and reduction in V_{OC} (Peumans, Forrest, 2001; Cheyns et al., 2008a).

There are several complex physical effects that arise at metal-organic semiconductor interfaces that are material-specific, and a full analysis is beyond the scope of this chapter. Among the candidate metal electrode materials, Ag was shown in the previous section to have the best combination of conductivity and optical properties, motivating further examination of the interface it forms with CuPc. It has previously been shown that Ag deposited on CuPc forms a sharp, inert interface (Molodtsova et al., 2007; Gorgoi, Zahn, 2006), and hence it is expected that CuPc is physisorbed onto silver with a sharp interface between the two layers, and the complex effects of chemisorption can be neglected (Crispin, 2004).

To investigate the electronic properties of the metal-organic interface, we begin by considering the flat-band energy diagram for the device as shown in **Fig. 3.7** with the work functions for potential anodes ITO, Ag and PEDOT:PSS shown on the left. For this device structure it has been shown that the addition of PEDOT:PSS between the ITO and CuPc layer improves V_{OC} from roughly 0.47 to 0.55 volts (Peumans et al., 2003b). This increase has been attributed to better band alignment between the work function of the anode and the CuPc HOMO level (Peumans et al., 2003b). However, it is shown in **Fig. 3.11** that a device with an Ag anode also shows an increase in V_{OC} over that of the ITO, device, which cannot be explained by a flat band model.

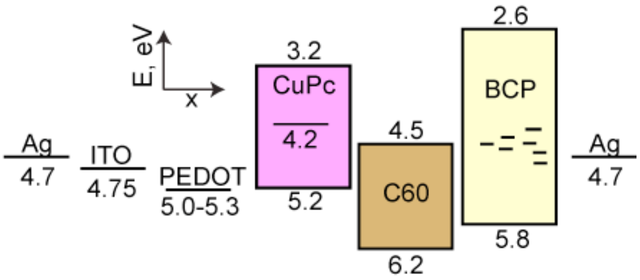

Figure 3.7. Band diagram of the small molecule OPV cell considered in this chapter with Ag, ITO and PEDOT:PSS shown at left as possible anode materials. In this flat-band diagram, the energy levels for each material are considered independent of adjacent layers.

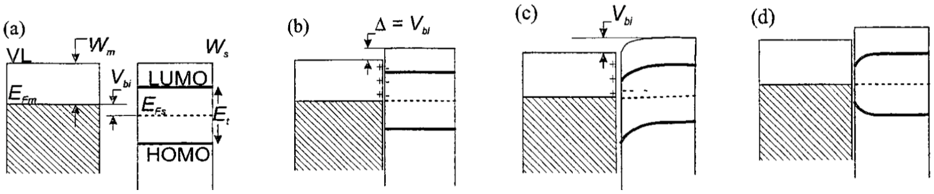

Figure 3.8. Formation of a metal–semiconductor contact. (a) The nonequilibrium (flat-band) alignment before contact is made. All energies are referred to a common vacuum level. The built-in potential (V_{bi}) is the potential difference between Fermi energies (E_{Fm} - E_{Fs}). (b) The extreme case in which the entire difference is accommodated by the formation of an interfacial dipole layer. (c) The extreme case in which the vacuum levels align at the interface and the potential difference is accommodated across a charged depletion zone. (d) Same as case (b), but now including the effect of the image potential (from Scott, 2003).

To understand the origin of this effect, we first consider a generic energy band structure for a semiconductor-metal interface as shown in **Fig. 3.8** under different electronic conditions (Scott, 2003). For an organic semiconductor that has a low concentration of free carriers, several physical processes can affect the band structure, including the formation of an interface dipole (**Fig. 3.8(a)**), charge transfer forming a depletion region (**Fig. 3.8(b)**), and an attractive image potential of the carriers formed near the metal interface, (**Fig. 3.8(c)**). To determine the process specific to the Ag-CuPc interface, it is instructive to consider the photoemission spectra and inverse photoemission spectra for Ag/CuPc samples with varying Ag thickness, as shown in **Fig. 3.9** (Gorgoi, Zahn, 2006). In the photoemission spectra there are two shifts in binding energy of 0.2 eV that occur on transitioning from bare CuPc to Ag/CuPc, at ~1.5 eV and ~ 17.2 eV, where the binding energy is measured relative to the Fermi energy level of CuPc. The shift in the binding energy and particularly at the core molecular orbital suggests the formation of an interface dipole with ~0.2 eV potential.

Secondly, at very low binding energy a signal of emitting charge is observed for silver thicknesses greater than 3.2 nm. The origin of this signal may be the band bending at the interface, through either charge transfer from Ag to CuPc or induced density of states in the band gap of CuPc due to its interaction with Ag. While differentiating these processes is difficult, the latter effect has been experimentally verified for weakly interacting interfaces such as the one under consideration, and hence we assume it to be the dominant process (Vazquez et al., 2007). Finally, we assume that free carriers in the organic layer near the interface with the metal film will see an attractive image potential. Combining these effects gives a proposed qualitative view of the band structure between silver and CuPc illustrated in **Fig. 3.10**. To determine the precise interface band structure, further work is required, which may include scanning tunneling microscopy, photoemission spectroscopy and cyclic voltammetry. For the analysis presented here thus far, the semi-qualitative band diagram suggests that there is a low energy barrier for hole transfer from the CuPc HOMO level to the Ag electrode.

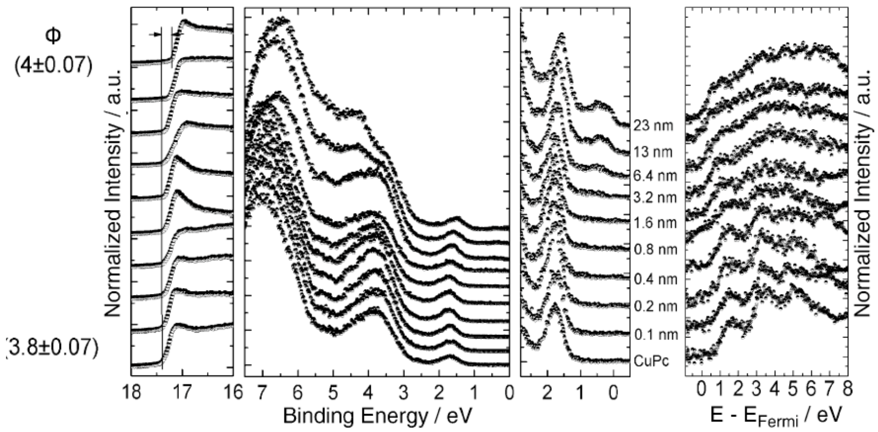

Figure 3.9. Photoemission measurement on Ag/CuPc/H-Si (111) with increasing thickness of Ag on 22 nm CuPc; (b) thickness-dependent IPES measurement on Ag/CuPc/H-Si (111). (From Ref. Gorgoi, Zahn, 2006)

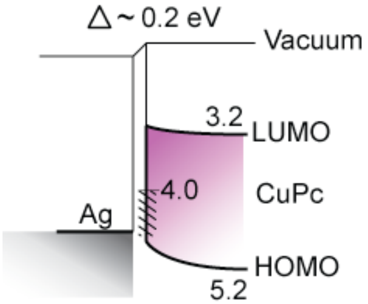

Figure 3.10. Qualitative view of the assumed energy band diagram for a Ag-CuPc interface. There is 0.2 eV shift in potential due to interface dipole formation. The hash lines in the CuPc bandgap represent an induced density of states formed at the interface, and the bending of the CuPc band is due to both a small amount of free carrier charge transfer across the interface and an induced image potential.

3.3 Organic PV with a thin metal electrode on glass substrate

As mentioned above, Ag has the best combination of optical properties and lowest sheet resistance among the metals considered. In addition, it was shown that the Ag-CuPc interface is expected to have low contact resistance. We therefore compare the device performance of PHJ-OPV cells with Ag and ITO light in-coupling electrodes. The device structure shown in **Fig. 3.11** was deposited in vacuum (at 10^{-6} torr), with film deposition rates of 0.1 - 0.3 nm/s. All devices were deposited onto 1 mm thick glass substrates, with the ITO-OPV devices using substrates precoated with 150 nm of ITO. The ITO substrates were UV-O_3 treated for 10 minutes (28 mW/cm^2, $\lambda \sim 254$ nm lamp output, with the sample approximately 1 cm from the lamp) prior to device fabrication to improve charge collection and V_{OC} (Xue et al., 2004). A 9 nm Ag anode was deposited at a rate of 0.2 nm/s and was exposed to air for approximately 2 minutes while the ITO substrates were loaded into the vacuum chamber to complete the device. The OPV cell active area was defined by 1 mm diameter circular cathodes that were deposited through a shadow mask. The current density-voltage (*j*-*V*) characteristics of the metal electrode and ITO-based devices are shown in **Fig. 3.11**. The fill factors (*FF*) of the two devices are similar; j_{SC} is 14% lower for the Ag anode device, while V_{OC} is greater by 14%. Combined, the j_{SC}, V_{OC}, and *FF* parameters yield power conversion efficiencies for the Ag and ITO based devices of 1.88 +/- 0.07% and 1.86 +/- 0.11%, respectively. The 9 nm thick Ag film was measured to have a sheet resistance of 15 Ohm/□, similar to the control ITO electrode with a sheet resistance of 11 Ohm/□. These results suggest that the 9 nm thick Ag anode yields OPV performance that is practically identical to that with an ITO anode. We note that the larger V_{OC} of the Ag electrode devices is likely due to a reduced contact resistance between the Ag and CuPc films. The V_{OC} observed in the ITO-based device is similar to that found in literature, and has been shown to improve with the addition of PEDOT:PSS (Peumans et al., 2003b). Eschewing PEDOT:PSS, however, simplifies the device structure, the deposition process, and may improve device lifetime (Kawano et al., 2006).

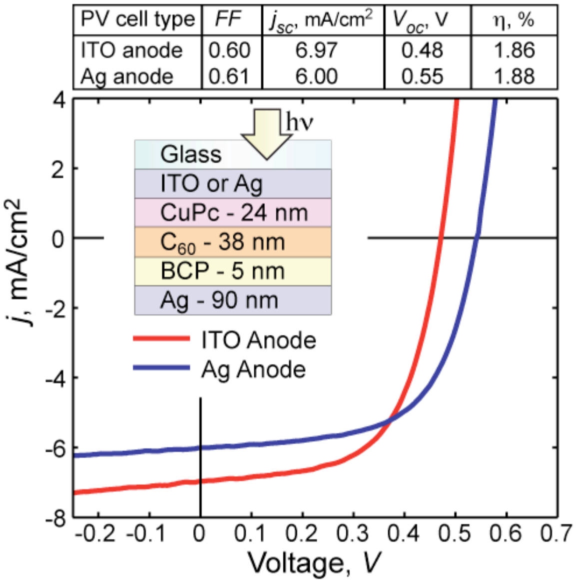

PV cell type	*FF*	j_{SC}, mA/cm^2	V_{OC}, V	η, %
ITO anode	0.60	6.97	0.48	1.86
Ag anode	0.61	6.00	0.55	1.88

Figure 3.11. The *j*-*V* characteristics for OPV cells with ITO and Ag anodes under 106 mW/cm^2 illumination (close to standard AM1.5G conditions). The ITO thickness is 150 nm and the semitransparent Ag electrode is 9 nm. Relevant device performance parameters are summarized in the table. (Inset) The layer structure of the organic solar cells considered, with the light in-coupling electrode either Ag or ITO.

While V_{OC} and FF appear to be largely independent of the Ag electrode thickness, j_{SC} is not, and we extend the optical modeling and experiments to PHJ cells with Ag electrodes of varying thickness. **Figure 3.12** shows the predicted reduction in j_{SC} with increasing Ag thickness calculated using the full optoelectronic model, which accurately tracks the experimentally observed values. For comparison, the average far-field transmittance of the electrode weighted by the AM1.5 photon flux and the transmittance weighted by the organic layer absorption spectra are also provided. We find that the full optical model provides the best fit to the experimental data, while the transmittance weighted by the absorption spectra of the organic layers closely follows. Along with **Fig. 3.12**, these results highlight the importance of the optical constants of all device layers for accurate modeling and suggest that a full optoelectronic model and device fabrication should be performed rather than simple far-field transmittance measurements in optimizing electrode design (Lee et al., 2008).

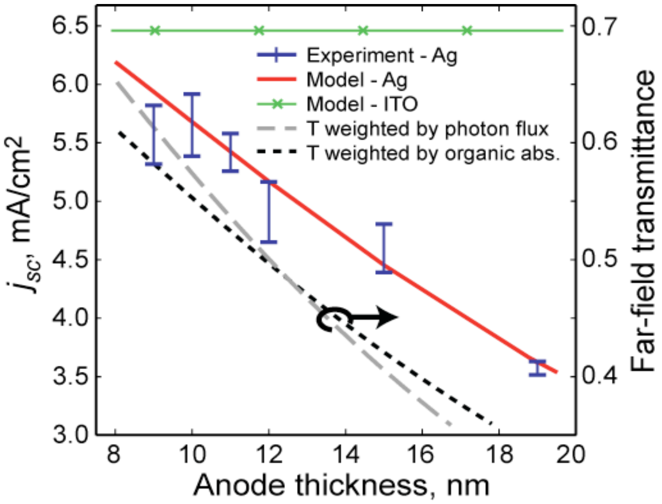

Figure 3.12. Calculated and experimental results of j_{SC} versus anode thickness for OPV cells with Ag and ITO anodes. All devices were illuminated by nearly-AM1.5 light, (100 - 110 mW/cm^2 intensity). The average far-field transmittance of the anode on glass is shown for two conditions; 1) weighted by the solar photon flux for AM1.5, and 2) weighted by the CuPc and C60 absorption coefficients between 300-900 nm.

3.4 Top-illuminated organic PV cells: applying a thin metal electrode on top of the organic layers

A typical organic solar cell is deposited onto a substrate pre-coated with a transparent electrode, through which light passes and enters into the active layers of the device. However, to allow devices to be deposited onto low-cost and/or opaque substrates (e.g. metal foils or fibers), a different architecture is required that allows illumination from the non-substrate side. In this section we consider the potential of applying thin metal coatings on top of the organic layers, opposite the substrate.

Again we turn to optoelectronic modeling to assist in electrode selection for the device structure shown in the inset of **Fig. 3.13**. The metal is now deposited on an organic film with surface roughness greater than the glass substrate; many metals also embed into the underlying organic layer upon deposition increasing interface and surface roughness (Peumans et al., 2003b). To maintain electrode conductivity, the cathode must be thicker. Here we use a 12.5 nm-thick film instead of the 10 nm film used in **Section 3.2.2**. The optical constants *n* and *k* are then varied in the model, allowing the performance of different metals to be mapped. j_{SC} is predicted using the same optical constants, exciton diffusion lengths, and boundary conditions given in **Section 3.2.2**, with results shown in **Fig. 3.13**. We again find that Ag has the optimal optical properties of the metals considered. Silver has also been shown to be an effective cathode when deposited on BCP (Peumans et al., 2003b).

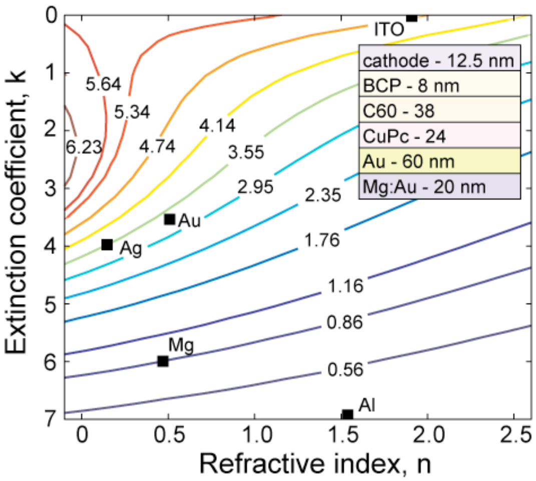

Figure 3.13. Contour plot for predicted j_{SC} for a 12.5 nm thick light-coupling electrode (cathode) for varying refractive index and extinction coefficient ($\tilde{n} = n + i^*k$), for the top-illuminated OPV cell whose structure is shown in the inset.

We performed experimental deposition of this device using Ag, generally following the fabrication sequence described in **Section 3.3**. The sequence was altered however, in that the device was deposited on a silicon substrate, and the anode begins with Mg as a wetting layer, followed by Mg:Au co-deposition (1:1 by volume) for 20 nm and then Au for 60 nm. The anode was then exposed to atmosphere briefly before the remainder of the device was fabricated. The current-voltage relationship for this device is given in **Fig. 3.14**. The j_{SC} is measured to be 3.65 mA/cm^2, comparing well with the predicted j_{SC} of 3.79 mA/cm^2 using wavelength-dependent optical constants (as opposed to the results with the average optical constant of the cathode shown in **Fig. 3.13**). Also shown in **Fig. 3.14** are the performance characteristics for alternative inverted OPV cells with Al (device 1) and Mg:Ag (device 2) in-coupling electrodes. Although the OPV structure differs slightly between cells, a decrease in j_{SC} is observed as expected from the contour plot of **Fig. 3.13**.

These results demonstrate that thin metal films are effective as a light in-coupling electrode for inverted OPVs, although there is a considerable drop in power efficiency of 44% when compared to the glass-ITO structure. Note that this drop is similar to the recent work of Tong et. al. (2008) that demonstrated an inverted OPV structure with an ITO light in-coupling electrode which showed a 38% drop in efficiency. However, as opposed to that work, here the undesirable ITO has been eliminated. In addition, even though the inverted metal-organic-metal OPV cell sees a considerable drop in performance, the next chapter will show that external optical coatings provide greater gains for this structure than coatings applied to the ITO-based OPV cells, making the performance of a top-illuminated metal-organic-metal structure more competitive with the conventional "bottom-illuminated" ITO-based devices. Beyond the removal of the undesirable ITO, additional benefits include the ability to use low-cost opaque substrates (as well as fiber substrates, as discussed in later section), making the top-illuminated thin metal electrode device geometry very attractive for future study.

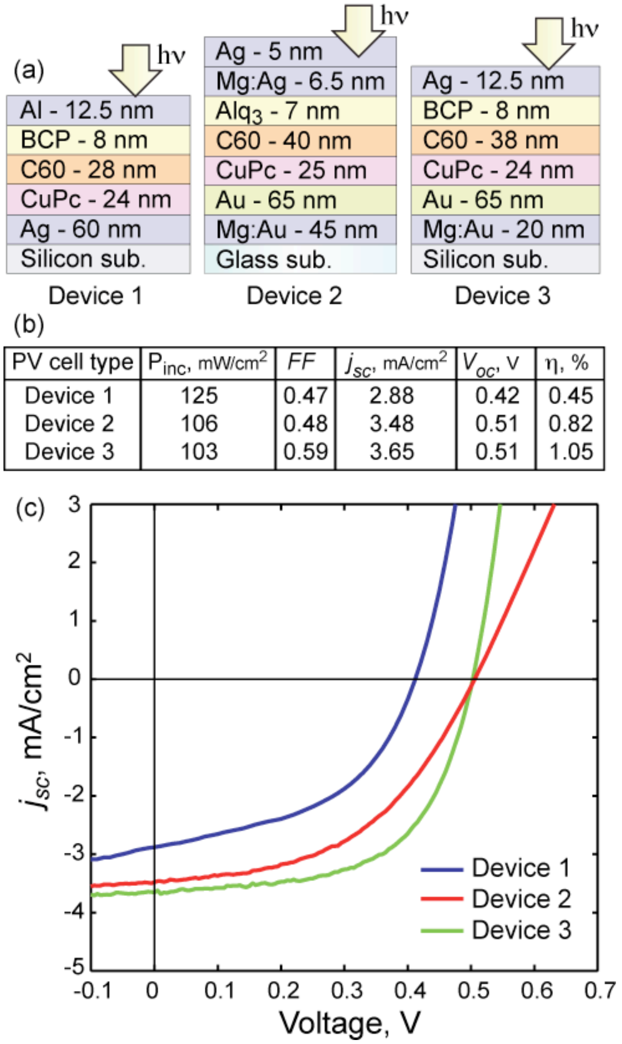

PV cell type	P_{inc}, mW/cm^2	*FF*	j_{sc}, mA/cm^2	V_{oc}, V	η, %
Device 1	125	0.47	2.88	0.42	0.45
Device 2	106	0.48	3.48	0.51	0.82
Device 3	103	0.59	3.65	0.51	1.05

Figure 3.14. (a) The structure of three inverted OPV cell structures under consdieration. (b) A summary of the performance characteristics of the three devices in (a). (c) Current-voltage relationship for the three devices under the incident light intensities (P_{inc}) provided in (b).

3.5 Conclusion and outlook for OPVs utilizing thin metal electrodes

In summary, we have shown that low-cost thin metal films can replace ITO in OPV cells, without the need for patterning. Our analysis examines a range of metals and metal oxides, showing systematically that Ag performs well as a transparent, conductive electrode material. This is due to a combination of its desirable refractive index and extinction coefficient, its low sheet resistance and its low contact resistance with the adjacent organic layer studied here. Optical modeling of OPV devices suggests that a metal electrode may actually outperform ITO in a BHJ cell, albeit subject to the specifics of the electrode surface energy and the desired phase separation of the active layers. Further improvements in photocurrent may be possible via modification of the optical constants and/or surface plasmon mediated energy transfer (e.g. through texturing and/or patterning). Unpatterned metal films, however, are likely to be vastly superior to most other transparent conductor alternatives in terms of materials and processing costs as well as operational reliability. Moreover, the fabrication simplicity enables device structures that would be difficult to realize with other proposed transparent conductors, such as devices deposited on non-planar and opaque substrates.

CHAPTER 4

EXTERNAL DIELECTRIC COATINGS FOR IMPROVING EFFICIENCY OF ORGANIC PHOTOVOLTAIC CELLS

4.1 Introduction and motivation

Photocurrent generation in OPV devices proceeds via a multi-step process, the overall efficiency of which is in part limited by the trade-off between efficient optical absorption and exciton diffusion to the electron donor-acceptor (DA) interface, where charge dissociation occurs. This limitation, as discussed in **Chapter 2**, is thought to originate from the short exciton diffusion length relative to the optical absorption length in compounds typically employed in organic PV cells. For a flat heterojunction structure, an optimal balance between light absorption and exciton diffusion is achieved for thin (on the order of 50 nm) organic layers. This, however, places one of the organic layers (e.g. the electron acceptor) close to an optically thick metallic electrode (e.g. the cathode), where the electromagnetic field amplitude quickly approaches zero, hindering the magnitude of the amplitude across the thin active organic layer, and reducing the net rate of exciton generation near the DA interface. Several approaches to simultaneously improve light absorption and exciton diffusion have been investigated, including the use of materials with longer exciton diffusion lengths (Shao, Yang, 2005), bulk heterojunction (BHJ) morphologies (Peumans et al., 2003a; Coakley, McGehee, 2004), exciton-blocking layers (EBLs) (Peumans et al., 2000; Rand et al., 2005; Kim et al., 2006), light trapping (Peumans et al., 2000), and sensitizing layers (Ishikawa et al., 2004). In these approaches, however, the optical field intensity near the DA interface cannot be controlled independently of the electrical properties of the active organic layers that are sandwiched between the electrodes limiting the optimization parameter space.

Here we model and experimentally demonstrate a device structure incorporating *external* dielectric layers that can increase the optical field intensity at the DA interface without any modification to the (internal) active organic layer structure. The capping layer is similar in optical function to conventional anti-reflection coatings used in optics (Nelson, 2003), yet differs in that it tunes the phase of incoming radiation to maximize the field intensity near a thin film organic PV cell's donor-acceptor interface with the ultimate goal of improving current generation.

In this chapter, a single-layer external dielectric coating is first shown to enhance energy conversion in an OPV cell with metal anode and cathode under narrow-band illumination by engineering the optical field intensity distribution in the device. Transfer matrix simulations are used to model the optical field intensity distribution within the device, which is then confirmed by an *in-situ* measurement of the photocurrent during growth of the external coating. A needle optimization method is then introduced to design multi-layer coatings for OPV cells under broadband illumination. The design principles are applied to the metal-organic-metal structures discussed in **Chapter 3**, both for light coupling through a glass substrate and for light coupling from the free-space side. It is shown that the coatings are much more effective when applied in conjunction with the semitransparent metal electrode than with an ITO electrode.

4.2 Single external dielectric coating – proof of concept

Compare an archetypal OPV cell structure shown in **Fig. 4.1(a)** to an alternative structure illustrated in **Fig. 4.1(b)**. In the latter, a thick metal anode replaces ITO, while the cathode is a semitransparent Al and Ag film, followed by a dielectric cap; light enters the cell through the cathode.

In order to analyze the different effects of the layer structure on device optical properties, we first calculate the optical field intensity profiles using the transfer matrix method developed in **Chapter 2**, assuming monochromatic light propagating normal to the device layers and typical optical constants for the active organic layers and organic dielectric cap (Pettersson et al., 1999; Rand et al., 2004). The calculated field intensity profiles, normalized to the incident free space field intensity, are superimposed on the structures in **Fig. 4.1**. Of particular importance for device efficiency is the normalized optical field intensity at the DA interface, $|E_{DA}|^2$.

The detailed structure used in the first simulation is shown in the inset of **Fig. 4.2**, and consists of: 1 mm glass substrate, 70 nm of aluminum (Al), 5 nm of nickel (Ni), 15 nm of CuPc, 50 nm of C_{60}, 3 nm of Al, 8 nm of Ag, and a capping layer (cap) of variable thickness. If no absorption or photon down-conversion takes place in the capping layer, $|E_{DA}|^2$ will vary periodically with the capping layer thickness (t_{CAP}) due to optical interference effects, as shown in **Fig. 4.2**. Note that $|E_{DA}|^2$ for a capping layer thickness of 47 nm is 30% higher than for the device without the capping layer, suggesting that a similar increase in photocurrent and conversion efficiency can be expected.

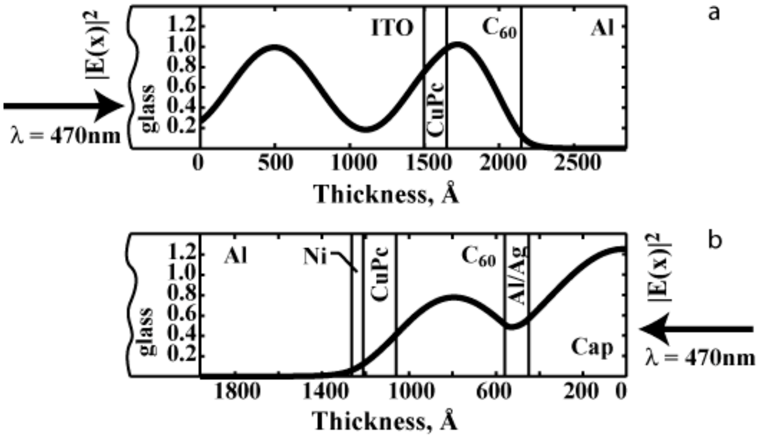

Refractive Index (λ = 470nm)

$n_{glass} = 1.42$	$n_{Al} = 0.69 + i*5.7$	$n_{CuPc} = 1.6$
$n_{Cap} = 1.7$	$n_{ITO} = 1.937 + i*0.016$	$n_{C60} = 2.2 + i*0.35$
$n_{BCP} = 1.8$	$n_{Ag} = 0.13 + i*3.07$	

Figure 4.1. Schematics of (a) an archetypal organic photovoltaic device that uses an ITO anode on a glass substrate, and (b) an alternative device structure with metal anode and cathode, capped by a 45 nm thick dielectric layer having a dielectric constant n_{CAP} = 1.7. Superimposed is the normalized electric field component of the optical field intensity, $|E_{DA}|^2$, throughout the structure, calculated using a thin-film transfer matrix model. For the structure in (a), $|E_{DA}|^2 = 0.98$. For the structure in (b), $|E_{DA}|^2 = 0.41$.

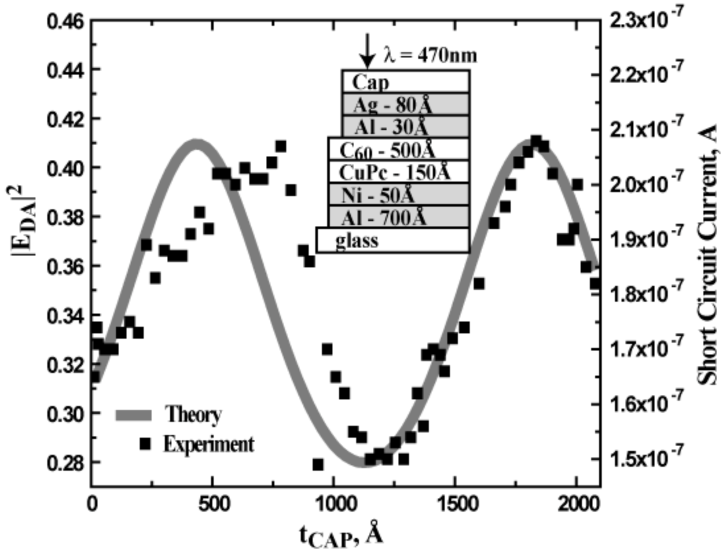

Figure 4.2. A plot of the calculated value of $|E_{DA}|^2$ versus the dielectric capping layer thickness, t_{CAP}, in the device structure shown in the inset (solid line). Superimposed are the data points corresponding to the short-circuit photocurrent, I_{SC}, measured *in-situ* during the growth of the capping layer (Alq_3) under constant illumination at λ = 470 nm.

To verify this prediction, we performed an in-situ measurement of the photocurrent produced by a PV cell with the same structure during the deposition of the capping layer. Here the organic PV cell layers were grown at 10^{-6} Torr at deposition rates of 0.2 and 0.1 nm/s for the organic and metal layers, respectively. The capping layer consisted of aluminum hydroxiquinoline (Alq_3) deposited at an average rate of 0.3 nm/s. The illumination source was a blue InGaN light-emitting diode (LED) with a peak wavelength of 470 nm and a spectral half width of 25 nm. The excitation wavelength, which corresponds to the peak absorption of C60 within the visible portion of the spectrum (Pettersson et al., 1999), is negligibly absorbed by Alq_3 (Sokolik et al., 1996). The current-voltage characteristic was measured by scanning the voltage from –0.2 V to 0.7 V at 20-second intervals.

The measured short circuit current is plotted versus t_{CAP} in **Fig. 4.2**, superimposed on the plot of the calculated $|E_{DA}|^2$. The measured photocurrent closely follows the predicted $|E_{DA}|^2$ curve, confirming the linear dependence of photocurrent on intensity near the DA interface. A 28% peak increase is observed in the photocurrent compared to the uncapped device. We note that the integrated field intensity over the C60 layer has a periodic behavior similar to $|E_{DA}|^2$, which is expected due to the long diffusion length (L_D) of excitons in C60 (Shao, Yang, 2005). Nevertheless, for many organic PV materials and structures that have smaller values of L_D, $|E_{DA}|^2$ remains the key design parameter for optimization. The observed small phase difference between the experimental data and theoretical prediction for small values of t_{CAP} is attributed to the deposited film roughness, which is not accounted for in the simulation.

To estimate the extent to which this approach can be used for high efficiency organic PV devices, we now extend our model to predict $|E_{DA}|^2$ for an archetypal double heterojunction cell that includes an EBL. The proposed device structure is shown in the inset of **Fig. 4.3**. It includes a 9 nm Ag anode, the same in-coupling electrode thickness used previously in **Fig. 3.11**. For monochromatic illumination at $\lambda = 470$ nm, the simulation predicts that the thickness and refractive index of the capping layer can be chosen such that the value of $|E_{DA}|^2$ in the device with metallic anode and cathode exceeds that in an analogous device that employs an ITO anode. This approach is extrapolated to design multi-layer coatings for broadband illumination in the next section.

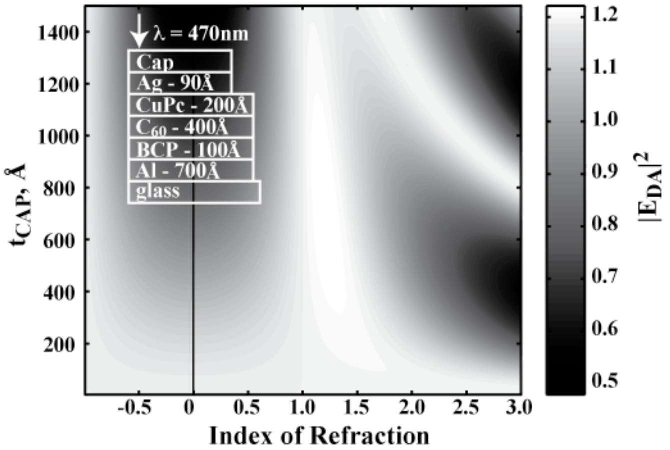

Figure 4.3. A gray-scale map of $|E_{DA}|^2$ in a high efficiency double heterojunction organic photovoltaic device (the structure of which is shown in the inset) versus the thickness and index of refraction of the dielectric capping layer. The plot was obtained by a thin-film transfer matrix calculation for incident light having 470 nm peak wavelength. The maximum $|E_{DA}|^2$ is 1.22 for a cap thickness of 72 nm and n_{CAP} = 1.21. For a similar device structure with a 150 nm ITO anode, $|E_{DA}|^2$ is 1.04.

4.3 Design and optimization of multilayer coatings for broad-band absorption

While a single layer can produce a peak in the optical field intensity at the donor-acceptor interface for a narrow range of wavelengths, multilayer coatings are required to achieve broadband optimization of intensity. Optical multilayer coatings often use 2 materials, one with a high index of refraction ($\tilde{n}_H$) and one with a low index ($\tilde{n}_L$) to keep the system as simple as possible (Heavens, 1965). Multilayer coatings using 2 materials having a large difference in index of refraction can combine to closely mimic a single layer with an index of refraction between $\tilde{n}_H$ and $\tilde{n}_L$. As such, the coating has the greatest flexibility in design with a material system that has the largest difference in index of refraction as possible. In the remainder of this chapter, we use the dispersion-free values of refractive index $\tilde{n}_H$ = 2.2 and $\tilde{n}_L$ =

1.35. These values are common in optical filter design and are close to the material optical properties of CeO_2 (or TiO, ZnS) and MgF, respectively (Heavens, 1965; Lissberger, 1970).

Unlike optical filters, the broadband external coating for an organic solar cell should be designed not to match a specific far-field transmission or reflection profile, but rather to maximize the output short-circuit current of the device. For each PV cell structure, the optimization of the coating is unique for a given wavelength of incident light. Ideally, the active layers and coating would be optimized simultaneously, but in practice the optical coating design is subordinate to the more limiting electrical properties of the active layers. For strongly absorbed wavelengths, the device cavity transmittance is maximized while for weakly absorbed wavelengths, resonance (light trapping) within the device cavity is maximized. In addition, the field intensity for a given wavelength should be optimized spatially to maximize overlap with the layer(s) where that wavelength is strongly absorbed. In the following section, a needle optimization design scheme is used to design multi-layer external coatings that significantly improve the predicted performance of organic solar cells.

4.3.1 Needle Optimization

Modern complex multilayer optical coating designs are typically developed using numerical techniques, of which needle optimization or a close variant is the most common (Agrawal, 2008). This method can be used either to refine a given design that is an approximation of the desired performance or to synthesize a solution from scratch (Sullivan, Dobrowolski, 1996).

To begin the coating optimization procedure, a merit function for the coating design must be defined. This merit function is the difference between the user-defined ideal performance (target) and the calculated performance; a common merit function is of the form:

$$(4.1) \qquad f(Q)=\left\{\frac{1}{m}\sum_{j=1}^{m}\left[\frac{Q(\lambda_j,\phi_j)-\tilde{Q}_j}{\Delta Q_j}\right]^2\right\}^{1/2} .$$

In this expression Q_j and $Q(\lambda_j,\phi_j)$ represent the *j*th target and calculated quantity of interest, respectively, and ΔQ_j is the associated design tolerance, all for m quantities (Sullivan, Dobrowolski, 1996). Here we use a merit function that is based on the short-circuit current density (j_{SC}) of a solar cell, where the target j_{SC} would be 100% η_{EQE} for AM1.5G illumination. For incident wavelengths between 300-900 nm (i.e. the visible spectrum), this would yield $j_{SC} \sim 35$ mA/cm^2. We therefore define Q_j = S(λ_j), $Q(\lambda_j,\phi_j)$ = $\eta_{EQE}(\lambda_j)$S(λ_j) with m = 120 leading to a wavelength increment of 5 nm (where S is the wavelength-dependent photon flux). The design tolerance is a constant across all *j* and is arbitrary and set to 1.

With the merit function thus defined, we performed an optimization process for the external coating design as shown in **Fig. 4.4**. The process starts with two layers (one high-index and one low-index) with a random thickness (between 50 nm to 400 nm). After calculating the merit function for a predetermined number (e.g. 500) of layer thicknesses, the best performing 2-layer coating is selected. The thickness of each layer is then incrementally varied, using a gradient of steepest decent method to minimize the merit function. When this point is reached, a thin layer (needle) is scanned through each layer of the coating, with the needle having an index of refraction that is opposite of the layer through which it is scanned. The position of the needle that again minimizes the merit function defines the location of a new layer (and the splitting of a current layer). The layer thicknesses of this new coating stack are then independently varied to minimize the merit function once again, and the process repeats.

During this optimization, we set the thickness of the needle insert and the minimum layer thickness to be 3 nm, which represents the thinnest layer that can be practically achieved. After the refinement process converges, any layers that are less than this minimum thickness are automatically removed, and the adjacent layers are combined. If a local minimum in the design optimization is reached, yet the design is still far from the set criteria, then a method known as tunneling may be applied. In this procedure, the thickness of one of the layers is changed significantly, so that the design "tunnels" from one local valley of the design space to another deeper one (which hopefully holds the global minimum). Alternatively, an additional thick bilayer is added on top of the stack and the system once again refined (Agrawal, 2008). The entire optimization routine is run multiple times with different starting layer thickness in order to test convergence.

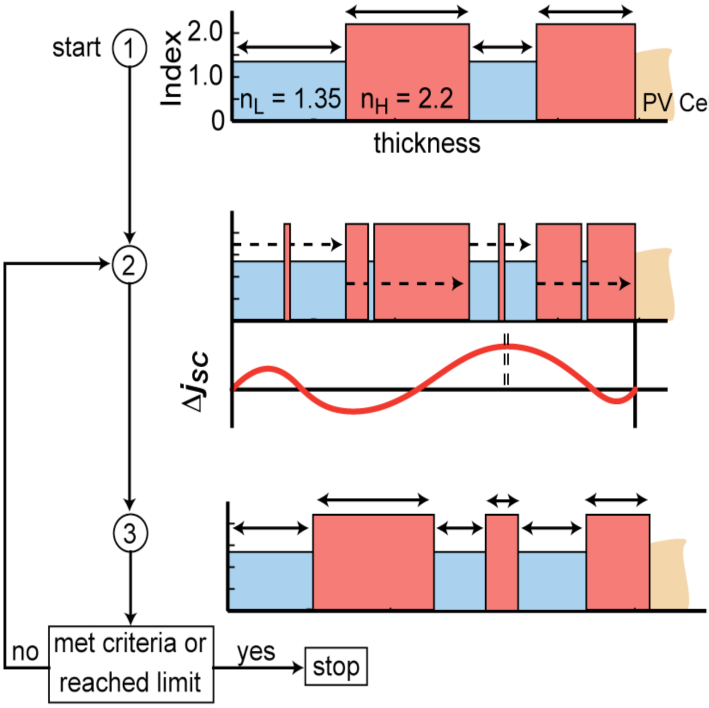

Figure 4.4. Steps in the needle optimization method. *Step 1:* starting with a given number of layers with specified thicknesses and refractive indices, independently adjust the layer thicknesses to minimize the user-defined merit function (which in this case maximizes j_{SC}). *Step 2*: scan a needle of opposite index of refraction through the layer stack until it reaches the position that again minimizes the merit function. *Step 3*: Adjust the thicknesses of all layers to once again minimize the merit function. After Step 3, check to see if the design criteria or a design limit has been reached, and either stop running the program or make necessary adjustments and go back to Step 2. Necessary adjustments may include subtracting a layer that is too thin; see **Section 4.3.1** for more details.

4.4 Broadband dielectric coatings applied to thin metal electrodes

In this section, multilayer external dielectric coatings are designed for both glass-ITO and metal electrode OPV cells. External coatings can improve j_{SC} in both cell types, but it will be shown that they are particularly effective for cells that employ a semitransparent metal electrode. This is due to the fact that while thin metal films have a lower transmittance than ITO, this poor transmittance is dominated by high reflectivity rather than absorption; losses to heat are minimal. The dielectric coating can be designed to soften the larger index step more effectively of the relevant interface (electrode-substrate, or electrode-air), and improve optical in-coupling.

4.4.1 Glass substrate – "bottom-illuminated" OPV cells

In **Chapter 3**, a thin Ag electrode of 9 nm thickness was shown to be an effective replacement for ITO. The metal-electrode OPV (ME-OPV) device was shown to have a *FF* comparable to the ITO-OPV device, the V_{OC} was shown to be 14% greater and the j_{SC} was shown to be 14% lower. Illuminations of the device structures for the ITO-OPV cell (Type I) and ME-OPV cell (Type II) are provided again in **Fig. 4.5**, with performance characteristics provided in **Fig. 4.6**. As discussed in **Chapter 3**, the decrease in j_{SC} from cell Type I to Type II is largely due to the decreased transmittance of the metal film compared to ITO. However, as noted previously, the full optoelectronic model we have developed provides a more accurate comparison between devices, with the η_{EQE} spectra for Type I and Type II shown in **Fig. 4.6**. This model can also be used to calculate the fraction of energy absorbed by the semitransparent metal film and ITO, as shown in **Fig. 4.8**. The fact that these two fractions are similar suggests that reflection and not absorption in the metal results in the lower j_{SC}. Our aim is therefore to recover this reflected portion of light using a broadband optical coating.

For both ME-OPV and ITO-OPV cells, we place an optimized multilayer dielectric stack (coating) between the glass substrate and the light in-coupling electrode, giving cell Types III and IV, as illustrated in **Fig. 4.5**. While the stack is not on the free space side of the cell as in **Section 4.2**, it remains on the side from which light is incident. The stack is designed using the aforementioned needle optimization, limiting the total number of dielectric layers limited to 8 and using two values of dispersion-free refractive index: 1.35 and 2.2 (Dobrowolski et al., 1996). Simulation results confirm that negligible performance gains are realized when using more than 8 layers. A comparison of the anode far-field transmission spectra and η_{EQE} spectra for Type I, II, III, and IV layer structures is shown in **Fig. 4.6**. For far-field transmission we assume that a semi-infinite slab of the archetypal electron donor molecule CuPc (neglecting the extinction coefficient) caps the anode. Applying the dielectric films to the metal electrode configuration leads to vastly improved transmittance. However, note that improving transmittance does not necessarily lead to increased η_{EQE}, as shown for the Type IV cell for $\lambda \approx 500$ nm. This further supports the use of j_{SC} rather than far-field transmittance as the parameter to optimize when designing coatings for OPV cells. The general trend observed in **Fig. 4.6(c, d)** is that the η_{EQE} is improved most for wavelengths within the strongest intrinsic absorption bands of the organic layers (~350-500 nm; 550-750 nm). This is due to the fact that smaller changes in the optical field intensity at these wavelengths result in large changes in exciton generation rate and subsequently j_{SC}.

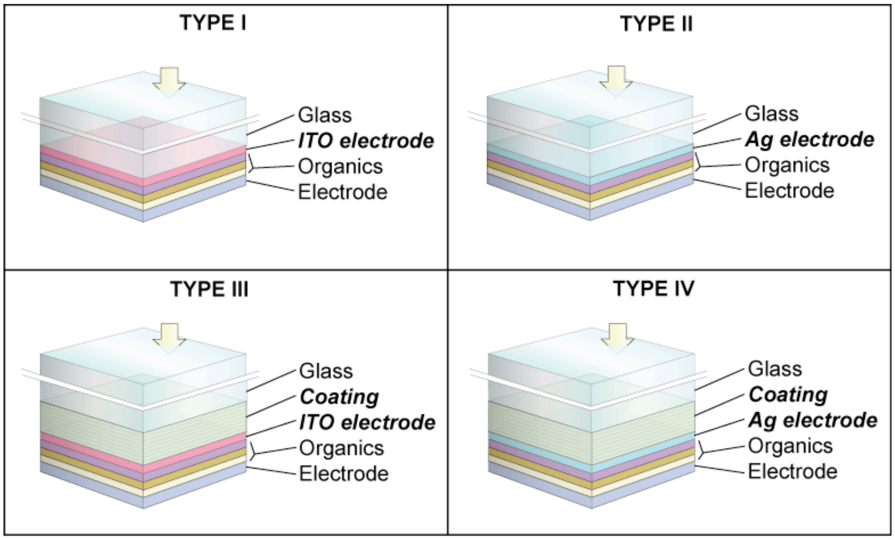

Figure 4.5. Illustration of the four OPV cell structures of interest in **Section 4.4.1**. Type I and III are OPV cells that utilize an ITO light in-coupling electrode, with cell Type III also employing dielectric coating between the electrode and glass substrates. Type II and IV OPV cells use Ag as the light in-coupling electrode, with Type IV employing the dielectric coating. After the transparent electrode, the design of all OPV cells is the same and includes: 24 nm CuPc, 38 nm C60, 5 nm BCP and 90 nm Ag.

Figure 4.7 shows the predicted j_{SC} for the Type I, II, III, and IV devices. It is predicted that the photocurrents of the Type III and IV devices become equivalent when the Type IV cell utilizes a 9 nm Ag anode. Based on the previously discussed experimental evidence that the Type II cell has a 14% larger V_{OC} than the Type I cell, the Type IV device is expected to be 14% more efficient than the optimized Type III cell.

Figure 4.7 also shows the j_{SC} of the Type IV cell with its coating optimimzed at a range of Ag anode thicknesses. Increasing the Ag anode to 12 nm maintains 95% of the j_{SC} of the Type III cell. The ability to achieve relatively high photocurrents with increased metal thickness enables reduced sheet resistance, improved film uniformity, resistance to corrosion, and improved reliability.

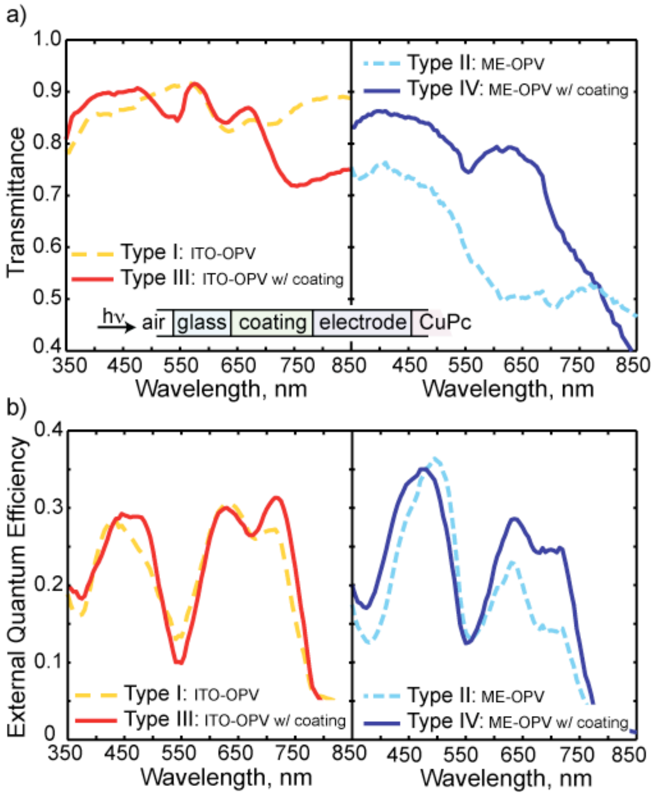

Figure 4.6. a) The far-field transmittance into an infinite CuPc film (neglecting CuPc absorption) by ITO and metal electrodes on glass with and without an optimized coating layer. b) The external quantum efficiency spectrum for ME-OPV and ITO-OPV devices with and without an optimized coating. These device structures are given in **Fig. 4.5**, with a 12 nm Ag anode for the ME-OPV cell. The plots also correspond to the predicted short-circuit current in in **Fig. 4.7**.

PV Type	I	II	III	IV
j_{SC}, mA/cm^2	6.41	5.92	6.54	6.70
η, %	1.85	1.99	1.88	2.25

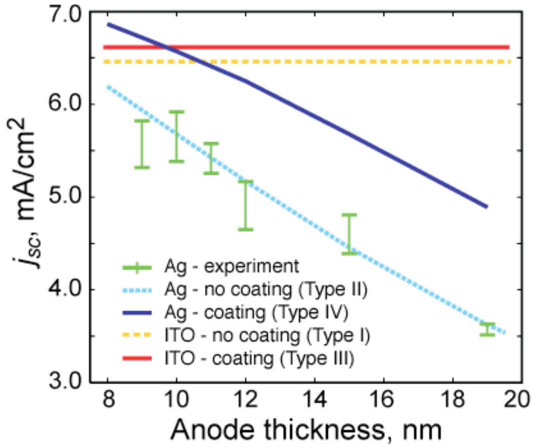

Figure 4.7. (a) Predicted j_{SC} and η_p (using experimental values of V_{OC} and FF) for the 4 cell types considered in **Section 4.4.1**. The Ag anode thickness for Types II and IV is 9 nm. (b) Predicted j_{SC} as a function of the semitransparent Ag thickness.

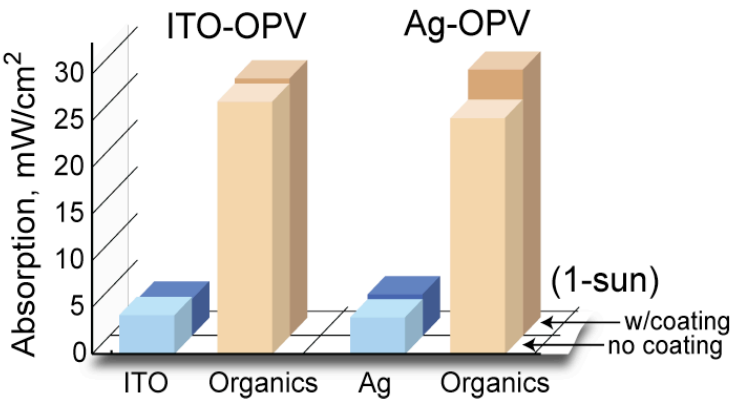

Figure 4.8. Predicted absorption in the electrode and active organic layers for Type I, II, III and IV OPV cells.

4.4.2 Coatings applied to top-illuminated OPV

Similar to the procedure used above for the thin metal electrode device on glass, the multilayer coating design process can also be applied to top-illuminated OPV cells in which the coating is deposited after the active layers and electrodes. The most highly optically mismatched (reflective) interface is now between air and the electrode. Again, we use the needle optimization method to design a multilayer coating for the best-performing top-illuminated OPV cell of **Chapter 3.4** (**Fig.3.14(c)**). For this device our model predicted j_{SC} = 3.79 mA/cm^2, which closely matched experimental results. Applying an 8-layer coating design to the device structure given in **Fig. 4.9** results in a predicted j_{SC} of 4.94 mA/cm^2, which represents an improvement of 30%. For top-illuminated devices, the coating is useful not only as a means to optimize the optical optimize the optical field intensity distribution, but also as an environmental barrier to improve device longevity.

4.5 Summary

External dielectric coatings were shown to substantially improve the light in-coupling efficiency of OPV cells, especially if both electrodes are metallic. Simulations of coupled optical and electrical transport in coated OPV cells were verified by *in-situ* measurements of the photocurrent during growth of a capping layer on an OPV cell. Multilayer coatings were designed using a needle optimization procedure to maximize solar cell performance under broadband AM1.5G solar illumination. The performance of an OPV cell utilizing a 9 nm Ag semitransparent electrode and an optimized 8-layer coating was shown to be nearly 20% better than the archetypal ITO-OPV cell also with an optimized dielectric coating. In addition, the use of an external coating improved the performance of a top-illuminated OPV cell by over 30%. The ability to replace the ITO anode of an OPV cell by a thin metal film potentially improves its overall mechanical properties (Lewis et al., 2004) and can lower its substrate cost. Furthermore, the ability to couple light in through the top-deposited cathode allows for a wider range of OPV cell designs, such as devices deposited directly onto nonplanar substrates (such as fiber) or opaque substrates (such as metal foils).

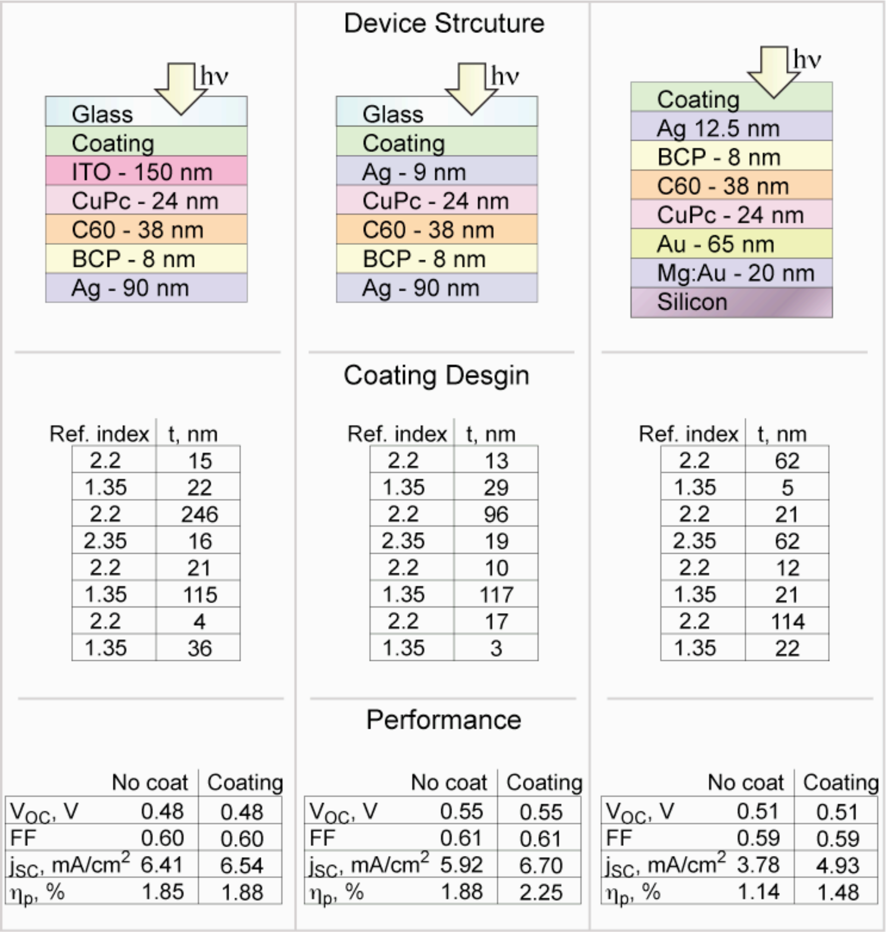

Ref. index	t, nm
2.2	15
1.35	22
2.2	246
2.35	16
2.2	21
1.35	115
2.2	4
1.35	36

Ref. index	t, nm
2.2	13
1.35	29
2.2	96
2.35	19
2.2	10
1.35	117
2.2	17
1.35	3

Ref. index	t, nm
2.2	62
1.35	5
2.2	21
2.35	62
2.2	12
1.35	21
2.2	114
1.35	22

	No coat	Coating
V_{OC}, V	0.48	0.48
FF	0.60	0.60
j_{SC}, mA/cm^2	6.41	6.54
η_p, %	1.85	1.88

	No coat	Coating
V_{OC}, V	0.55	0.55
FF	0.61	0.61
j_{SC}, mA/cm^2	5.92	6.70
η_p, %	1.88	2.25

	No coat	Coating
V_{OC}, V	0.51	0.51
FF	0.59	0.59
j_{SC}, mA/cm^2	3.78	4.93
η_p, %	1.14	1.48

Figure 4.9. Summary of the coating optimization applied to the OPV cells considered in **Sections 4.3 and 4.4**. The left panel is the control ITO-glass OPV cell, and the center panel replaces the ITO electrode with a 9 nm Ag electrode. At right, the top-illuminated OPV structure, coating design, and performance results are given.

CHAPTER 5

FIBER SHAPED ORGANIC PHOTOVOLTAIC CELL

5.1 Introduction and motivation

In this chapter, we demonstrate and analyze in detail thin-film photovoltaic cells based on small molecular weight organic compounds that are deposited concentrically on long fibers. The ability to fabricate semiconductor devices on a fiber substrate, coupled with the commodity scale of fiber and textile technologies, can have significant implications for realizing cost-effective, large-scale energy conversion. Previous attempts at fiber-shaped PV cells discussed in detail in **Chapter 1,** include fibers coated with polymer-based active layers that receive light from the fiber core.(Liu et al., 2007) This limits the amount of organic material participating in photocurrent generation.

Here, we examine a fiber-based organic PV (OPV) cell architecture is examined in which light enters the cell through a semitransparent outer electrode, as shown in **Fig. 5.1**. We focus on smal molecule organic materials, noting that others have subsequently extended our work in this geometry to ploymer-based active layers (Lee et al., 2009). Using a combination of modeling and experiments, we quantify device performance analyze in detail the unique features and requirements of fiber-based OPV devices that are important for scale-up.

5.2 Fiber-based organic solar cell design

As discussed earlier, an archetypal PHJ-OPV cell consists of light absorbing organic thin films sandwiched between two electrodes, where light enters the active layers after passing through a transparent substrate pre-coated with an ITO anode (Tang, 1986). A fiber-based device can be realized by depositing a similar layer structure concentrically around a fiber substrate, by growth from solution or vapor phase. The fiber-based OPV devices in this work were fabricated by VTE of the organic and metallic films onto a polyimide coated silica fiber. VTE is a line-of-sight deposition process, requiring the fiber to be rotated about its axis during deposition to obtain conformal coatings. The vacuum-compatible apparatus we designed and assembled to rotate the fiber is shown in **Fig. 5.2,** along with the VTE system in which it is mounted.

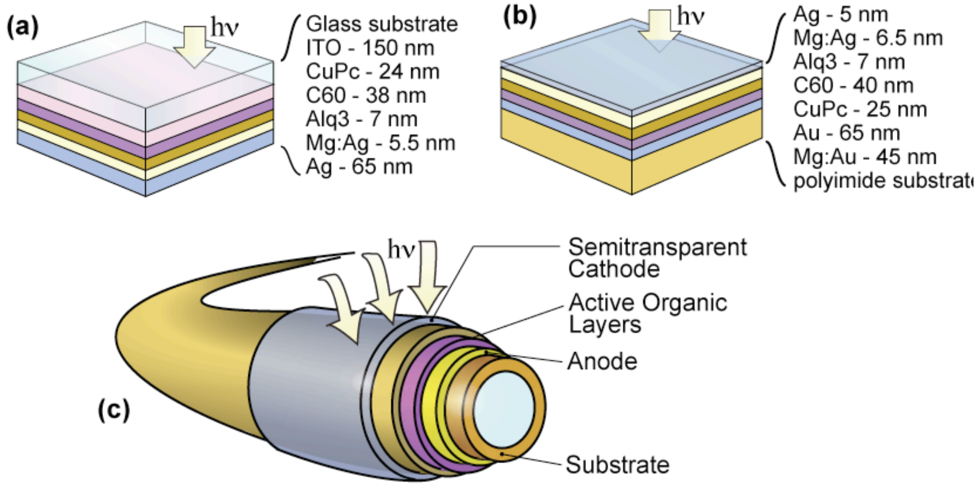

Figure 5.1. Illustration of the 3 types of PV cells fabricated and analyzed in this chapter: (a) an archetypal organic solar cell deposited onto ITO-coated glass (b) a top-illuminated planar device on glass or flexible polyimide substrate, (c) a device on a flexible polyimide-coated silica fiber substrate, with the device layers deposited concentrically around the fiber. The details of the device structure are provided for each cell type. The fiber structure (c) has the same layer structure as (b).

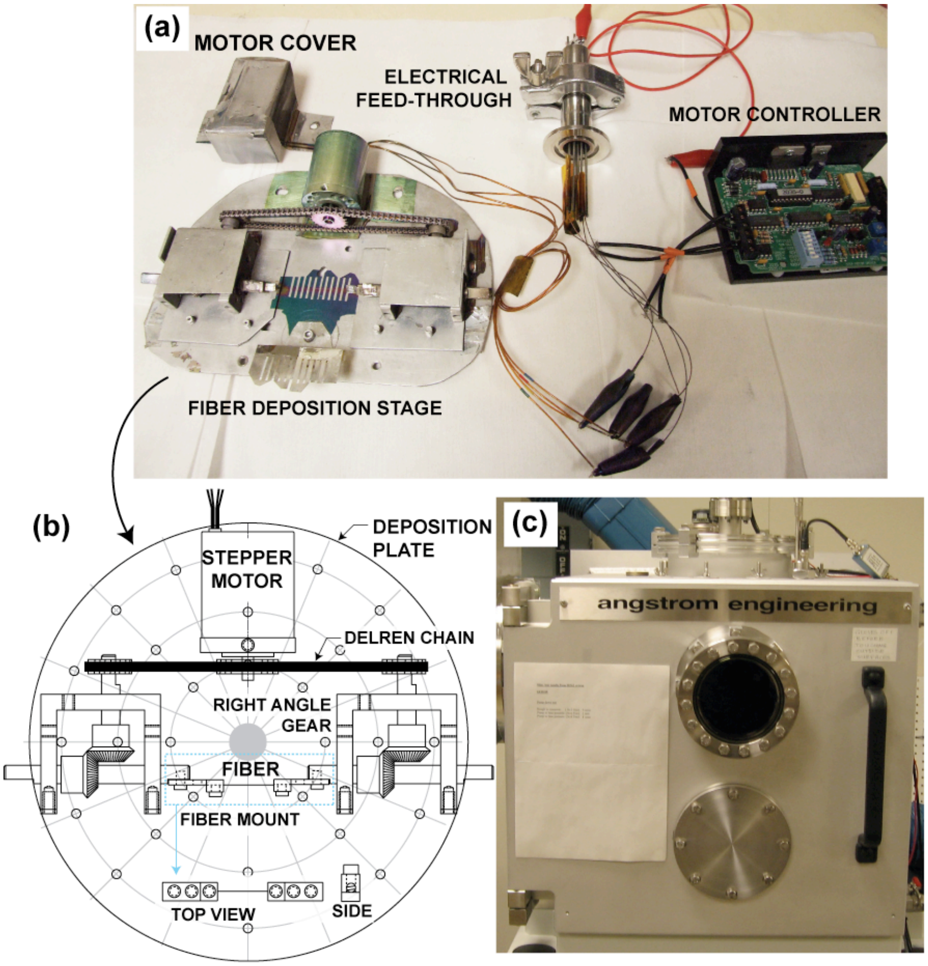

Figure 5.2. Modular fiber rotation stage. (a) A photograph of the components constituting the fiber rotation stage used with the Angstrom A-mod vacuum thermal evaporation system. Components include: fiber-mounting hardware, rotation motors and gear train, electrical feedthrough, and stepper motor. (b) Top-view schematic of the deposition stage as it sits on the planar VTE deposition puck. (c) Image of the vacuum thermal evaporator in which the deposition stage is placed for device fabrication. During layer deposition, the fiber rotates at roughly 30 rpm.

For large-area fiber PV applications, it is advantageous to couple light into the active layers through the outer-most (rather than inner-most) electrode, as shown in **Fig. 5.1(c)**. Planar analogues of such top-illuminated OPV cells have been previously studied (O'Connor et al., 2006; Oyamada et al., 2007), and several aspects of the top-illuminated OPV cell designs developed in **Chapter 3** are incorporated here. For a direct performance comparison of the planar and fiber geometries, OPV devices having identical layer sequences and thicknesses were deposited on planar glass, planar polyimide, and fiber polyimide/silica substrates. A conventional OPV cell was also deposited onto ITO-coated glass (through which light was incident) in order to provide reference point for the materials purity and illumination conditions of our laboratory. All devices with the exception of the ITO-glass device consisted of the following layer sequence: 25 nm Mg, 20 nm Mg:Au co-deposited with a volume ratio of 1:1, 65 nm Au, 25 nm CuPc, 40 nm C60, 7 nm Alq_3, 6.5 nm Mg:Ag co-deposited with a volume ratio of 7:1 and finally 5 nm Ag. The thickness values account for the rotating fiber substrate and correspond to actual thicknesses of the layers in each device shape. This OPV structure is similar to the archetypical double heterojunction small molecule design (Peumans et al., 2003b), with several modifications described as follows. The magnesium in the anode promotes adhesion of gold to the substrate; the gold anode itself was UV-ozone treated for 5 minutes prior to the deposition of the organic layers to facilitate charge collection (Rentenberger et al., 2006). In OPV cells, bathocuproine (BCP) is typically employed as an exciton blocking layer and an optical spacer between C60 and the adjacent metal electrode. The inverted metal electrode organic solar cell presented in **Chapter 2** effectively used BCP followed by silver. For the fiber substrates, however, OPV cells made with BCP were plagued by low fill factors. Thin films of BCP deposited by thermal evaporation are typically amorphous, but BCP easily crystallizes, which reduced device performance (Song et al., 2005). we suspect that the intermittent deposition of the device layers onto the rotating fiber substrate promotes BCP crystallization, affecting the contact with the semitransparent electrode and considerably reducing device performance. As an alternative, Alq_3 has been shown to be an effective exciton blocking layer and has low optical absorption throughout the visible spectrum (Song et al., 2005). Therefore we replaced BCP with a thin Alq_3 layer. The Mg:Ag alloy forming the outer electrode has a low work function and has been shown to have low sheet resistance for very thin vacuum-deposited films (Oyamada et al., 2007). Finally, the silver capping layer was used to reduce oxidation of the cathode. The energy band structure for the device is given in **Fig 5.3(a)**.

One millimeter long cathodes were deposited through a shadow mask on a fiber substrate with a diameter of 480 μm (Shtein et al., 2003). The planar control device cells consisted of 1 mm diameter circles and 1 mm x 6 mm rectangles, also deposited through shadow masks. The ITO-glass control followed the same deposition process described above, but with an ITO rather than Mg:Au anode and an optically thick (reflecting) cathode consisting of 5.5 nm Mg:Ag alloy capped by 65 nm of Ag. All substrates were cleaned using a previously described process (Salzman et al., 2005). For testing, all devices were illuminated with a 150 W Oriel solar simulator with an AM1.5 optical filter.

5.3 Performance Characterization

Figure 5.3(b) compares the current density-voltage (*j-V*) characteristics of the fiber device to the analogous planar devices, with the PV performance details summarized in **Table 5.1**. For the fiber device, the incident illumination intensity and current density are based on the projected area of the fiber. The reduced short-circuit current density (j_{SC}) of the structures in which light enters through the outer electrode compared with the conventional ITO-based structure is attributed mainly to the reduced transmittance of the semitransparent electrode (**Fig. 5.4**).

The sheet resistance of the semitransparent metal electrode deposited on glass was measured using a four-point probe technique to be 11.3 Ohms/☐, which is comparable to that of the ITO electrode (10.5 Ohms/☐). Little difference is observed between the metal-organic-metal structure deposited on glass and on polyimide foil.

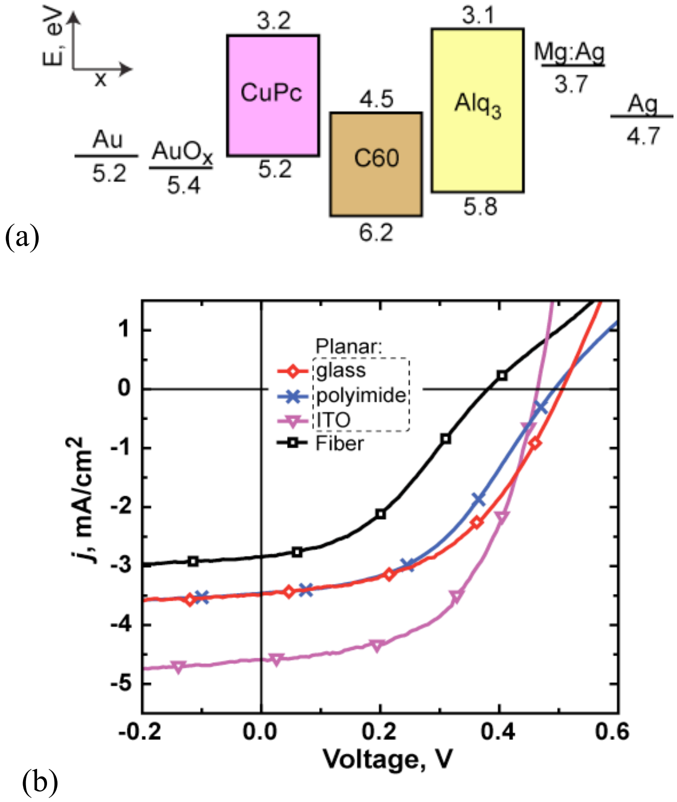

Figure 5.3. (a) Flat-band energy diagram of the demonstrated OPV cell deposited on a fiber substrate. (b) Plots corresponding to the data in **Table 5.1** and the normal incidence illumination conditions listed therein. For the ITO-based devices, light enters through the glass-ITO substrate, while in the other three devices, light enters through a semi-transparent metallic electrode.

Table 5.1. A summary of the performance parameters for all of the devices considered, where P_{inc} is the illumination intensity and η_{hemi} is the predicted efficiency averaged over a hemispherical range of illumination angles. The remainder of the data corresponds to the plot in **Fig. 5.3**. Note that η_p corresponds to power conversion efficiency at normal incidence.

	P_{inc}, mW/cm^2	j_{sc}, mA/cm^2	V_{oc}, V	*FF*	η_p, %	η_{hemi}, %
Planar substrate						
ITO-Glass	104	4.59	0.47	0.55	1.13	--
Glass	104	3.48	0.51	0.48	0.82	0.52
Polyimide	104	3.46	0.50	0.45	0.76	0.48
Fiber substrate	105	2.85	0.39	0.47	0.50	0.48

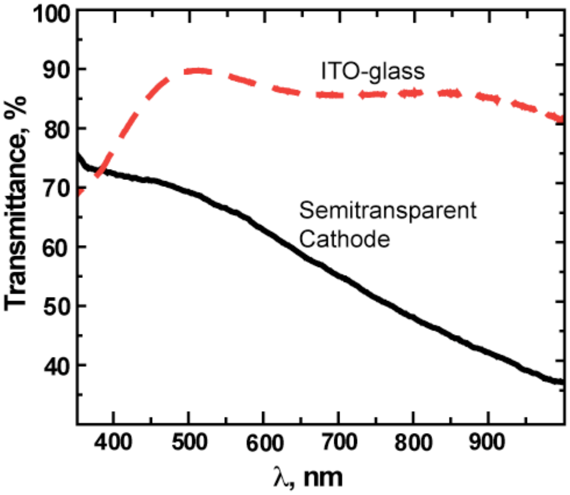

Figure 5.4. The transmittance of the semi-transparent cathode compared to that of the ITO-glass substrate. The semi-transparent electrode is 6.5 nm Mg:Ag co-deposited with a volume ratio of 7:1 followed by 5 nm Ag.

We now turn our attention to the differences between the fiber and planar devices having identical structures. The fiber-based PV cell exhibits lower power conversion efficiency (η_p) than the planar analogue when illuminated at normal incidence. This is attributed to a combination of shading, oblique light incidence at the curved fiber surface, and the intermittent deposition of material due to fiber rotation in the VTE chamber. The contributions from these effects are each considered independently below.

Shading in fiber-based OPV cells occurs when light is absorbed or reflected from the side of the fiber facing the light source. Under direct illumination of a single fiber, one half of the fiber circumference is shaded. In order to study this effect, an experiment was conducted using two planar glass substrate OPV cells. For the planar cells an aperture is placed directly above the cell controlling the amount of the device the device under illumination. Here shading refers to complete removal of incident light. **Fig. 5.5** shows the effect of shading on efficiency for the PV cell on the planar glass substrate.

The effect of shading on efficiency can be derived from a simplified equivalent circuit model for a solar cell resulting in (Quaschning, Hanitsch, 1996):

$$\eta_p = \eta_{p0}[1 + C \cdot \ln(1 - S_{Sh})], \tag{5.1}$$

where C is a fitting parameter and S_{Sh} is the fraction of the cell is shaded. Although this model was developed for inorganic solar cells, using $C = 0.073$ fits the experimental data of the planar top-illuminated OPV device well. A planar cell, half of which is shaded from incident light (similar to a single fiber under direct illumination) is predicted to be 5% less efficient than an un-shaded device. The fill factor (FF) for the shaded cell increases slightly, while both the open circuit voltage (V_{OC}) and the j_{SC} are reduced by approximately 4% from the un-shaded device. We conclude that shading would not be a limiting factor in fiber-based and woven solar textiles, in which it is expected that a considerable fraction of the active material will be shaded. In addition, certain fiber bundle architectures to be discussed later do not experience significant shading.

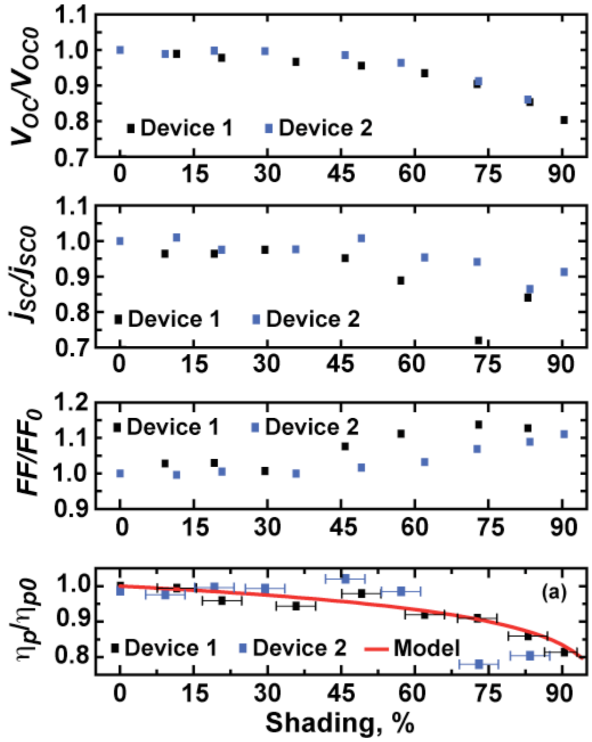

Figure 5.5. The four panels provide the characteristic performance parameters of two planar glass substrate OPV cells under varying amounts of shading. All four figures are normalized to performance under normal illumination. The data is corrected for degradation with a linear fit to the change in performance of the cells un-shaded at the beginning and end of testing. The bottom panel is a plot of the power efficiency (η_p) of the planar glass substrate cell with variation in the amount of device shaded normalized by the unshaded device efficiency (η_{p0}). The model approximates the effect of shading using a simplified equivalent circuit of a photovoltaic cell.

To understand the effect of off-normal incidence of light onto the surface of the fiber-OPV device, we model the fiber as a collection of differentially tiled planar cells collectively “seeing” 180º of illumination angles in θ and φ (defined in the inset of **Fig. 5.6(a)**). Each tile is assumed to have the characteristics of an experimentally measured planar cell illuminated at the corresponding angle of incidence. **Figure 5.6** shows the variation in operating parameters (FF, V_{OC}, and j_{SC}) and power efficiency (η_p) for the planar cell versus angle of incidence (ϕ); all parameters are normalized by the performance of the cell under normal incidence (ϕ = 0). After mapping the measured angle-dependent performance of the planar cell onto the fiber geometry, the fiber is predicted to be 13% less efficient than the planar cell at normal incidence. This predicted loss is dominated by reduced j_{SC} (10%), while FF and V_{OC} each reduce by 2%. It is worth noting that the planar cell shown here was not optimized for off-normal illumination, and improved performance may be possible.

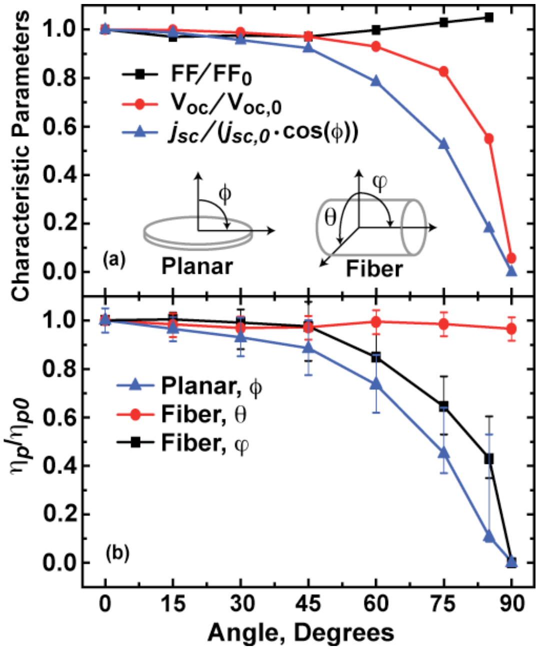

Figure 5.6. (a) Measured dependence of the planar cell's characteristic operating parameters (FF, V_{OC}, and j_{SC}) on illumination angle, normalized by performance under normal illumination (FF_0, $V_{OC,0}$ and $j_{SC,0}$). The inset illustrations define the relevant illumination angles for the planar and fiber cells. (b) Measured dependence of the planar and fiber cells' normalized efficiency of the planar and fiber based devices with variation in illumination angle. Note that $\eta_p(\phi)/\eta_{p,0}$ and j_{SC} for the planar cell and $\eta_p(\phi)/\eta_{p,0}$ for the fiber zenith angle are corrected for decreased illumination intensity with angle by cos(ϕ).

Together, the effects of shading and oblique incidence of light on a fiber-shaped cell are predicted to combine to make it 17% less efficient at normal incidence than the same cell on a planar substrate. However, the tested devices show an additional 17% loss. This discrepancy is dominated by the value of V_{OC}, with a drop beyond what is expected for the illumination geometry.

We believe that this additional reduction in V_{OC} is most likely due to the lowering of the Fermi energy (E_F) in CuPc deposited on the rotating fiber substrate. It has been shown that E_F for CuPc can vary with morphology (Grzadziel et al., 2003), and our preliminary results show V_{OC} drops concomitant with morphology variations for intermittently deposited organic layers. These results arise from tests in which deposited CuPc onto a Mg:Au film on a planar silicon substrate under the two scenarios shown in **Fig. 5.7(a)**. The first scenario is continuous CuPc deposition (as durng the deposition of a planar OPV cell), and the second scenario is intermittently CuPc deposition with a periodicity close to that used for the fiber rotation. These films show clear differences in morphology (see **Fig. 5.7(b)**). Further measurements showed that planar OPV cells fabricated with intermittent deposition of the organic layers exhibited a 16% lower V_{OC} than continuously-grown devices. Combining this V_{OC} drop caused by the deposition geometry with the predicted losses due to illumination geometry gives a rather accurate account of the performance of the fiber device. We note that the PV cell performance is also sensitive to variations in the thickness of the cathode deposited onto planar versus fiber devices, particularly when metal-organic-metal structures are employed (Peumans et al., 2003b; Zhang et al., 2004). The sensitivity with metal film thickness is from the large extinction coefficient of the material resulting in a large amount of light absorption with increasing film thickness.

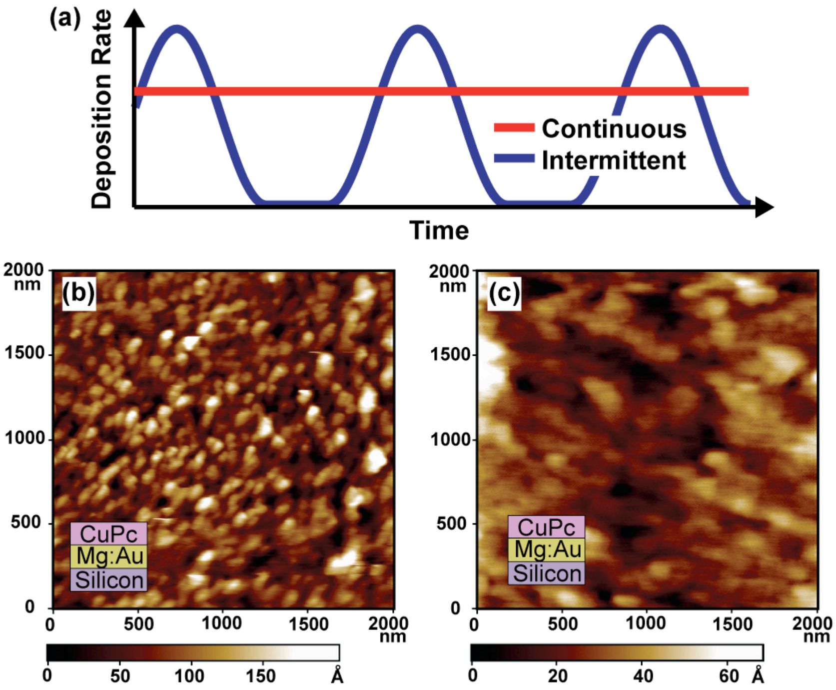

Figure 5.7. (a) Schematic of the deposition process seen for the planar cell (continuous deposition, and for a point on the fiber substrate while the fiber is axially rotating (intermittent deposition). (b) AFM morphology of a CuPc film deposited planar Mg:Au under continuous deposition. (c) AFM morphology for the same layer structure for a planar silicon substrate with CuPc deposited intermittently (mimicking the fiber deposition process).

Lastly, we consider the performance of individual cells formed along the fiber substrate, as shown in **Fig. 5.8**. None PV cells evenly spaced along a 33 mm length of fiber exhibit similar performance, suggesting that the active length of the fiber device is limited primarily by the geometric constraints of the deposition apparatus, and that longer fiber devices are practical with the development of reel-to-reel evaporation methods.

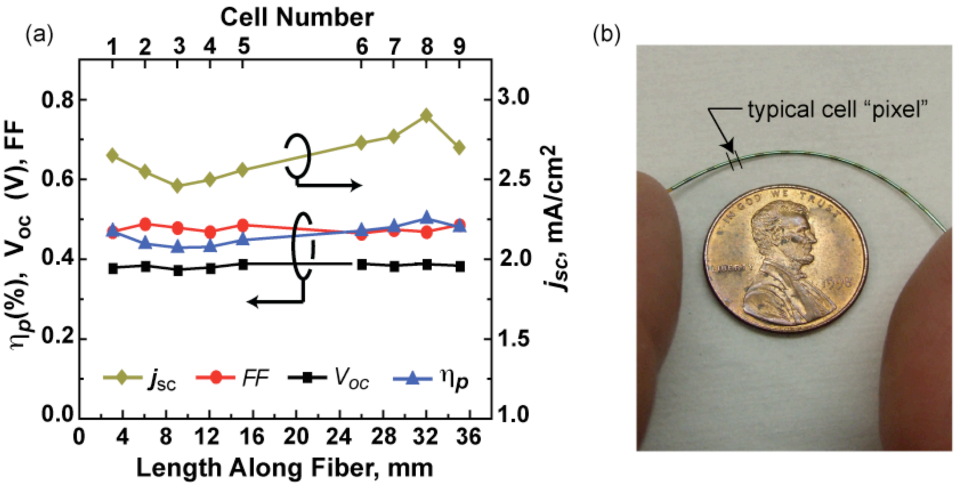

Figure 5.8. (a) A plot of several performance metrics for a fiber-based OPV cell, shown for each cell formed along the fiber length. The parameters considered include the power efficiency (η_p), open circuit voltage (V_{OC}), fill factor (*FF*), and the short-circuit current density (j_{SC}). The individual cells formed along the fiber perform comparably to each other, with the total fiber length limited only by the geometry of the deposition system. (b) Photograph of typical fiber with 1 mm "pixel" OPV cells deposited along its length.

5.4 Performance advantages of the fiber PV cell over its planar analogue

While the planar OPV cell outperforms the fiber device under normal incidence, consider the performance of the fiber PV cell shown in **Fig. 5.9(b)**. Due to the cylindrical symmetry of the fiber, η_p/η_{p0} does not vary with azimuthal illumination angle (θ). The fiber cell also shows a slower fall-off in η_p/η_{p0} with zenith angle (φ) than the planar cell, attributed to the already large proportion of off-normal incidence across the surface of the fiber. This much more gradual reduction in η_p/η_{p0} of the fiber cell is important for mobile applications, systems without sun-tracking, and diffuse light conditions. Under such conditions the device must operate over a wide range of illumination light angles. Here, we consider the power conversion efficiency of the devices illuminated from all angles within an encompassing hemisphere (η_{hemi}, i.e. angles subtended by a 2π solid angle), shown in **Fig. 5.9**. The width of the planar cell is taken to be equal to the diameter of the fiber cell.

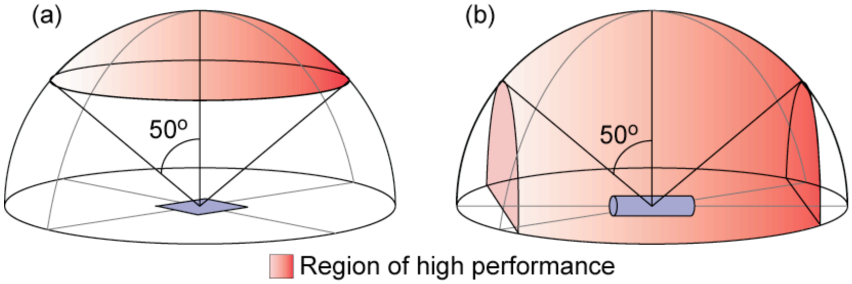

Figure 5.9. Schematic of an encompassing hemisphere for (a) a planar OPV and (b) a fiber-based OPV cell. The region of high performance is qualitatively defined as 50 degrees based on the efficiency roll-over data in **Fig. 5.6**. Due to the cylindrical symmetry of the fiber, the region of high performance is much greater for the fiber structure.

Using the experimentally measured variation in η_p with incident angle for the planar and fiber cells (**Fig. 5.6**), it is estimated that the fiber and planar cells have the same hemispherical efficiency, with $\eta_{hemi,f}$ = 0.48% for the fiber cell and $\eta_{hemi,p}$ = 0.48% for the planar cell. Note that $\eta_{hemi,f}$ was calculated using only the data for η_p under varying zenith angles, by transforming all locations on the encompassing hemisphere to zenith angle coordinates.

Note also that the parity in η_{hemi} between planar and fiber cells is achieved even with the deposition apparatus-dependent V_{OC}. For ideal conditions without the 16% loss in V_{OC} associated with the intermittent deposition (such as cells fabricated in an apparatus that deposits on all sides of the fiber at once), $\eta_{hemi,f}$ increases to 0.57%, outperforming the planar device.

Further advantages are seen when considering a hemispherical average of power generation (P_{hemi}). Taking the angle-dependent generated electrical power as $P(\phi) = \eta_p(\phi) \cdot I(\phi)$ where the intensity on the cell ($I(\phi)$) is reduced by $cos(\phi)$ for the illumination angle ϕ (replaced by φ for the fiber) , we see that $P_{hemi,p} = 0.3$ mW/cm^2 for the planar cell, while $P_{hemi,f} = 0.4$ mW/cm^2 for the fiber. Without the V_{OC} losses incurred due to intermittent deposition, $P_{hemi,f}$ is predicted to increase to 0.48 mW/cm^2, a 60% improvement over the planar cell. This enhancement would be reduced for bundled sets of fibers (discussed in **Chapter 6**), however it remains plausible that under generalized operating conditions, the fiber cell may indeed outperform its planar analogue. Furthermore, this highlights the important dependence of device performance on the deposition process.

5.5 Summary

This chapter focused on the experimental demonstration and detailed analysis of an OPV cell deposited on a fiber, which potentially constitutes a basic building block of textile-based solar cells. Detailed comparisons were made with planar OPV analogues. The performance of the fiber PV cell is much less dependent on variations in illumination angle than the planar metal-organic-metal OPV cell, enabling the fiber-based device to outperform its planar analogue under certain common operating conditions (e.g. diffuse illumination, no solar tracking, or mounting on a moving object such as an air vehicle). Individual PV devices collectively spanning 33 mm of the fiber substrate perform comparably, suggesting that the form factor and fabrication are scalable via reel-to-reel manufacturing methods, as discussed in **Chapter 8**. Similarly designed fiber-based organic light-emitting devices are shown to operate in **Fig. 7.1** under mild flexure, suggesting weaving of PV fiber devices may be practical. The unique fiber geometry also provides further opportunities for improving light trapping in PV cells, as will be discussed in **Chapter 6**. Significant additional gains can be realized with improved deposition methods and the further development of transparent electrode materials that can be deposited onto active organic layers.

CHAPTER 6

OPTICAL MANAGEMENT IN FIBER-BASED ORGANIC PHOTOVOLTAICS

6.1 Introduction and motivation

In the previous chapter, single-fiber OPV cells were demonstrated and studied in detail. Benefits were observed under certain operating conditions, yet experiments under normal (angle) illumination show the fiber cell to be 34% less efficient than its planar counterpart and 56% less efficient than an archetypal glass-ITO cell. This lower performance is attributed to the non-planar geometry of the fiber and the intermittent deposition of device layers. The discrepancy due to the deposition intermittency can be corrected with modifications to the deposition system, but the loss associated with the non-planar geometry is an inherent property of the fiber that results in increased reflection for off-normal incidence along the illuminated fiber surface, in addition to the (albeit small) losses due to the partial shading of side of the coated surface. However, optical losses due to reflection in individual fibers can be reclaimed by 2 compatible approaches: external optical coatings, and multi-fiber architectures that promote light trapping within individual fibers and fiber bundles.

In this chapter, the design of fiber OPV systems that result in efficient light trapping will be studied using the model developed in **Chapter 2**. First, the model will be used to predict the performance of a fiber device with external coatings. Then the model will be extended to consider multi-fiber systems in which certain bundle configurations result in large gains in light absorption and short-circuit current. Finally, “color-tuned” fiber-OPV cells will be considered in a bundled system where individual fibers will be designed to have very high quantum efficiency over small wavelength ranges and then combined in a bundled system to act as built-in light dispersion elements for off-resonant wavelengths leading to improved overall j_{SC}.

6.2 Modeling of fiber-shaped organic photovoltaic devices

To enable the design of high-efficiency fiber PV systems, we begin with the optoelectronic model described in **Chapter 2**. Although this model has already been used in previous chapters to accurately predict the performance of OPV devices under normal illumination, here we verify its ability to accurately predict the j_{SC} of a planar cell under a range of illumination angles and a fiber-OPV cell. The planar and fiber metal-organic-metal OPV cells demonstrated in the previous chapter are modeled with $L_{D,CuPc}$ = 11.5 nm and $L_{D,C60}$ = 20 nm, values similar to those used in **Chapter 3**. The device structure of this device is provided again in **Fig. 6.1**. As discussed in detail in **Chapter 2**, the diffusion lengths are used as fitting parameters to experimental data (staying within the range of literature values). The planar ME-OPV cell is predicted to have a j_{SC} = 3.29 mA/cm^2 under normal incidence, a 2.6% error from the experimental result. To model the fiber cell, we map the planar cell’s angle-dependent j_{SC} onto the fiber’s cylindrical geometry. As shown in **Fig. 6.1**, the model yields very good agreement with experimental data for the planar metal electrode OPV cell performance under varying illumination angles. Integrating the resulting $j_{SC}(\phi)$ and including a 6% loss associated with half of the fiber being shaded yields a predicted j_{SC} for the fiber of 2.87 mA/cm^2, which compares well with the experimental result of 2.72 mA/cm^2 (this value is extrapolated from **Table 5.1** for 100 mW/cm^2). Having shown that the model can predict the performance of a fiber cell, we will use it throughout the remainder of this chapter to predict modified fiber OPV systems.

In the next section, new fiber configurations will be introduced and optimized to result in a significantly improved predicted efficiency. Before looking at these systems, the refinement of our single fiber design to boost its efficiency is a prudent first step. Using the exciton diffusion lengths that fit the fiber OPV experimental data, an enhanced planar top-illuminated ME-OPV cell is designed with optical spacers added between the absorbing organic layers and the electrodes. Using our model to maximize this cell's performance, we arrive at a layer structure for the enhanced ME-OPV cell consisting of a polyimide substrate followed by 100 nm Ag, 30 nm TiO_x, 15 nm CuPc, 27.5 nm C_{60}, 30 nm BCP, and 10 nm Ag.(Kim et al., 2006) An analogous enhanced ITO-OPV device is also optimized using the above exciton diffusion lengths, resulting in a cell that consists of glass substrate followed by 150 nm ITO, 15 nm CuPc, 30 nm C60, 40 nm BCP, and 100 nm Ag. The new ITO-OPV cell has a predicted j_{SC} = 8.42 mA/cm^2, the enhanced planar metal electrode OPV cell has a predicted j_{SC} = 8.06 mA/cm^2, and the enhanced fiber OPV cell with the same metal electrode structure has a predicted j_{SC} = 7.22 mA/cm^2.

6.3 Multi-fiber system in a single row with external coatings

The device iteration sequence of previous chapters, in which the glass-ITO OPV cell was transitioned to a ME-OPV structure and then to the fiber geometry, results in consecutive decreases in j_{SC}, as shown schematically in **Figs. 6.2(a-c)**. In this section, external dielectric coatings that have been shown to benefit planar ME-OPV cells will be applied to the fiber device (**Fig. 6.2(d)**), and multiple fibers will be placed adjacent to each other as one might encounter in a woven structure (**Fig. 6.2(e)**). These modifications will be explored as a means for recouping efficiency losses caused by transitioning from a planar geometry to the fiber device geometry.

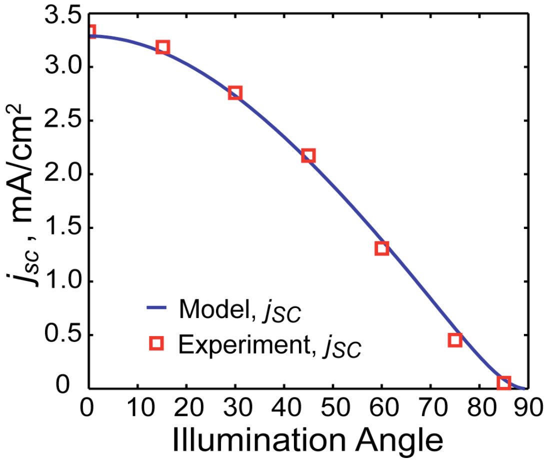

Figure 6.1. The variation of j_{SC} with illumination angle for a planar ME-OPV device with layer sequence of 5 nm Ag, 6.5 nm MgAg, 7 nm Alq_3, 40 nm C60, 25 nm CuPc, 65 Au, 45 MgAu on a polyimide substrate. The decrease in j_{SC} with angle follows a cosine pattern similar to the decrease in illumination intensity with angle incident on the OPV cell.

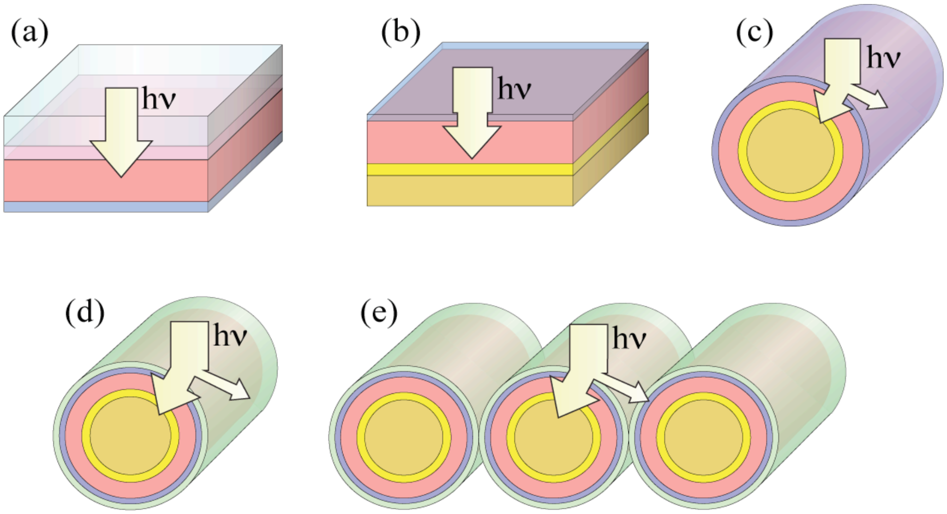

Figure 6.2. (a-b) A review of the devices considered in the previous chapters, leading to (c) the fiber OPV cell, along with design schemes to improve fiber OPV performance that include (d) and external coating to engineer optical transmission/reflection, and (e) a bundle of such fibers.

A six-layer dielectric coating for the fiber device is first designed according to the needle optimization technique of **Chapter 4**, with $\tilde{n}_H = 2.2$ and $\tilde{n}_L = 1.35$. Applying this coating to the fiber results in a predicted j_{SC} of 7.97 mA/cm^2 under normal illumination, a 10% gain over the basic fiber. If PV fibers are placed adjacent to each other, reflections off the sides of the fibers may be incident upon the neighboring fibers, trapping light very effectively for large off-normal angles of incidence along the fiber surface. Using ray tracing to account for the recycling of light (discussed below), adjacent fibers with optimized external coatings are predicted to have a $j_{SC} = 9.42$ mA/cm^2. This is a 31% increase over the individual uncoated fiber, and now is predicted to outperform the glass-ITO OPV cell. **Figure 6.3** shows the variation in reflectivity with illumination angle for the fiber including the cutoff angle beyond which reflected light is incident upon the adjacent fiber.

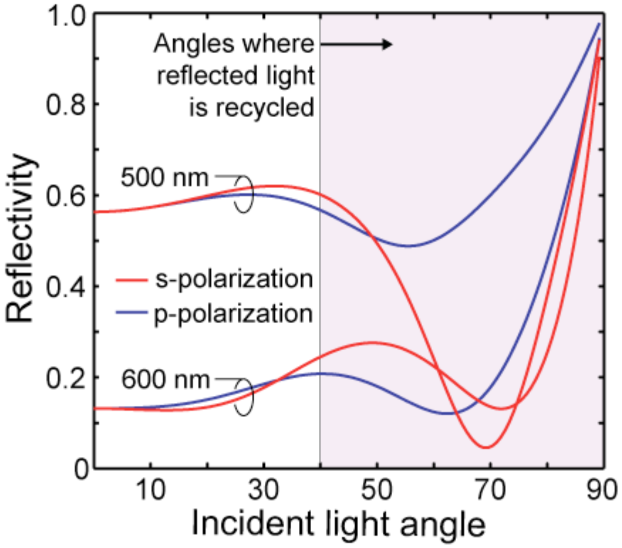

Figure 6.3. The dependence of the reflectivity on incident light angle for the optimized ME-OPV cell with a 6-layer optical coating for λ = 500 nm and λ = 600 nm incident light. For a single layer of adjacent fibers, incident light beyond 40 degrees will be reflected off the fiber OPV cell and incident upon an adjacent fiber.

6.4 Modeling multi-fiber OPV arrays that incorporate external coatings

To examine periodic multi-fiber systems with more than one layer, we utilize a program developed by Denis Nothern at the University of Michigan. As adapted for this work, the program generates an array of fibers, each having the optical properties of a given fiber-OPV cell. The user defines the location of each fiber within a repeating unit cell that has periodic boundary conditions. The fibers are approximated as infinitely long, which is an important consideration for off-normal illumination. A line emitter, defined above the fiber system, is a 2-dimensional line with light rays that emit perpendicular to the line with a given vector angle relative to the fiber bundle. A rear reflector (i.e. R = 1) is placed below the fiber bundle. A schematic view of a two-row fiber OPV bundle example is shown in **Fig. 6.4**. The figure shows a random sample of rays traced by the program for the two-row system. Note that rays incident on the left or right endge of the unit cell are translated to the opposite edge in order to satisfy the periodic boundary conditions. It is observed that the rays are incident upon all surfaces of each fiber, and thus reductions in performance due to shading of the fibers are neglected from this point forward. A flowchart of the ray tracing process is given in **Fig. 6.5**. The program runs until the summed intensity of the rays is less than 0.5% of the input intensity. For the line emitter, 10,000 rays are generated and randomly placed along the length of the emitter with even probability (Lopez-Hernandez et al., 2000).

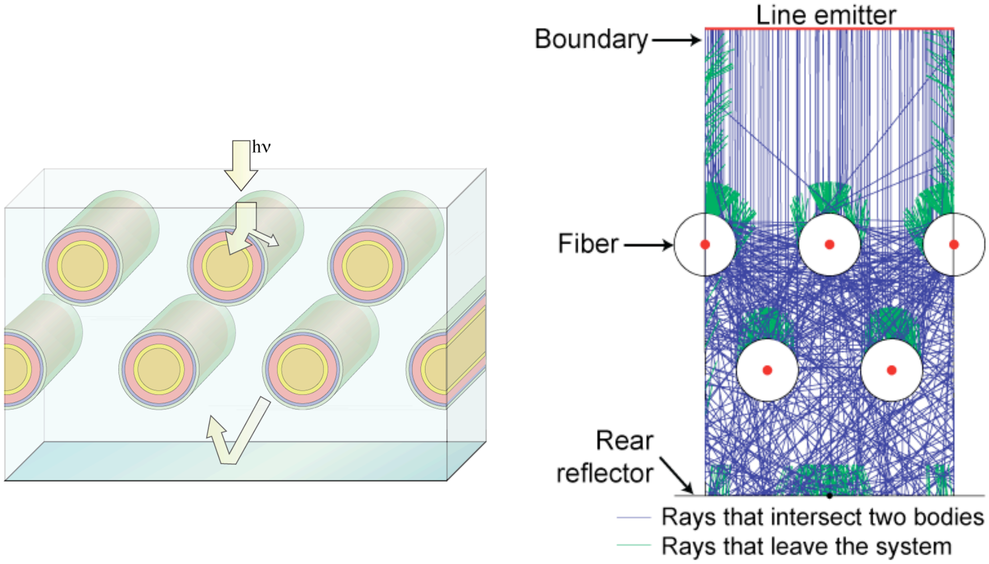

Figure 6.4. Illustration of the ray-tracing program that is used to analyze periodic multi-fiber OPV systems. Left, an illustration of a 2-row fiber bundle that is housed in a plastic matrix. Right, sample rays traced visually inspect the performance of a bundled fiber OPV system. Rays that leave the system are shown in green, and rays that are intersect at least two bodies are shown in blue.

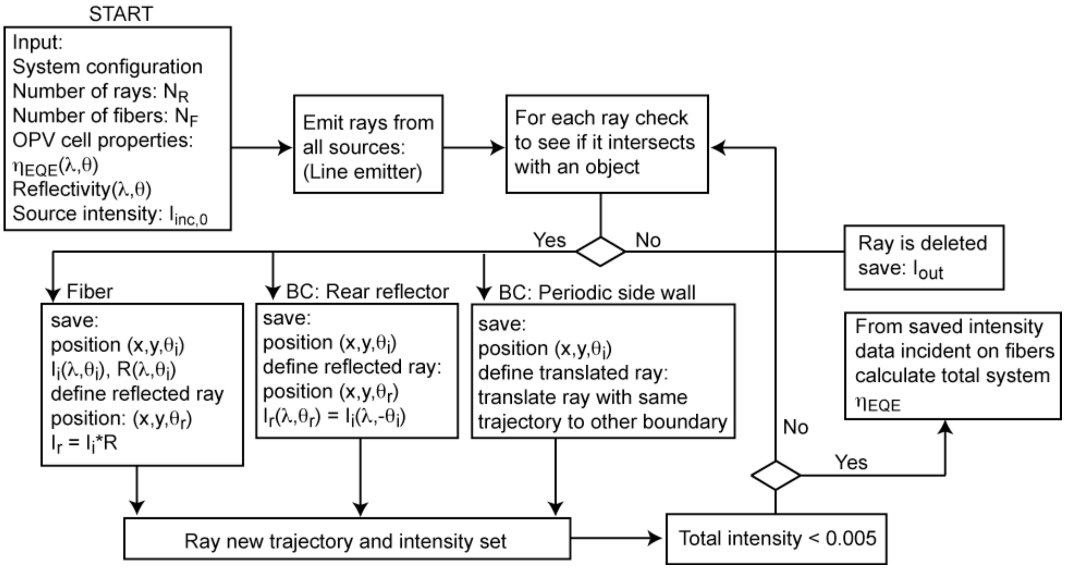

Figure 6.5. Flowchart of the ray-tracing program. The program begins after the unit cell is defined including properties of the line emitter, boundaries and fiber PV cells.

6.5 Multi-fiber OPV arrays: Design and performance

Even though a single row of fibers increases performance substantially (~18%), much of the light reflected off the fiber surface is not trapped efficiently. For properly designed multi-row fiber OPV bundles, however, a majority of light rays that enter the fiber matrix reflect many times before leaving the system. In this section, such fiber bundles are investigated as a means of efficiently trapping light in OPV cells and hence improving the absorption efficiency. The depth of fiber arrays is varied from 1 to 10 fiber rows, where for each number of rows, the distance between fibers is varied spatially both vertically and horizontally in a non-exhaustive search for the configuration with highest j_{SC}. The geometries of a few of the best-performing bundles are given in **Fig. 6.6**, with the performance given in **Fig. 6.7**.

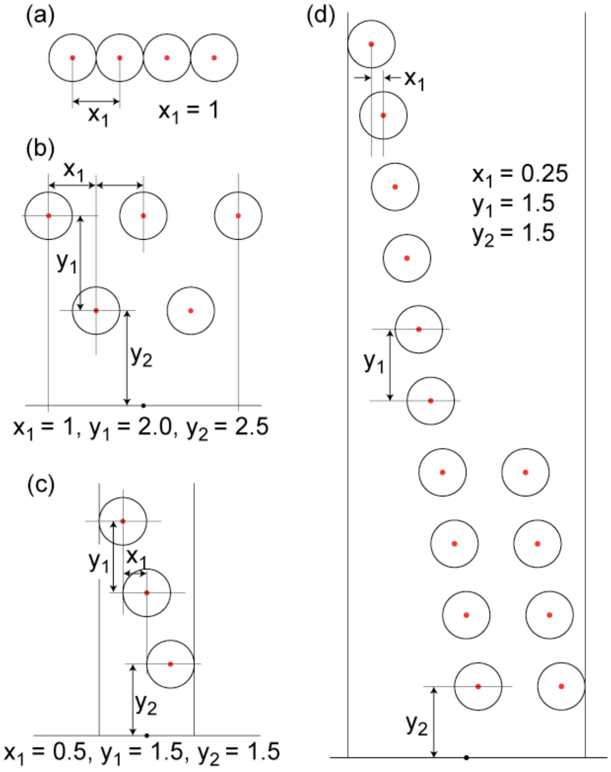

Figure 6.6. Coordinates for the best-performing fiber-OPV bundles for 2, 3, and 10-row systems. The coordinates are given in terms of fiber diameters.

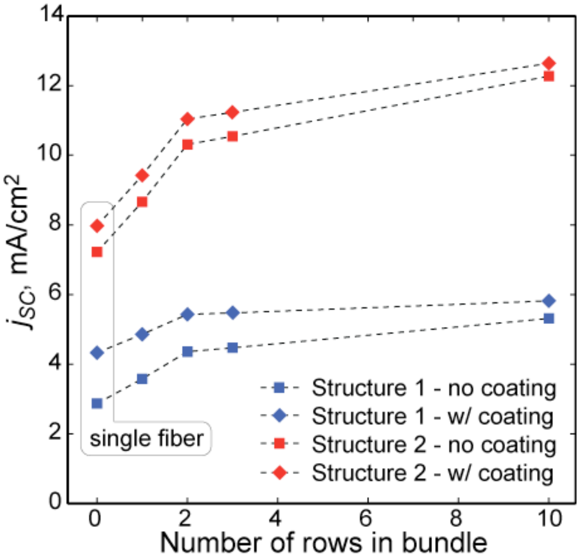

Figure 6.7. The predicted j_{SC} for multi-row fiber bundles. Fibers are shown with and without the application of an external coating that optimizes the j_{SC} of a single fiber. Structure 1 refers to the ME-OPV design used in **Chapter 5** and in this chapter to verify the optoelectronic model. Structure 2 refers to the enhanced device structure given in **Section 6.2**.

For the best 10-row fiber bundle system, combining the predicted j_{SC} of 12.64 mA/cm^2 with typical organic solar cell parameters of V_{OC} = 0.55 and FF = 0.6, the resulting bundle efficiency is predicted to be η_p = 4.16%. This is a 75% improvement over the single fiber cell and a 45% improvement over the glass-ITO device. Furthermore, note that the external coatings applied to the fibers are optimized based on the j_{SC} of a single fiber, not the j_{SC} of the entire bundle. Performing a needle optimization that is coupled to the ray-tracing simulation in order to optimize the coatings for maximum bundle j_{SC} may result in even higher bundle efficiency.

As might be expected, there are diminishing returns with increasing the number of rows. At ten rows, almost all light is absorbed by the system, and η_{EQE} approaches the modified internal quantum efficiency (η_{IQE}') as shown in **Fig. 6.8**. It is also important to consider the performance with illumination angle. The dependence of the performance on illumination angle is shown in **Fig. 6.9** for the best 2-row bundle. It is apparent that at low off-normal angles the bundles can outperform the glass-ITO cell, yet the overall trend in performance with angle is very similar to the conventional planar ITO-based OPV cells. This stems from the fact that scattering of light by the bundle is fairly invariant at low off-normal angles, but at high off-normal angles the light is not effectively transmitted to rows deep rows within the bundle, reducing the light trapping efficiency.

In the next section, we focus on the fact that η_{EQE} approaches η_{IQE}' in fiber OPV bundles. This phenomenon suggests new design for the fiber OPV device structures to improve overall bundle efficiency.

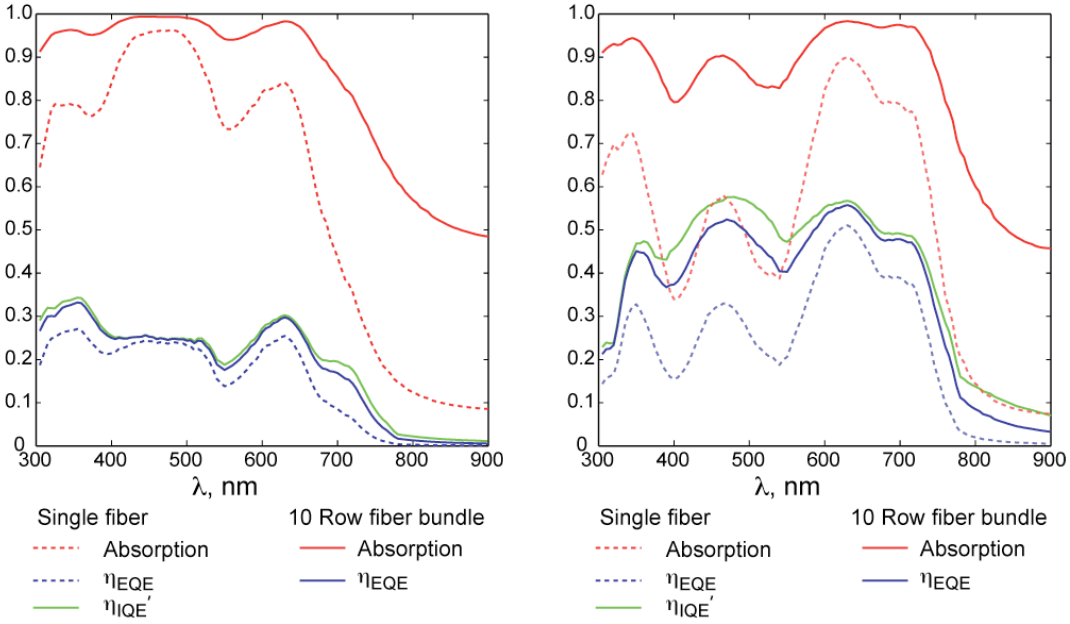

Figure 6.8. The η_{EQE}, η_{IQE}', and absorption of a single fiber, and for the 10-row fiber OPV bundle illustrated in **Fig. 6.6(d)**. The η_{IQE}' is the same for the single fiber and 10-row bundle. At left, the 10 row-bundle is for the fiber OPV cell design demonstrated in **Chapter 5**. At right, the 10-row bundle is for the enahnced fiber OPV cell design of **Section 6.2**.

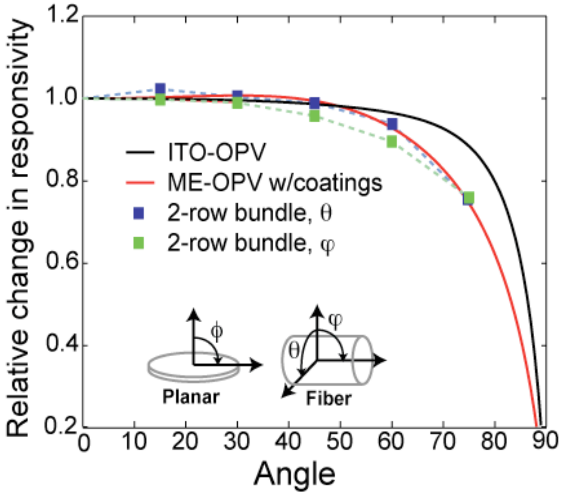

Figure. 6.9. The angular dependence of the planar-ITO and ME-OPV cells compared with a 2-row fiber bundle. The variation in the incident angle for the bundle is illustrated by the single fiber given in the inset. The relative responsivity is a measure of performance assuming the intensity on the surface of the cell is constant with angle.

6.5.1 Spectrally-tuned fiber OPV bundles

The optical microcavity formed by a metal-organic-metal OPV structure can be engineered to in-couple light very efficiently over a narrow resonant wavelength band and reflect light efficiently at other wavelengths. A group of spectrally tuned ME-OPV cells can therefore be designed to yield high quantum efficiency over a broad spectrum, if losses due to absorption of non-resonant wavelengths are minimized. Recently, narrow-band OPV cells coupled with an ideal optical dispersion element (which separates and routes wavelengths to the proper cells) were theoretically analyzed, showing potential for very high quantum efficiency (60 – 80%) over the solar spectrum (Kim, Kim, 2008); an illustration of this design in shown in **Fig. 6.10**. The study, assumed several idealizations including a perfect (i.e. lossless) optical dispersion element and an organic material with $\alpha = 1.5\times10^5$ cm^{-1} across the entire spectrum. Meeting these challenges is likely to prove quite difficult given the constraints of fabrication and readily available organic materials.

Building on this concept, a novel OPV system is introduced, consisting of a bundle that is composed of fiber-based OPV cells that are each spectrally tuned using optical microcavity engineering to achieve high η_{IQE}' over a narrow bandwidth with known materials. External coatings are applied to the fibers to further improve η_{EQE} for on-resonant wavelengths and maximize reflectivity for off-resonant wavelengths. This bundle design acts as an inherent dispersion element in which light of a particular wavelength bounces between the constituent fibers until it finds (and is absorbed by) a complementary tuned fiber OPV cell.

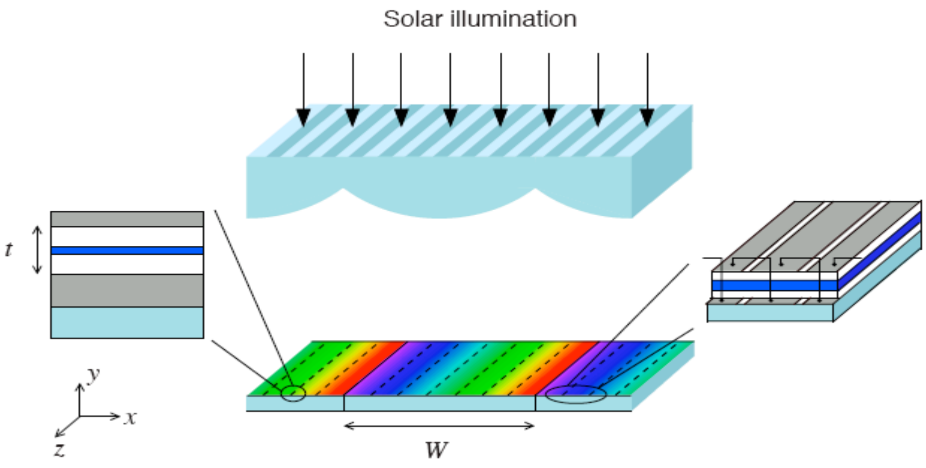

Figure 6.10. Schematic view of OPV cell in a lateral tandem configuration employing plnar microcavity sub-cells. The laterial tandem cell system consists of a one-dimension periodic array of a unit cell under an ideal dispersive-focusing element with period W. The dispersion element is conceptually represented by a lens with a grating on its surface that spectrally separates incoming solar photons and routes different wavelengths to the proper sub-cells. The planar microcavity OPV cell is shown at left with metal anode and cathode (gray), active organic layer (blue), and optical spacers (white) above and below the active layer. The electrical series connections between adjacent sub-cells are illustrated at right (Kim, Kim, 2008).

The microcavity tuned OPV cell consists of an active layer sandwiched by transparent and conductive transport layers followed by metal electrodes, the outermost of which is thin enough to be semitransparent. The basic structure of the OPV cell studied here is shown in the inset of **Fig. 6.11**. The electrodes are both silver, with the semitransparent electrode thickness set at 10 nm; this configuration was shown in **Chapter 3** to be highly conductive to optical engineering. To capture the widest range of the solar spectrum with known organic semiconductors, the chosen active layer materials are C60 (absorbs strongly for λ = 300-550 nm), CuPc (absorbs λ = 550 – 750 nm), and SnPc which has been shown to be effective in OPV cells and sensitive into the near infrared (absorbs λ = 700 – 950 nm) (Peumans et al., 2003b; El-Nahass, Yaghmour, 2008). The thickness of the active layer is set to be on the order of the materials diffusion length to maximize η_{IQE}; $L_{D,C60}$ = 24 nm, $L_{D,CuPc}$ = 9 nm, and $L_{D,SnPc}$ = 9 nm. The thickness of the transport layers adjacent to the active layer are defined to maximize η_{IQE}' over a specific optical band. **Figure 6.10** shows the maximum possible η_{IQE}' for a tuned microcavity OPV cell at each wavelength. For each material system, one specific device structure is chosen to maximize the combined response over the solar spectrum. The structure of the optimized C60-based OPV cell is: 100 nm Ag anode, 40 nm thick transport layers, and an active layer thickness of 15 nm. The CuPc-based OPV cell consists of 100 nm Ag, 75 nm transport layers, and 5 nm CuPc layer. The SnPc-based OPV cell has 100 nm Ag, 87.5 nm transport layers, and 7 nm SnPc layer. The refractive indices of each material are given in Appendix I. The refractive index of the transport layer is assumed to be equal to 1.75 across the entire visible spectrum.

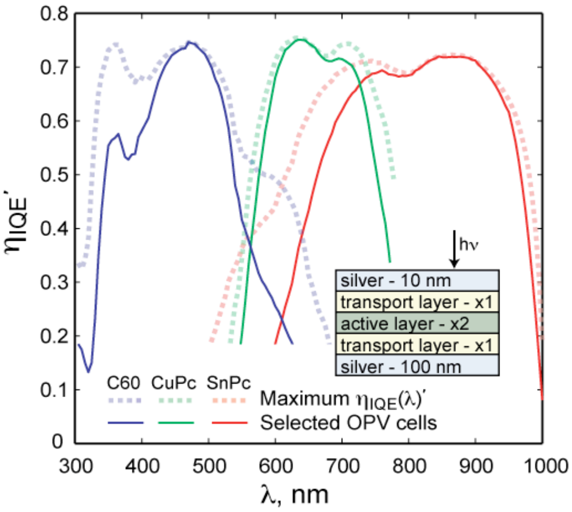

Figure 6.11. The maximum modified internal quantum efficiency (η_{IQE}') for microcavity-tuned OPV cells utilizing C60, CuPc, and SnPc at each wavelength. Here the OPV cell structure is optimized for each wavelength (i.e. every wavelength results in a unique OPV cell with unique transport layer thicknesses to maximize η_{IQE}'). The η_{IQE}' is also shown for devices with a selected transport layer thickness. The inset illustrates the microcavity OPV cell structure, where all three cells consist of a 10 nm semitransparent Ag electrode and a 100 nm Ag rear electrode. For the optimized C60-OPV cell, x_1 = 40 nm and x_2 = 15 nm; for the CuPc-OPV cell, x_1 = 75 nm and x_2 = 5 nm; and for the SnPc-OPV cell x_1 = 87.5 nm and x_2 = 7 nm.

For the fiber bundle to act as an effective dispersion element, each fiber should have high η_{EQE} for on-resonant wavelengths and high reflectivity for off-resonant wavelengths. In order to accomplish this, we first design the OPV cells to have a high on-resonance η_{IQE}' and then design multi-layer external dielectric coatings for each microcavity-tuned OPV cell. The design process follows the needle optimization outlined in **Chapter 3**, using the same refractive index values but with a merit function defined to maximize off-resonance reflectivity and on-resonance η_{EQE}. To restate, the merit function as defined in **Chapter 4** is:

$$(6.1) \qquad f(Q) = \left\{ \frac{1}{m} \sum_{j=1}^{m} \left[\frac{Q(\lambda_j, \phi_j) - \tilde{Q}_j}{\Delta Q_j} \right]^2 \right\}^{1/2}.$$

In this expression, Q_j and $Q(\lambda_j, \phi_j)$ represent the *j*th target and calculated quantity of interest, respectively, and ΔQ_j is the associated design tolerance, all for m quantities (Sullivan, Dobrowolski, 1996). The design criteria for each "color-tuned" OPV cell are given in **Table 6.1**. The η_{EQE} and reflectivity results of optimized 6-layer coatings are shown in **Fig. 6.12**.

Table 6.1. Needle optimization merit function parameters for the design of multi-layer dielectric coatings for the three fiber OPV sub-cells. For all three cells $\tilde{Q}_j = 1$, and m = 400, leading to a 5 nm increment in wavelength over the range of 300 - 1,000 nm.

PV cell type	λ = 300-550 nm	λ = 550-750 nm	λ = 750-1,000 nm
C60-tuned	$Q = \eta_{EQE}\ \ \Delta Q = 1$	$Q = R\ \ \Delta Q = 1/4$	$Q = R\ \ \Delta Q = 1/4$
CuPc-tuned	$Q = R\ \ \Delta Q = 1/4$	$Q = \eta_{EQE}\ \ \Delta Q = 2/3$	$Q = R\ \ \Delta Q = 1/4$
SnPc-tuned	$Q = R\ \ \Delta Q = 1$	$Q = R\ \ \Delta Q = 1$	$Q = \eta_{EQE}\ \ \Delta Q = 1/5$

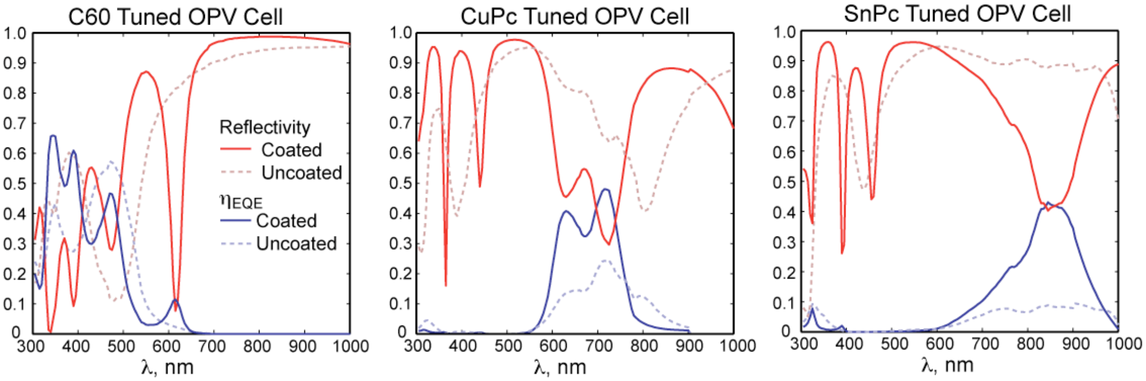

Figure 6.12. The external quantum efficiency (η_{EQE}) and reflectivity of the three "color-tuned" OPV cells under normal illumination. The performance of the OPV cells is considered with no external coatings and with a 6-layer dielectric coating stack.

As a first step en route to constructing a fiber bundle, we consider an array of planar microcavity-tuned OPV cells. These planar cells are arranged to ensure that rays reflecting off of one sub-cell are incident on another cell. The cells are also designed in such a way that incident light remains nearly perpendicular to the PV cell. An illustration of what such a system may look light is given in **Fig. 6.13(b)**. The calculated η_{EQE} for a system in which the light is incident upon the C60 cell, then the SnPc cell, then the CuPc cell is given in **Fig. 6.12(a)**, along with the η_{IQE}' for each tuned OPV cell. It is observed that in this system the η_{EQE} approaches the η_{IQE}' for each sub-cell, suggesting that OPV cells with optimized coatings have low parasitic absorption of off-resonant light. The idealized system with coatings is predicted to have j_{SC} = 18.62 mA/cm^2, while the system without external coatings is predicted to have j_{SC} = 11.42 mA/cm^2. This provides an upper limit as to what can be expected from a three sub-cell color-tuned fiber OPV bundle using the selected active materials.

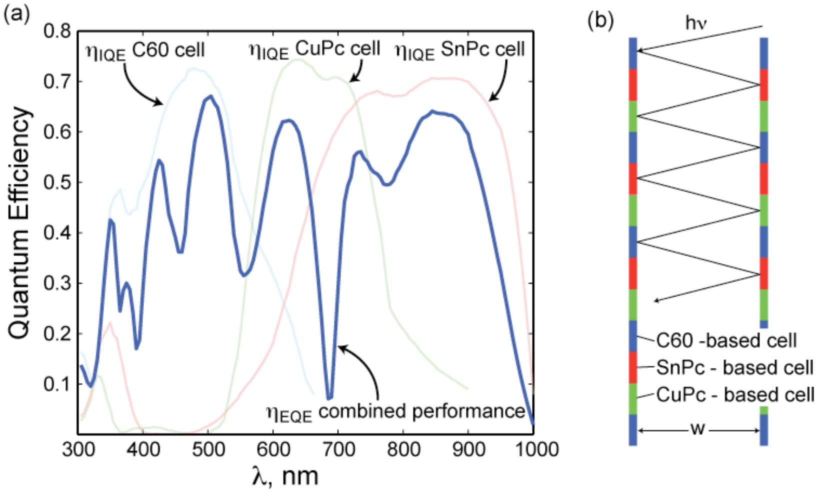

Figure 6.13. The idealized performance of a spectrally tuned OPV system with three sub-cel types. (a) The η_{EQE} of the idealized system in which non-reonant wavelengths of light are reflected from each cell to the others. The η_{IQE}' spectra of the three individual tuned OPV cells are shown for comparison. Reflections are considered until the intensity of light drops to less than 0.5% of its initial value. (b) Illustration of how the ideal system may be constructed, where the width (w) of the two panels approaches infinity so that the light nears perpindicular incidence with each sub cell (each cell must also then approach zero in length).

The three planar microcavity tuned OPV cells are now applied to the fiber geometry and placed into a bundled configuration. After a non-exhaustive search using ray-tracing, a high-performing 20-row bundled fiber system is designed as illustrated in **Fig. 6.14**. The resulting η_{EQE} for the bundled system along with the system absorption are also shown. This design results in a predicted j_{SC} = 13.96 mA/cm^2, surpassing the “single-color” fiber OPV bundle system and outperforming a single C60/CuPc fiber OPV cell by 93%. The system absorbs over 90% of the light from 300-1000 nm. We note that this design does not represent a global optimization. Improvements to color-tuned fiber OPV systems are likely with coupled design optimization of the coating design, design of the fiber bundle unit cell and fiber sub-cell locations. In addition, such an optimization should include the potential for each sub-cell to be optimized for the maximum output voltage, leading to improved overall power efficiency (Kim, Kim, 2008).

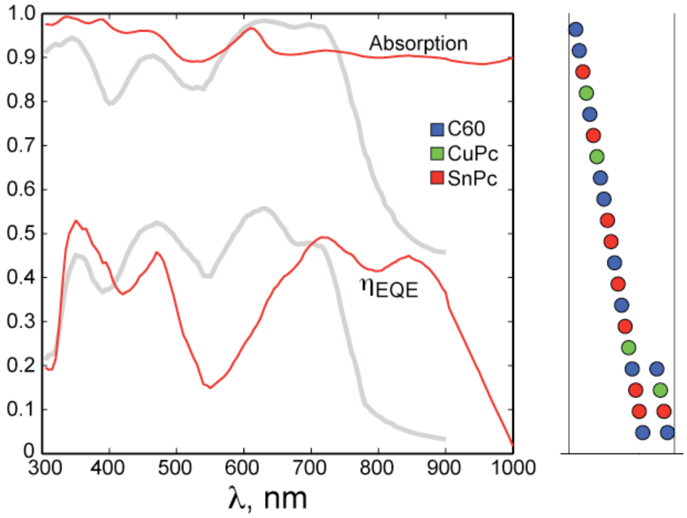

Figure 6.14. A color-tuned OPV bundle system with three sub-cell fibers. At right is the bundled structure with fiber colors indicating the cell type. At left are the η_{EQE} and absorption spectrum for the bundled system. The spectrally tuned system is compared to the device type 10-row bundle (**Fig. 6.8(b)**).

6.6 Concept feasibility and remaining work

To practically implement a multi-row fiber bundle, it is necessary to hold the fibers in place. This can be accomplished by placing the fibers in a transparent plastic matrix as illustrated in **Fig. 6.4**. This will change the optics at the air-plastic and plastic-fiber interfaces, but should not modify the overall efficiency substantially. In addition, bus-lines will be required to transport charge efficiently down long lengths of fiber. The bus-lines can be placed as metal strips underneath each fiber and may also act as light scattering sources in the ray-tracing program. In the model, the fiber bundles are observed to be somewhat insensitive to exact geometry, suggesting that the implementation of bus-lines will not substantially alter device performance.

Table 6.2 summarizes the performance of the different fiber configurations investigated in this chapter. It is observed that simply coating fibers and placing them adjacent to each other (as in a weave) provides substantial gains. For the color-tuned fiber OPV bundles, a more complete optimization is required that couples the number of tuned OPV cells, the external coating design, and the fiber bundle design together to maximize the power conversion efficiency.

The OPV device designs based on spatially distributed fibers offer several potentially powerful advantages over conventional planar devices. For example, electrical interconnections can be made with much greater latitude for current and voltage matching. This is in contrast to planar, series-connected tandem cells, for example, which suffer severe resistive losses for off-normal illumination and due to shifts in the illuminating spectrum in the course of the day. The spatially distributed fibers can be placed into an inert matrix material, which can prevent the diffusion of oxygen and moisture, and offer considerable protection from mechanical damage.

Table 6.2. Summary of the devices modeled in this chapter. The original device structures compare well with the experimental results from which the device layer thicknesses were enhanced. The fiber was designed with a 6-layer optimized coating. The coated fiber-OPV cell was then used in multi-fiber systems that were from one to ten rows deep. Finally, 3 color-tuned microcavity fiber OPV cells were placed in a twenty-row bundle. Efficiency estimates are based on V_{OC} = 0.55 and FF = 0.6, which are typical for OPV cells using these materials.

	j_{SC}, mA/cm^2	% improvement	η_p, %
Original device structures			
ITO - glass OPV	6.41	-	2.13
Metal electrode (ME) - OPV	3.29	-	1.09
Fiber - OPV	2.87	-	0.95
Enhanced structures			
ITO - glass OPV	8.42	-	2.78
ME - OPV	8.06	-	2.66
Fiber - OPV	7.22	From this value	2.38
Fiber system designs			
Single fiber with 6 layer-coating	7.97	10	2.63
One row of adjacent fibers	9.42	30	3.11
Two rows multi-fiber bundle	11.04	53	3.64
Three rows multi-fiber bundle	11.23	56	3.71
Ten rows multi-fiber bundle	12.64	75	4.17
Color-tuned multi-fiber PV			
Twenty rows, three sub-cell, multi-fiber bundle	13.96	93	4.61

CHAPTER 7

FIBER-SHAPED ORGANIC LIGHT-EMITTING DEVICE

7.1 Introduction and motivation

Advances in fiber and fabric technologies have been applied in a wide variety of contexts, including structural composites, fiber-optic communications, and more recently, electronic textiles. In the previous chapters, fiber-based organic photovoltaics devices have been studied in detail for applications in solar energy harvesting textiles and bundled composites. Fiber-based organic light-emitting devices (OLEDs) are also of interest for applications including fabric-integrated light sources and low-cost solid-state lighting. The fiber geometry provides an opportunity for low-cost red-green-blue (RGB) lighting by replacing integrated LED technologies that require expensive lithography techniques with separate RGB light sources in close proximity to one another. Additionally, it provides the ability to couple light from LEDs deposited onto an optical fiber into the fiber itself, with potential applications in optical communications and microscopy. However, there have been very few published scientific studies researching the impact that the fiber geometry has on device performance or the challenges facing fiber-based and fabric-integrated optoelectronics.

In this chapter we demonstrate a fiber-based OLED and analyze the physical effects that arise due to the non-planar device geometry, such as an electroluminescence spectrum that is independent of the observation angle. The experimental and theoretical treatment presented here focuses on organic materials as the active device layers, similar to the fiber-OPV device, taking advantage of their inherent mechanical flexibility and compatibility with low-cost device fabrication techniques (Forrest, 1997; Shtein et al., 2001). Furthermore, because the thickness of the active layers (~100 nm) is orders of magnitude smaller than the typical fiber diameter (~50 - 1,000 μm), light emission functionality can be integrated with the fiber substrate without significantly affecting its mechanical characteristics.

7.2 Fiber OLED fabrication

Red, green and blue fiber OLEDs are demonstrated in this chapter, with an emphasis on the performance of the green light-emitting device. The green-OLED employs an archetypal layer structure (Forrest, 1997), consisting of a metallic anode, organic charge transport and emission layers, and a semi-transparent metallic cathode, deposited sequentially and concentrically onto a 480 μm thick polyimide-coated silica fiber. The structure of the green-emitting fiber OLED is shown in **Fig. 7.1**. The fabrication method is very similar to the method used for the fiber OPV devices, where vacuum thermal evaporation is used to maintain fine control over the organic layer thicknesses and allow comparison with a planar device. This is necessary due to the fact that layer thickness variations as small as 1% of the ~100 nm total thickness strongly influence the electroluminescence (EL) of the device (Shtein et al., 2001).

Planar and fiber-based OLEDs were grown by vacuum thermal evaporation at 10^{-6} Torr. For both planar and fiber substrates the deposition sequence was: aluminum, nickel, CuPc, N,N'-di-1-naphthyl-N,N'-diphenyl-1,1'-biphenyl-4,4'diamine

(NPD), Alq_3, lithium fluoride (LiF), and aluminum. A shadow mask was used to deposit 1 mm length long cathode segments along the fiber and 1 mm diameter cathode disks for the planar cell, which define the device area. All layers were grown at rates of 0.2-0.3 nm/s, except for LiF and Ni, which were are grown at 0.02 nm/s. The nickel anode was oxidized prior to the deposition of the organic layers to facilitate hole injection (O'Connor et al., 2006; Kanno et al., 2005). The fiber substrate was axially rotated at a speed of 20 rpm during material deposition. The planar and fiber devices were cleaned with the same routine process of sonication with deionized water and organic solvents (Rhee, Lee, 2002).

Figure 7.1(c) shows a photograph of a 1 mm segment of an OLED deposited conformally around the fiber emitting characteristic green light under forward electrical bias. To study the effect of substrate geometry on optoelectronic performance, the same OLED structure was deposited on planar silicon and polyimide substrates, as depicted in **Fig. 7.1(a)**. The layer thicknesses on the fiber are corrected for the rotation of the substrate.

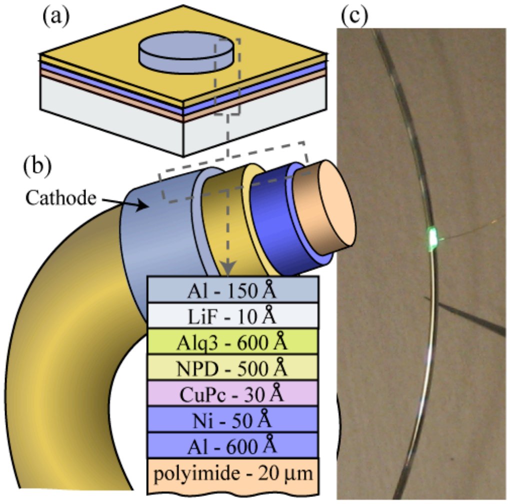

Figure 7.1. a) Illustrations of (a) planar and (b) fiber-based organic light emitting devices (OLEDs). c) A photograph of a flexed OLED fiber having a 1 mm green light emitting "pixel" turned on.

7.3 Device characterization

The current density-voltage (*j*-*V*) characteristics of two fiber OLEDs are compared to those of the analogous planar devices in **Fig. 7.2**. The silicon and polyimide planar substrate devices were grown simultaneously and characterized in close succession in atmosphere. The fiber devices were grown and tested separately due to the difference in the substrate geometry requiring different deposition processes. The line of sight deposition requires that the evaporation take into account fiber rotation where a portion of the fiber does not see adatoms at a given time. The similarity in the current-voltage relationship between the planar and fiber cells suggests comparable layer thicknesses of the hole and electron transport layers as designed (Baldo, Forrest, 2001). The slightly larger leakage current at low bias (< 2.5

V) in one of the fiber-based devices is attributed to a greater surface roughness on the fiber substrate.

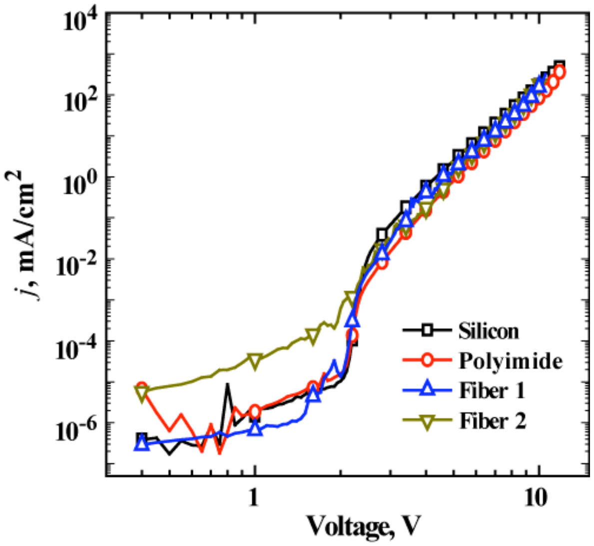

Figure 7.2. Current density-voltage characteristics of fiber and planar OLEDs. The planar OLEDs considered are on silicon and polyimide substrates. The similar behavior between devices suggests comparable organic layer thicknesses. One fiber device has increased leakage current attributed to substrate surface roughness causing an increased number of current shunt pathways.

While the electrical characteristics do not differ substantially between the fiber- and planar-shaped OLEDs, their emission characteristics are expected to differ substantially due to the microcavity effects typical of OLEDs. Specifically, the microcavity effects present in the planar device structure lead to a strong variation in the peak wavelength with emission angle (Bulovic et al., 1998; Worthing et al., 1999). **Figures 7.3(a)** and **7.3(b)** show the electroluminescence spectra of the planar devices on silicon and polyimide substrates for different observation angles. The peak of the emission is shifted by as much as 40 nm on moving from the normal to the in-plane observation angles. In contrast to the planar devices, as **Fig. 7.3(c)** and **7.3(d)** show, the fiber OLED exhibits an emission spectrum that is invariant with viewing direction. This can be understood by picturing the fiber OLED as an array of thin planar OLED strips of vanishing width around the circumference of a cylinder. Indeed, as **Fig. 7.4** shows, the full width half maximum (FWHM) of the EL peak is invariant with angle for the fiber OLED, but is larger than the FWHM for the planar OLEDs over the majority of observation angles.

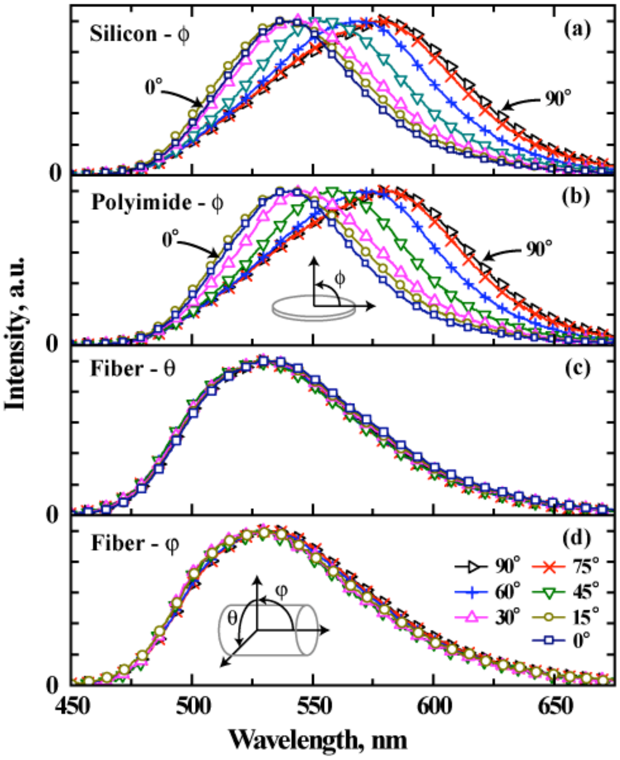

Figure 7.3. Emission spectrum with variation in observed angle for (a) planar top-emitting OLED on a silicon substrate, (b) a planar top-emitting OLED on a polyimide substrate, (c) a fiber OLED with variation in azimuthal angle θ, and (d) a fiber OLED with variation in zenith angle φ. Normal emission is taken as 90°; the inset schematics illustrate the directions of angular variation.

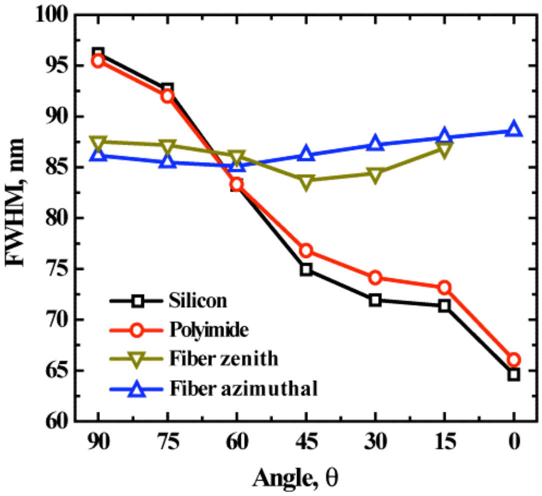

Figure 7.4. The spectral full width half maximum (FWHM) for the planar and fiber devices with variation in observtion angle defined for each device in **Fig. 7.3**. The planar OLEDs show similar and strong variation in FWHM, while the fiber devices show invariant angular behavior.

Figure 7.5 compares the experimental and predicted emission intensity versus angle (integrated over all wavelengths), where the model considers radiation from an isotropic distribution of oscillating dipoles confined within the device microcavity (Wasey, Barnes, 2000). The experiment and theory match well, with small deviations at off-normal emission angles attributed to increased scattering by surface imperfections. For comparison, a purely Lambertian emission pattern is also shown in **Fig. 7.5**. Based on measures light emission intensities from all sides of the fiber and planar devices, the external quantum efficiency (η_{EQE}) of each device is plotted versus current density in **Fig. 7.6** (Forrest et al., 2003). The efficiency of the "Fiber 1" device approaches that of the planar devices, with the difference attributed to small variations in the anode and cathode thicknesses and roughness, both of which can depend on the sticking coefficients of the adatoms, which in turn depends on the angle of arrival at the substrate.

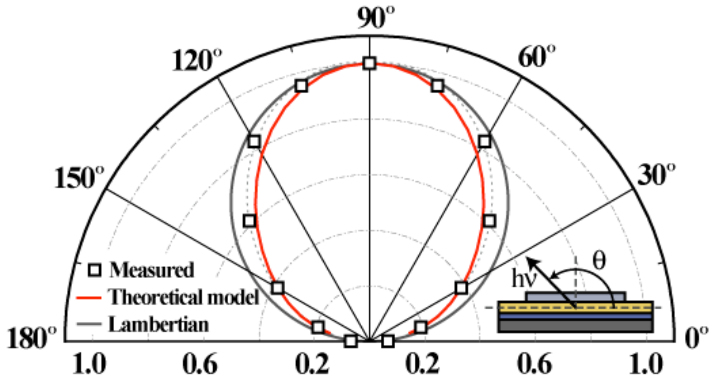

Figure 7.5. Electroluminescent intensity (integrated over all wavelengths) versus emission angle for a planar OLED with the device structure in **Fig. 7.1a**. The experimental data is compared with a theoretical model of the radiant power efficiency of an emitting dipole in the device microcavity and a Lambertian emission pattern.

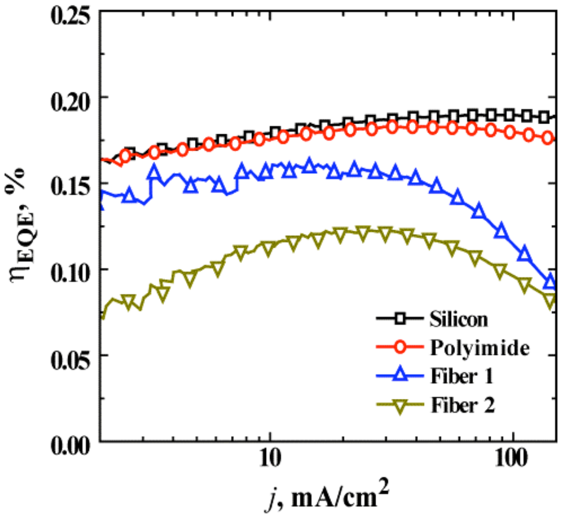

Figure 7.6. External quantum efficiency for the planar and fiber OLED devices. These efficiency measurements correspond to the *j*-v curves of **Fig. 7.2**.

7.4 RGB fiber OLEDs for solid state lighting

Organic light-emitting devices are reaching efficiencies that make them attractive for solid-state lighting (SSL) applications (Navigant Consulting Inc., 2009). A key challenge for commercial realization of this technology is a cost-effective device architecture. All solid-state white-light devices, both organic and inorganic, currently use one of two approaches to generate a broad, white-light spectrum, as illustrated in **Fig. 7.7.** The first approach is to have a short wavelength emitter that can be combined with a down-conversion phosphor to produce white light. However, there are inherent energy losses associated with the down conversion process. The second approach is to use separately biased red, green, and blue emitters that can be stacked on top of one another or placed adjacent to one another. This architecture is attractive in that it allows efficient emission of each color to combine as efficient white light. The difficulty with this approach is in the patterning requirements, which often require expensive lithography techniques that add considerable cost to the system. The fiber geometry provides an opportunity for low-cost RGB lighting by placing separately biased, efficient RGB fiber OLED sources in close proximity to one another without requiring expensive lithography techniques.

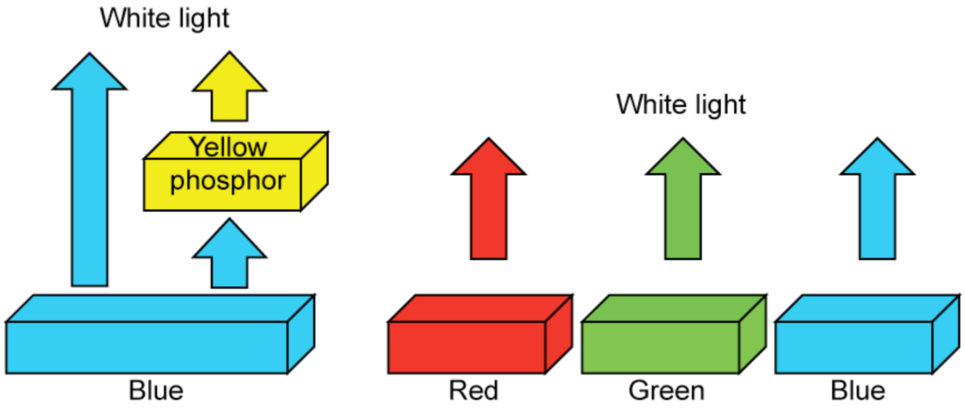

Figure. 7.7. Two approaches for generating white light from an OLED. At left, a blue light emitter is followed by partial down-conversion using fluorescent or phosphorescent layers. At right, separately biased red, green, and blue emitters are combined such that the close proximity generates white light in the far-field (Adapted from So et al., 2008).

Here we demonstrate the ability to fabricate separate red, green, and blue OLEDs on fibers that when combined can produce white light. The green-emitting device was discussed in detail in the previous section. The red and blue-emitting devices follow the same fabrication process, with modifications to the layer structure. The substrate and anode for all three devices are the same and consist of a 480 μm diameter polyimide-coated silica fiber substrate with 60 nm Al followed by 5 nm Ni. The Ni is UV-ozone treated after deposition to improve hole injection. The remainder of the layer structure for the red-emitting OLED is 3 nm CuPc, 30 nm NPD, 20 nm co-deposited Alq_3 and PtOEP (10:1 by volume), 20 nm Alq_3, 1 nm LiF, and 12 nm Al. An image of the red fiber OLED under forward bias along with its device structure is shown in **Fig. 7.8**. The blue OLED structure (after the anode) consists of 22.5 nm MTDATA, 30 nm NPD, 15 nm BCP, 10 nm Alq_3, 1 nm LiF, and 12 nm Al. The blue OLED structure with an image of the device under forward bias is also shown in **Fig. 7.8**. Based on the emission spectra of the devices, the color coordinates for each device are given in **Fig. 7.9**. The CIE 1931 chromaticity diagram (**Fig. 7.9**) represents a color space projection with an approximated RGB color gamut. Also on the plot is the Planckian locus, which represents the location of blackbody radiation at varying temperatures (the emission of the sun is closely approximated as a 6,000 K blackbody). The ability of the RGB fiber OLEDs to encompass much of the Planckian locus suggests that tuning the proportion of light from each OLED can be used to produce a range of colors including white light.

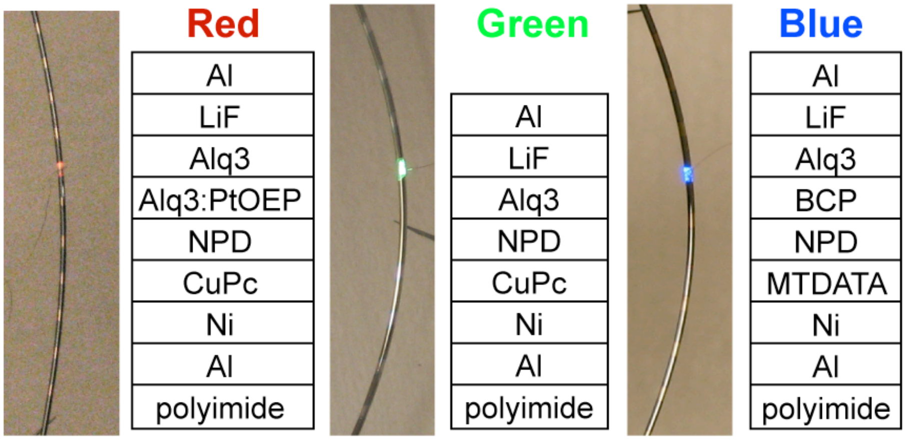

Figure. 7.8. Images of light emission from red, green, and blue fiber OLEDs under forward bias. At the right of each image is the corresponding device structure.

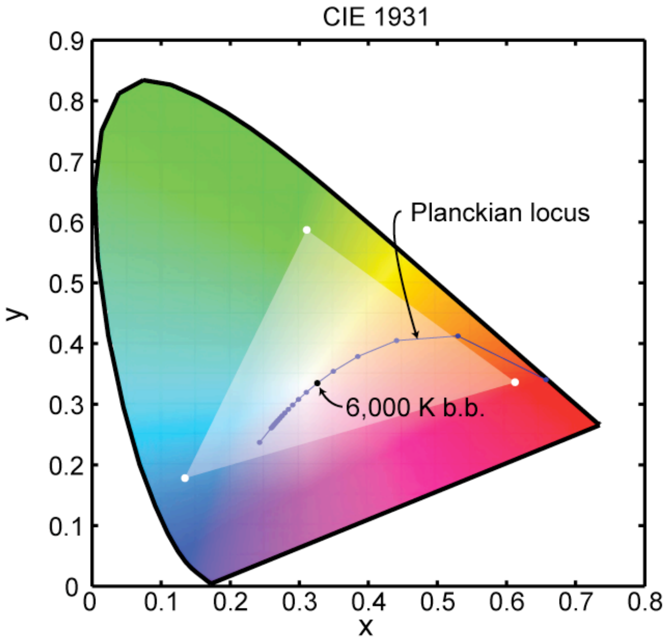

Figure 7.9. The CIE 1931 color coordinates for the fiber OLEDs demonstrated in **Fig. 7.8**. The three colors encompass much of the Planckian locus and thus have the ability to combine to generate white light. Also, shown is the color coordinate position for a 6,000 K black body that closely approximates the emission behavior of the Sun.

7.5 Conclusions and suggested future research on fiber-based OLEDs

The physical properties demonstrated above have the potential to be applied to a range of applications, yet for the fiber OLED to become commercially viable, long operating lifetimes are required. This may be achieved through proper device encapsulation. Developments are being made in monolithic encapsulation of flexible OLEDs with parylene (Yamashita et al., 2001; Ghosh et al., 2005) and multilayer coatings (Choi et al., 2007) such as Barix™ encapsulate (Burrows et al., 2001). These encapsulants are vacuum-deposited and thus directly compatible with the fiber geometry and fabrication technique discussed here.

In summary, there has been a considerable amount of research on OLEDs that focuses on the EL spectral behavior (Lu, Sturm, 2002; Riel et al., 2003; Cheung et al., 2004), including the microcavity effects that lead to variation in the emission spectrum with angle (Qiu et al., 2004; Neyts, 2005), and the use of non-planar device geometries to improve light out-coupling (Lupton et al., 2000). In this study, organic light-emitting devices having a fiber form factor were demonstrated and analyzed in detail. Fiber OLEDs exhibit optoelectronic performance characteristics comparable to those of planar analogues, but offer a novel device geometry with axially symmetric emission intensity and an emission spectrum that is invariant with observation angle; both traits are desirable for lighting applications. The electrical and optical characteristics of the fiber devices can be explained in terms of those of analogous planar device by adapting planar device models directly to the fiber geometry. The ability to form a light emitter directly on an optical fiber suggests further applications in fiber-optic communications and optical microscopy.

CHAPTER 8

SUMMARY AND SUGGESTIONS FOR FUTURE WORK

8.1 Summary of present work

Organic photovoltaic (OPV) cells and organic light emitting devices (OLEDs) have made great technological strides over the past 20 years, and are currently at different stages of commercial development. OLEDs are beginning to enter the marketplace in the form of displays, and are gaining interest for area lighting. Organic PV remains solely in the laboratory, although continued improvements in performance have moved the technology much closer to commercialization (Brabec, Durrant, 2008). The key challenges for these technologies include improving efficiency and operating lifetime as well as reducing manufactured cost. The objective of the work presented in **Chapters 1-7** has been to directly tackle efficiency and cost through experimentally and theoretically developed novel device architectures.

In **Chapter 3**, metal-organic-metal photovoltaic device structures were developed to obviate the need for undesirable (e.g. brittle and costly) ITO electrodes. Different metals were considered based on their optical and electronic properties, leading to the choice of Ag as optimal for the OPV cell under consideration. An OPV cell utilizing only a 9 nm thick Ag anode was demonstrated to have a power conversion efficiency equal to that of an OPV device using ITO. In addition, top-illuminated devices using semitransparent metal films were developed, increasing the potential for practical OPV cells on low-cost and opaque substrates.

In **Chapter 4**, external coatings were introduced that coherently trap light in OPV devices. The coherence length of sunlight (approximately 800 nm) is much greater than the OPV layer thicknesses, resulting in coherent light propagation through the device. The design of optimized anti-reflection coatings for OPV cells must therefore take into account optical interference within the OPV cell structure. To validate this assertion and demonstrate the ability to improve power conversion efficiency using external coatings, an experiment was devised and conducted in which the solar cell performance was measured under monochromatic illumination while a dielectric capping layer was grown on the device. The change in short-circuit current was measured and compared to predictions of optical transfer matrix simulations, showing good agreement and verifying the concept. Multi-layer coatings were then designed to optimize the OPV cell for broadband illumination. These coatings were shown to be particularly effective when applied to metal-organic-metal devices. An organic solar cell with a thin metal anode and external dielectric coating was predicted to be 20% more efficient than a cell with an ITO anode and its own optimized coating.

In **Chapter 5**, a fiber-based OPV cell was demonstrated and characterized in detail. It was shown that OPV cells maintain performance under large amounts of shading, implying that a PV fiber with half the device always shaded under direct sunlight or with additional shading in a weave configuration will not experience significantly reduced performance. Another key feature of the fiber PV cell is that its performance is far less sensitive to illumination angle than its planar counterpart. This is an important feature, considering the broad range of illumination angles that are encountered in many PV applications. For low-cost OPV systems aimed at integration with other devices and surfaces, solar tracking is essentially out of the question. Solar tracking issues aside, substantial diffuse illumination exists under most operating conditions, suggesting that the fiber-based OPV devices can maintain an edge over planar counterparts.

In **Chapter 6**, the fiber OPV cell was shown to be a versatile building block for multi-fiber systems (such as might occur in a woven textile) that trap light very effectively and show large gains in device conversion efficiency. These multi-fiber systems become especially efficient when optimized dielectric coatings are applied to the fiber OPV cells, as introduced in **Chapter 4**. Adjacent fibers with optimized coatings are shown to be 34% better than a single fiber and outperform the archetypal planar cell that uses ITO electrodes. This breakthrough design potentially enables cost-effective large-scale solar energy harvesting systems. More complex distributions of fibers are shown to result in over 90% light absorption over the region of the solar spectrum where the organic layers absorb, and are predicted to nearly double the performance of the analogous planar glass-ITO OPV device.

In **Chapter 7**, fiber OLEDs were demonstrated and characterized in detail. The emission spectrum was shown to be invariant with viewing angle, as opposed to the strong angular dependence observed for analogous planar OLEDs. Red, green, and blue emitting fibers were demonstrated that can generate white light when combined. Both of these important features are attractive for realizing cost-effective OLED-based solid-state lighting.

The highlights of this work include:

- A metal-organic-metal OPV structure shown to have efficiency comparable to a device using ITO (O'Connor et al., 2008a).
- The introduction of coherent light trapping in organic solar cells using external dielectric coatings (O'Connor et al., 2006).
- Multi-layer dielectric coatings that when applied to metal-organic-metal structures achieve predicted performance gains of roughly 14% over analogous ITO-OPV cells that are likewise integrated with their own optimized coatings (O’Connor et al., in preparation).
- Demonstration that fiber-based organic photovoltaic devices can outperform their planar counterparts under diffuse illumination conditions (O'Connor et al., 2008b).
- Modeling of fiber OPV bundle geometries that act efficiently trap light and show large predicted gains in short-circuit current, including a 100% improvement over the conventional glass-ITO device (O’Connor et al., in preparation).
- Introduction of color-tuned fiber OPV bundles that simultaneously introduce high quantum efficiency performance over a wide range of wavelengths and inherent light dispersion (O’Connor et al., in preparation).
- Demonstration of fiber-based OLEDs that have angle-independent emission (O'Connor et al., 2007).

8.2 Outlook and future work: Planar organic devices

A recent research thrust in the OLED, OPV, and inorganic PV research communities has been to find alternatives to ITO as a transparent electrode. In **Chapter 3** we showed that thin metal films can effectively replace ITO for small molecule OPV cells. Such electrodes may also work well for polymer-based OPV cells (e.g. utilizing the P3HT:PCBM blend). Our calculations show that an electrode material which exhibits low n and non-zero k would be ideal. A future research direction in developing structured electrodes that have optimal optical properties and maintain conductivity may lead to even greater device improvements. The ability of noble metal electrodes also raises the possibility of engineering surface plasmon-polariton (SPP) energy transfer between the electrode and organic layer (Reilly et al., 2008). Future work that optimizes this plasmon coupling along with the metal anode's optical transmittance and electrical conductivity may achieve further improvements in device efficiency.

We have shown that external dielectric coatings significantly improve OPV performance, in particular when applied to metal electrode devices. Future work in this area could include the experimental demonstration of multi-layer coatings for broadband performance enhancement. Of particular importance is the development of low-cost and ductile anti-reflection coatings that can simultaneously act as an encapsulation for top-illuminated devices.

8.3 Outlook and future work: Fiber-based electronics

As outlined in the introduction, there have been numerous recent developments in fiber devices including batteries, thermoelectric generators (Yadav et al., 2008), piezoelectrics, solar cells (Liu et al., 2007; O'Connor et al., 2008b), photodetectors (Bayindir et al., 2004), and OLEDs (O'Connor et al., 2007). However, for the practical implementation of fiber-based electronics, there remain several key challenges including scalable fabrication, encapsulation, electrical interconnection, and a detailed understanding of device performance under mechanical stress and strain.

The fiber-based devices in this work were fabricated in a batch process using vacuum thermal evaporation. To realize large-area textiles and composites, much longer lengths of fiber than those demonstrated here are required. Such devices could be fabricated by thermal evaporation and/or solution processing techniques in a reel-to-reel configuration; an example of such a system in the early stages of its construction and operation is shown in **Fig 8.1** (courtesy of Steven Morris, University of Michigan). When the system is fully assembled, long lengths of fiber will spool through multiple interconnected vacuum stages, each of which depositing electrodes, active organic layers, or encapsulants. Alternatively, a solution coating processes for photo-active polymers can also be employed. Such a system using a cylindrical dye is illustrated in **Fig. 8.2** (Panoliaskos et al., 1985; Lee et al., 2009).

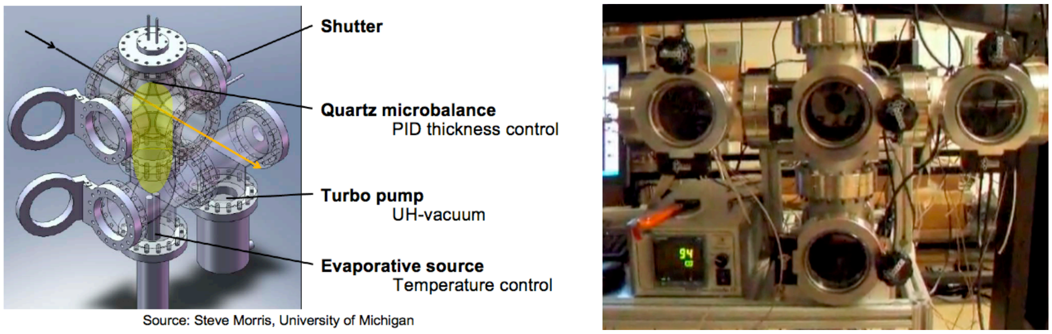

Source: Steve Morris, University of Michigan

Figure 8.1. Left, drawing of a single module of a reel-to-reel vacuum thermal evaporation system for fiber-based organic electronics. Right, an image of a current single module unit that is able to axially rotate and translate a fiber during thin film deposition (Courtesy of Steve Morris, University of Michigan).

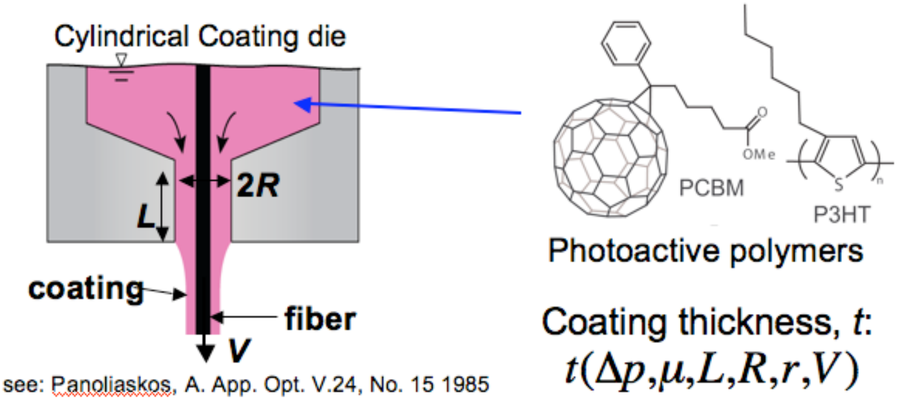

see: Panoliaskos, A. App. Opt. V.24, No. 15 1985

Figure 8.2. Left, illustration of a solution coating process for fiber-based organic electronics using photo-active polymers. Right, molecular structures of P3HT and PCBM, common polymer based photovoltaic materials.

Careful attention must be paid to fiber interconnections and module bus-lines in order to achieve efficient current extraction in fiber PV architectures. A woven PV textile, for example, represents a massively parallel system of PV fibers for which a robust electrical interconnection scheme has not yet been developed.

While the interior electrode does not produce electrical losses under most design situations, the transparency requirement for the outer electrode puts limits on its conductivity. This limitation necessitates bus-lines that are tied together with the outer electrode to efficiently collect generated current. An effective bus-line design that has been recently demonstrated involves wrapping a secondary metallic wire around the central OPV fiber (Lee et al., 2009). The amount of shading caused by the bus-line depends on the conductivity of the outer electrode and bus-line size, and optimal designs are required.

Finally, a major selling point of organic electronics is their compatibility with flexible substrates. Our replacement of brittle ITO electrodes by thin metal films aids device flexibility, yet little work has been done to analyze how the stress, strain, and fatigue associated with bending affect device performance. This is particularly important for fiber PV devices in textiles, which must withstand repeated flexing without performance degradation in order to be practical.

APPENDICES

I. Refractive indices and extinction coefficients of select materials

Refractive index: $\tilde{n} = n + ik$

References for the materials are provided below, below each table. Many of the refractive indices for metals and oxides are from E.F. Schubert, Rensselaer Polytechnic Institute (http://128.113.2.9/~schubert/) and references therein and repeated below.

Wavelength, nm	**ITO**		**Ag**		**Al**		**Au**	
	n	***k***	***n***	***k***	***n***	***k***	***n***	***k***
305	2.37	0.0505	1.45	0.8	0.407	4.43	1.82	1.92
310	2.34	0.044	1.323	0.647	0.407	4.43	1.83	1.916
315	2.32	0.04	1.044	0.514	0.407	4.43	1.835	1.91
320	2.3	0.03732	0.815	0.526	0.407	4.43	1.83	1.904
325	2.28	0.0337	0.526	0.65	0.407	4.43	1.825	1.878
330	2.26	0.0308	0.371	0.813	0.407	4.43	1.81	1.87
335	2.24	0.029	0.294	0.986	0.407	4.43	1.8	1.86
340	2.22	0.0267	0.259	1.12	0.407	4.43	1.785	1.852
345	2.21	0.025	0.238	1.24	0.407	4.43	1.77	1.846
350	2.2	0.0234	0.21	1.3	0.407	4.43	1.76	1.847
355	2.18	0.024	0.209	1.44	0.407	4.43	1.74	1.848
360	2.18	0.0211	0.19	1.48	0.407	4.43	1.72	1.855
365	2.17	0.02	0.186	1.61	0.407	4.43	1.716	1.862
370	2.16	0.0194	0.19	1.62	0.41	4.5	1.71	1.88
375	2.15	0.0188	0.2	1.67	0.432	4.56	1.7	1.906
380	2.14	0.0181	0.195	1.7	0.44	4.6	1.69	1.915
385	2.13	0.0176	0.193	1.81	0.46	4.6	1.68	1.923
390	2.12	0.017	0.192	1.81	0.46	4.71	1.674	1.93
395	2.1	0.0166	0.173	1.9	0.49	4.75	1.67	1.942
400	2.1	0.0161	0.172	1.95	0.5	4.86	1.66	1.956
405	2.1	0.0157	0.173	2	0.5	4.9	1.65	1.957
410	2.1	0.0154	0.173	2	0.523	4.9	1.64	1.958
415	2.1	0.0151	0.173	2.11	0.523	5.02	1.64	1.955
420	2.1	0.0149	0.17	2.2	0.54	5.1	1.63	1.95
425	2.1	0.014	0.162	2.23	0.55	5.1	1.63	1.945
430	2.1	0.0144	0.16	2.28	0.558	5.2	1.62	1.94
435	2.1	0.0142	0.158	2.35	0.57	5.3	1.6	1.92
440	2.05	0.0141	0.157	2.4	0.598	5.38	1.57	1.904
445	2.05	0.0139	0.157	2.45	0.6	5.38	1.54	1.89
450	2.05	0.0138	0.1513	2.47	0.6	5.3	1.5	1.87
455	2.05	0.0136	0.148	2.52	0.62	5.3	1.45	1.86
460	2.05	0.0135	0.144	2.56	0.644	5.28	1.43	1.846
465	2.05	0.0136	0.144	2.59	0.65	5.3	1.35	1.83
470	2.05	0.0135	0.133	2.7	0.66	5.5	1.28	1.81

475	2	0.0135	0.132	2.72	0.695	5.8	1.24	1.8
480	2	0.01344	0.13	2.75	0.7	6	1.15	1.81
485	2	0.0134	0.13	2.75	0.72	6	1.07	1.82
490	2	0.01344	0.13	2.8	0.74	6	1	1.83
495	2	0.0135	0.13	2.88	0.755	6.03	0.916	1.84
500	2	0.0135	0.13	2.9	0.78	6.1	0.85	1.88
505	2	0.0135	0.13	3	0.79	6.1	0.75	1.93
510	2	0.0135	0.13	3.01	0.8	6.1	0.7	1.99
515	2	0.0136	0.13	3.07	0.826	6.28	0.608	2.12
520	2	0.0137	0.13	3.1	0.83	6.3	0.54	2.25
525	2	0.0138	0.13	3.14	0.85	6.3	0.5	2.35
530	2	0.0139	0.13	3.2	0.9	6.3	0.47	2.42
535	2	0.0139	0.13	3.21	0.9	6.4	0.43	2.48
540	2	0.0141	0.129	3.25	0.912	6.55	0.402	2.54
545	2	0.0141	0.128	3.3	0.95	6.6	0.38	2.62
550	2	0.0141	0.125	3.34	1	6.7	0.36	2.7
555	2	0.0144	0.123	3.38	1	6.8	0.34	2.78
560	1.95	0.0145	0.12	3.45	1.02	6.85	0.32	2.84
565	1.95	0.0147	0.12	3.47	1.02	6.9	0.3	2.88
570	1.95	0.0149	0.12	3.5	1.055	7	0.28	2.89
575	1.95	0.015	0.12	3.54	1.1	7	0.26	2.9
580	1.95	0.0152	0.121	3.6	1.1	7.02	0.25	2.92
585	1.95	0.0154	0.121	3.61	1.1	7.1	0.24	2.93
590	1.95	0.0155	0.121	3.66	1.15	7.15	0.23	2.95
595	1.95	0.0157	0.121	3.68	1.15	7.2	0.22	2.96
600	1.95	0.016	0.122	3.73	1.18	7.2	0.21	2.97
605	1.94	0.0162	0.122	3.75	1.2	7.3	0.2	2.99
610	1.93	0.0166	0.125	3.8	1.25	7.4	0.2	3
615	1.92	0.0166	0.126	3.85	1.29	7.4	0.19	3.01
620	1.92	0.0168	0.13	3.88	1.3	7.48	0.19	3.03
625	1.92	0.017	0.132	3.9	1.34	7.5	0.18	3.05
630	1.9	0.017	0.133	3.95	1.38	7.6	0.18	3.08
635	1.9	0.018	0.133	4	1.4	7.6	0.17	3.1
640	1.9	0.018	0.134	4.03	1.43	7.7	0.17	3.12
645	1.9	0.018	0.136	4.1	1.48	7.8	0.165	3.14
650	1.9	0.0184	0.14	4.13	1.49	7.82	0.166	3.15
655	1.89	0.0186	0.14	4.18	1.51	7.85	0.165	3.2
660	1.89	0.0189	0.14	4.2	1.52	7.9	0.165	3.3
665	1.89	0.0193	0.14	4.23	1.55	7.9	0.164	3.4
670	1.89	0.0194	0.14	4.25	1.59	7.9	0.163	3.5
675	1.89	0.0198	0.14	4.26	1.6	8	0.163	3.6
680	1.88	0.02	0.14	4.29	1.65	8	0.162	3.7
685	1.88	0.0205	0.14	4.3	1.7	8.1	0.161	3.75
690	1.86	0.021	0.14	4.44	1.74	8.21	0.16	3.8
695	1.86	0.0211	0.141	4.486	1.74	8.25	0.161	3.85
700	1.85	0.022	0.142	4.52	1.8	8.3	0.161	3.9
705	1.85	0.022	0.143	4.56	1.8	8.3	0.162	4
710	1.85	0.022	0.144	4.6	1.9	8.4	0.162	4.1
715	1.85	0.022	0.145	4.6	2	8.45	0.163	4.15
720	1.85	0.023	0.148	4.6	2.1	8.5	0.163	4.2
725	1.85	0.023	0.148	4.7	2.1	8.5	0.164	4.28
730	1.83	0.023	0.145	4.74	2.14	8.57	0.164	4.35
735	1.83	0.024	0.145	4.8	2.2	8.6	0.165	4.4
740	1.83	0.024	0.145	4.8	2.2	8.6	0.166	4.45
745	1.83	0.025	0.145	4.9	2.3	8.6	0.167	4.5
750	1.8	0.025	0.146	4.9	2.3	8.6	0.168	4.6
755	1.8	0.026	0.145	4.94	2.4	8.6	0.169	4.65
760	1.8	0.026	0.144	5	2.4	8.6	0.17	4.7
765	1.8	0.026	0.144	5	2.5	8.6	0.1715	4.75
770	1.8	0.027	0.144	5	2.5	8.6	0.173	4.8
775	1.8	0.027	0.143	5.09	2.63	8.6	0.174	4.86

780	1.79	0.028	0.143	5.1	2.6	8.55	0.175	4.9
785	1.78	0.029	0.144	5.1	2.6	8.5	0.176	4.95
790	1.78	0.029	0.144	5.2	2.65	8.45	0.177	5
795	1.78	0.03	0.144	5.25	2.65	8.45	0.179	5.05
800	1.77	0.03	0.144	5.3	2.65	8.4	0.18	5.1
805	1.77	0.03	0.144	5.3	2.7	8.4	0.181	5.15
810	1.75	0.031	0.144	5.4	2.7	8.35	0.183	5.2
815	1.75	0.031	0.144	5.4	2.7	8.35	0.185	5.25
820	1.75	0.032	0.144	5.4	2.74	8.33	0.186	5.3
825	1.75	0.032	0.145	5.5	2.74	8.31	0.188	5.39
830	1.75	0.033	0.146	5.53	2.7	8.3	0.189	5.45
835	1.74	0.033	0.1476	5.564	2.7	8.3	0.19	5.5
840	1.74	0.034	0.149	5.6	2.7	8.3	0.192	5.53
845	1.74	0.035	0.15	5.64	2.6	8.25	0.194	5.58
850	1.74	0.036	0.152	5.68	2.5	8.25	0.195	5.62
855	1.72	0.036	0.154	5.72	2.5	8.25	0.196	5.66
860	1.72	0.037	0.155	5.75	2.4	8.25	0.197	5.67
865	1.72	0.037	0.1567	5.8	2.4	8.24	0.198	5.72
870	1.7	0.038	0.158	5.83	2.3	8.22	0.199	5.75
875	1.7	0.039	0.16	5.87	2.3	8.21	0.2	5.79
880	1.7	0.04	0.161	5.91	2.25	8.21	0.205	5.82
885	1.7	0.04	0.163	5.95	2.24	8.21	0.21	5.88
890	1.7	0.041	0.165	5.98	2.24	8.2	0.215	5.92
895	1.7	0.042	0.168	6.02	2.24	8.2	0.22	5.96
900	1.7	0.044	0.17	6.06	2.24	8.2	0.225	6

References:

ITO – Filmetrics Corporation of San Diego, California 2002

Ag – Palik E. Handbook of Optical Constant of Solids, 1985

Al – Filmetrics Corporation of San Diego, California 2002

Au – Filmetrics Corporation of San Diego, California 2002

Wavelength, nm	**Mg**		**Ni**		**PEDOT:PSS**	
	n	***k***	***n***	***k***	***n***	***k***
305	0.1315	2.63	1.73	2.0	1.45	0.019
310	0.1334	2.675	1.73	1.98	1.447	0.0193
315	0.1353	2.72	1.72	1.98	1.444	0.0196
320	0.1372	2.765	1.7	1.98	1.441	0.02
325	0.1392	2.81	1.69	1.99	1.438	0.0203
330	0.1412	2.855	1.68	1.99	1.435	0.0206
335	0.1433	2.9	1.66	2.02	1.432	0.02095
340	0.1454	2.945	1.65	2.03	1.429	0.02128
345	0.1476	2.99	1.64	2.07	1.426	0.02161
350	0.1498	3.035	1.64	2.1	1.423	0.02194
355	0.1521	3.08	1.63	2.1	1.42	0.02227
360	0.1544	3.125	1.63	2.14	1.418	0.0226
365	0.1568	3.17	1.62	2.17	1.416	0.02293
370	0.1593	3.215	1.62	2.2	1.414	0.02326
375	0.1617	3.26	1.61	2.23	1.412	0.02359
380	0.1643	3.305	1.61	2.25	1.41	0.02392
385	0.1669	3.35	1.61	2.26	1.408	0.02425
390	0.1696	3.395	1.61	2.3	1.406	0.02458
395	0.1723	3.44	1.61	2.33	1.404	0.02491
400	0.1751	3.485	1.61	2.36	1.402	0.02524
405	0.1780	3.53	1.61	2.39	1.4	0.02557
410	0.1809	3.575	1.61	2.4	1.399	0.0259
415	0.1839	3.66	1.61	2.44	1.398	0.02623

420	0.1869	3.71	1.61	2.48	1.397	0.02656
425	0.1901	3.76	1.61	2.5	1.396	0.02689
430	0.1933	3.81	1.61	2.52	1.395	0.02722
435	0.1966	3.86	1.61	2.57	1.394	0.02755
440	0.1999	3.91	1.62	2.61	1.393	0.02788
445	0.2033	3.96	1.62	2.63	1.392	0.02821
450	0.2068	4.01	1.62	2.64	1.391	0.02854
455	0.2104	4.06	1.63	2.65	1.39	0.02887
460	0.2141	4.11	1.64	2.71	1.389	0.0292
465	0.2178	4.16	1.64	2.75	1.388	0.02953
470	0.2217	4.21	1.65	2.77	1.387	0.02986
475	0.2256	4.26	1.65	2.81	1.386	0.03019
480	0.2296	4.31	1.65	2.83	1.385	0.03052
485	0.2337	4.36	1.66	2.85	1.384	0.03085
490	0.2378	4.41	1.66	2.9	1.383	0.03118
495	0.2421	4.46	1.67	2.93	1.382	0.03151
500	0.2465	4.51	1.68	2.95	1.381	0.03184
505	0.2509	4.56	1.69	2.97	1.3805	0.0325
510	0.2555	4.61	1.7	2.99	1.38	0.033
515	0.2601	4.66	1.71	3.06	1.3795	0.0335
520	0.2648	4.71	1.71	3.08	1.379	0.034
525	0.2697	4.76	1.71	3.12	1.3785	0.0345
530	0.2746	4.81	1.72	3.14	1.378	0.0352
535	0.2796	4.86	1.74	3.19	1.3775	0.0359
540	0.2847	4.91	1.75	3.19	1.377	0.0366
545	0.2900	4.96	1.76	3.2	1.3765	0.0373
550	0.2953	5.01	1.78	3.22	1.376	0.038
555	0.3008	5.06	1.8	3.3	1.3755	0.039
560	0.3063	5.11	1.8	3.33	1.375	0.0395
565	0.3120	5.16	1.81	3.33	1.3745	0.0405
570	0.3178	5.21	1.82	3.36	1.374	0.0416
575	0.3236	5.26	1.83	3.4	1.3735	0.0427
580	0.3296	5.31	1.84	3.4	1.373	0.0438
585	0.3358	5.36	1.84	3.4	1.3725	0.0449
590	0.3420	5.41	1.85	3.48	1.372	0.0463
595	0.3483	5.46	1.85	3.5	1.3715	0.0481
600	0.3548	5.51	1.86	3.52	1.371	0.0497
605	0.3614	5.56	1.86	3.53	1.3705	0.0513
610	0.3681	5.61	1.87	3.55	1.37	0.0529
615	0.3749	5.66	1.89	3.6	1.37	0.0545
620	0.3819	5.74	1.92	3.65	1.37	0.0561
625	0.3890	5.795	1.92	3.66	1.37	0.0577
630	0.3962	5.85	1.93	3.68	1.37	0.0593
635	0.4035	5.905	1.96	3.7	1.37	0.0609
640	0.4110	5.96	1.97	3.72	1.37	0.0625
645	0.4185	6.015	2	3.74	1.37	0.0641
650	0.4263	6.07	2.02	3.82	1.37	0.0657
655	0.4341	6.125	2.04	3.85	1.37	0.0673
660	0.4421	6.18	2.06	3.9	1.37	0.0689
665	0.4503	6.235	2.08	3.91	1.37	0.0705
670	0.4585	6.29	2.1	3.93	1.37	0.0721
675	0.4669	6.345	2.12	3.94	1.37	0.074
680	0.4755	6.4	2.12	3.97	1.37	0.0759
685	0.4842	6.455	2.13	4	1.37	0.0778
690	0.4930	6.51	2.14	4.01	1.37	0.0797
695	0.5020	6.565	2.16	4.03	1.37	0.0816
700	0.5111	6.62	2.18	4.05	1.37	0.0835
705	0.5204	6.675	2.2	4.09	1.37	0.0854
710	0.5298	6.73	2.21	4.1	1.37	0.0873
715	0.5394	6.785	2.22	4.12	1.37	0.0892
720	0.5491	6.84	2.25	4.13	1.37	0.0911

725	0.5590	6.895	2.26	4.17	1.37	0.093
730	0.5690	6.95	2.28	4.18	1.37	0.0949
735	0.5792	7.005	2.3	4.2	1.37	0.0968
740	0.5895	7.06	2.32	4.21	1.37	0.0987
745	0.6000	7.115	2.33	4.22	1.37	0.1006
750	0.6107	7.17	2.34	4.23	1.37	0.1025
755	0.6215	7.225	2.35	4.25	1.37	0.1044
760	0.6325	7.28	2.36	4.26	1.37	0.1063
765	0.6437	7.335	2.38	4.3	1.37	0.109
770	0.6550	7.39	2.4	4.3	1.37	0.11074
775	0.6665	7.445	2.43	4.31	1.37	0.1128
780	0.6781	7.5	2.44	4.32	1.37	0.11486
785	0.6899	7.555	2.45	4.36	1.37	0.11692
790	0.7019	7.61	2.47	4.4	1.37	0.11898
795	0.7141	7.665	2.48	4.41	1.37	0.12104
800	0.7264	7.72	2.5	4.42	1.37	0.1231
805	0.7389	7.775	2.5	4.44	1.37	0.12516
810	0.7516	7.83	2.5	4.45	1.37	0.12722
815	0.7645	7.885	2.5	4.46	1.37	0.12928
820	0.7775	7.94	2.5	4.46	1.37	0.13134
825	0.7908	7.995	2.53	4.47	1.37	0.1334
830	0.8042	8.05	2.54	4.5	1.37	0.13546
835	0.8178	8.105	2.55	4.51	1.37	0.13752
840	0.8315	8.16	2.56	4.52	1.37	0.13958
845	0.8455	8.215	2.58	4.54	1.37	0.14164
850	0.8596	8.27	2.6	4.55	1.37	0.1437
855	0.8740	8.325	2.6	4.58	1.37	0.14576
860	0.8885	8.38	2.61	4.6	1.37	0.14782
865	0.9032	8.435	2.62	4.6	1.37	0.14988
870	0.9181	8.49	2.63	4.6	1.37	0.15194
875	0.9332	8.545	2.64	4.6	1.37	0.154
880	0.9485	8.6	2.64	4.6	1.37	0.15606
885	0.9640	8.655	2.65	4.63	1.37	0.15812
890	0.9797	8.71	2.65	4.63	1.37	0.16018
895	0.9956	8.765	2.65	4.63	1.37	0.16224
900	1.0117	8.82	2.65	4.63	1.37	0.1643

References:
Mg – Filmetrics Corporation of San Diego, California 2002
Al – Filmetrics Corporation of San Diego, California 2002
PEDOT:PSS – Dennler et al., 2007

Wavelength, nm	**CuPc**		**C60**		**SnPc**		**P3HT:PCBM**	
	n	***k***	***n***	***k***	***n***	***k***	***n***	***k***
305	1.62	0.25	2.25	0.7	1.7	0.18	1.82	1.92
310	1.64	0.29	2.2	0.63	1.7	0.2	1.83	1.916
315	1.68	0.34	2.15	0.57	1.75	0.21	1.835	1.91
320	1.73	0.38	2.1	0.55	1.8	0.23	1.83	1.904
325	1.8	0.42	2.08	0.58	1.85	0.25	1.825	1.878
330	1.9	0.45	2.05	0.65	1.9	0.27	1.81	1.87
335	1.95	0.48	2.02	0.73	1.95	0.28	1.8	1.86
340	2	0.49	2.025	0.79	2	0.295	1.785	1.852
345	2.02	0.49	2.035	0.82	2.1	0.31	1.77	1.846
350	2.05	0.48	2.1	0.84	2.2	0.315	1.76	1.847
355	2.1	0.47	2.3	0.75	2.21	0.308	1.74	1.848
360	2.15	0.45	2.425	0.65	2.22	0.3	1.72	1.855
365	2.2	0.41	2.47	0.58	2.23	0.285	1.716	1.862
370	2.25	0.38	2.49	0.5	2.23	0.27	1.71	1.88

375	2.22	0.32	2.47	0.43	2.23	0.25	1.7	1.906
380	2.2	0.28	2.425	0.375	2.25	0.22	1.69	1.915
385	2.17	0.22	2.38	0.34	2.26	0.2	1.68	1.923
390	2.13	0.18	2.35	0.32	2.28	0.17	1.674	1.93
395	2.05	0.13	2.32	0.3	2.29	0.15	1.67	1.942
400	2	0.1	2.29	0.29	2.3	0.12	1.66	1.956
405	1.98	0.09	2.26	0.285	2.33	0.1	1.65	1.957
410	1.93	0.08	2.24	0.29	2.37	0.08	1.64	1.958
415	1.92	0.07	2.22	0.295	2.4	0.06	1.64	1.955
420	1.9	0.06	2.2	0.3	2.43	0.04	1.63	1.95
425	1.86	0.05	2.19	0.31	2.47	0.02	1.63	1.945
430	1.84	0.04	2.18	0.32	2.49	0.011	1.62	1.94
435	1.81	0.03	2.19	0.325	2.52	0.009	1.6	1.92
440	1.79	0.02	2.2	0.33	2.56	0.004	1.57	1.904
445	1.77	0.02	2.21	0.34	2.58	0.002	1.54	1.89
450	1.75	0.01	2.22	0.33	2.6	0	1.5	1.87
455	1.73	0.01	2.235	0.32	2.59	0	1.45	1.86
460	1.72	0.005	2.25	0.31	2.55	0.002	1.43	1.846
465	1.7	0.005	2.255	0.305	2.5	0.004	1.35	1.83
470	1.69	0	2.262	0.295	2.48	0.006	1.28	1.81
475	1.68	0	2.268	0.285	2.44	0.008	1.24	1.8
480	1.66	0	2.27	0.275	2.4	0.01	1.15	1.81
485	1.64	0	2.275	0.26	2.36	0.014	1.07	1.82
490	1.63	0	2.28	0.245	2.31	0.017	1	1.83
495	1.61	0	2.29	0.23	2.29	0.022	0.916	1.84
500	1.6	0	2.3	0.21	2.25	0.025	0.85	1.88
505	1.59	0.005	2.3	0.19	2.22	0.028	0.75	1.93
510	1.57	0.009	2.3	0.17	2.2	0.032	0.7	1.99
515	1.55	0.01	2.3	0.16	2.18	0.036	0.608	2.12
520	1.52	0.015	2.3	0.145	2.16	0.041	0.54	2.25
525	1.5	0.02	2.285	0.13	2.14	0.046	0.5	2.35
530	1.48	0.04	2.277	0.115	2.13	0.053	0.47	2.42
535	1.46	0.06	2.26	0.095	2.1	0.058	0.43	2.48
540	1.42	0.08	2.25	0.075	2.08	0.062	0.402	2.54
545	1.3	0.1	2.244	0.07	2.06	0.065	0.38	2.62
550	1.28	0.13	2.235	0.06	2.04	0.071	0.36	2.7
555	1.28	0.17	2.22	0.0575	2.02	0.074	0.34	2.78
560	1.32	0.21	2.2	0.055	2	0.075	0.32	2.84
565	1.37	0.25	2.192	0.0525	1.98	0.077	0.3	2.88
570	1.42	0.29	2.184	0.05	1.96	0.08	0.28	2.89
575	1.47	0.34	2.177	0.0475	1.95	0.083	0.26	2.9
580	1.53	0.38	2.17	0.047	1.94	0.086	0.25	2.92
585	1.58	0.44	2.167	0.0465	1.93	0.089	0.24	2.93
590	1.62	0.48	2.161	0.046	1.92	0.092	0.23	2.95
595	1.67	0.55	2.156	0.0452	1.91	0.095	0.22	2.96
600	1.77	0.62	2.15	0.044	1.9	0.1	0.21	2.97
605	1.83	0.67	2.15	0.043	1.91	0.11	0.2	2.99
610	1.85	0.73	2.15	0.042	1.925	0.12	0.2	3
615	1.92	0.78	2.15	0.04	1.94	0.13	0.19	3.01
620	2	0.79	2.15	0.039	1.98	0.14	0.19	3.03
625	2.1	0.8	2.15	0.0375	2	0.15	0.18	3.05
630	2.2	0.79	2.15	0.035	2.1	0.165	0.18	3.08
635	2.24	0.77	2.15	0.031	2.17	0.18	0.17	3.1
640	2.25	0.75	2.15	0.028	2.25	0.19	0.17	3.12
645	2.24	0.73	2.145	0.024	2.33	0.2	0.165	3.14
650	2.23	0.7	2.14	0.02	2.4	0.215	0.166	3.15
655	2.2	0.67	2.135	0.018	2.45	0.23	0.165	3.2
660	2.18	0.65	2.125	0.016	2.5	0.245	0.165	3.3
665	2.16	0.6	2.12	0.014	2.55	0.26	0.164	3.4
670	2.13	0.58	2.115	0.013	2.6	0.275	0.163	3.5
675	2.125	0.57	2.1	0.012	2.65	0.285	0.163	3.6

680	2.13	0.57	2.1	0.01	2.7	0.295	0.162	3.7
685	2.18	0.57	2.1	0.008	2.75	0.305	0.161	3.75
690	2.21	0.58	2.1	0.006	2.8	0.315	0.16	3.8
695	2.23	0.61	2.1	0.004	2.85	0.322	0.161	3.85
700	2.25	0.625	2.1	0.0025	2.9	0.33	0.161	3.9
705	2.28	0.625	2.095	0.002	2.94	0.34	0.162	4
710	2.31	0.62	2.09	0.0015	2.98	0.35	0.162	4.1
715	2.38	0.6	2.085	0.001	3.02	0.36	0.163	4.15
720	2.41	0.57	2.08	0.0005	3.06	0.37	0.163	4.2
725	2.45	0.52	2.075	0	3.1	0.37	0.164	4.28
730	2.47	0.45	2.07	0	3.13	0.365	0.164	4.35
735	2.5	0.39	2.065	0	3.16	0.365	0.165	4.4
740	2.52	0.33	2.06	0	3.18	0.36	0.166	4.45
745	2.53	0.28	2.058	0	3.2	0.35	0.167	4.5
750	2.5	0.25	2.056	0	3.2	0.34	0.168	4.6
755	2.48	0.22	2.054	0	3.24	0.33	0.169	4.65
760	2.43	0.2	2.05	0	3.28	0.32	0.17	4.7
765	2.42	0.18	2.05	0	3.32	0.3	0.1715	4.75
770	2.4	0.15	2.05	0	3.4	0.28	0.173	4.8
775	2.38	0.12	2.05	0	3.45	0.26	0.174	4.86
780	2.33	0.1	2.05	0	3.5	0.25	0.175	4.9
785	2.3	0.1	2.049	0	3.55	0.24	0.176	4.95
790	2.28	0.1	2.048	0	3.6	0.23	0.177	5
795	2.26	0.1	2.046	0	3.65	0.22	0.179	5.05
800	2.25	0.1	2.045	0	3.7	0.215	0.18	5.1
805	2.22	0.1	2.044	0	3.75	0.215	0.181	5.15
810	2.2	0.1	2.042	0	3.8	0.22	0.183	5.2
815	2.18	0.1	2.041	0	3.85	0.225	0.185	5.25
820	2.16	0.1	2.04	0	3.9	0.235	0.186	5.3
825	2.14	0.1	2.038	0	3.95	0.24	0.188	5.39
830	2.12	0.1	2.035	0	4.05	0.25	0.189	5.45
835	2.11	0.1	2.033	0	4.1	0.255	0.19	5.5
840	2.1	0.1	2.03	0	4.15	0.26	0.192	5.53
845	2.08	0.1	2.028	0	4.2	0.27	0.194	5.58
850	2.07	0.1	2.025	0	4.3	0.2625	0.195	5.62
855	2.05	0.1	2.023	0	4.35	0.26	0.196	5.66
860	2.05	0.1	2.02	0	4.45	0.26	0.197	5.67
865	2.05	0.1	2.017	0	4.5	0.26	0.198	5.72
870	2.05	0.1	2.015	0	4.55	0.255	0.199	5.75
875	2.05	0.1	2.013	0	4.6	0.255	0.2	5.79
880	2.04	0.1	2.01	0	4.65	0.25	0.205	5.82
885	2.03	0.1	2.008	0	4.7	0.245	0.21	5.88
890	2.02	0.1	2.005	0	4.75	0.24	0.215	5.92
895	2.01	0.1	2.002	0	4.8	0.23	0.22	5.96
900	2	0.1	2	0	4.85	0.225	0.225	6

References:
CuPc – Pettersson et al., 1999
C60 – Rand et al., 2004
SnPc – El-Nahass,Yaghmour, 2008
P3HT:PCBM – Dennler et al., 2007

Materials that are modeled with a non-dispersion refractive index are ($\tilde{n} = n + ik$):

BCP: $\tilde{n} = 1.8$; Alq$_3$: $\tilde{n} = 1.7$; TiOx: $\tilde{n} = 1.8$; MoO3: $\tilde{n} = 1.8$; MgF: $\tilde{n} = 1.35$; SnO: $\tilde{n} = 2.2$; Glass: $\tilde{n} = 1.42$;

II. Summary of the organic photovoltaic devices considered in each chapter

	STRUCTURE	$L_{D,C60}$	$L_{D,CuPc}$	j_{SC} Modeled	j_{SC} Exp.	j_{SC} Coating	Error, % model v exp
CHAPTER 1	No devices introduced						
Chapter 2 1 PLANAR	glass-ITO-CuPc-C60-BCP-Ag inf-1500-200-400-70-1000	160	57	5.08	NA	NA	NA
Ch. 3 / Ch. 4 2 PLANAR	glass-ITO-CuPc-C60-BCP-Ag inf - 1500 - 240 - 380 - 50 - 900	160	90	6.41	6.58	6.54	2.58
3 PLANAR	glass-Ag-CuPc-C60-BCP-Ag inf - 100 - 240 - 380 - 50 - 900	160	90	5.92	5.66	6.7	4.59
4 PLANAR	glass-ITO-P3HT:PCBM-Ag inf - 1500 - 1000 - 1000	NA	NA	7.86	NA	NA	NA
5 PLANAR	Ag - BCP - C60 - CuPc - Au - Mg:Au 125 - 80 - 380 - 240 - 600 - 200	160	90	3.79	3.65	NA	3.84
6 PLANAR	Ag-Al-C60-CuPc-Ni-Al-Si 80 - 30 - 500 - 150 - 50 - 700	NA	NA	NA	NA	NA	NA
Ch. 5 / Ch. 6 7 PLANAR	Glass-ITO-CuPc-C60-BCP-Alq3-Mg:Ag-Ag inf - 1500 - 240 - 380 - 70 - 55 - 650	200	115	NA	4.41	NA	NA
8 PLANAR	Ag-Mg:Ag-Alq3-C60-CuPc-Au-Mg:Au 5 - 6.5 - 7 - 40 - 25 - 65 - 50	200	115	3.29	3.33	4.95	1.20
9 FIBER	Ag-Mg:Ag-Alq3-C60-CuPc-Au-Mg:Au 5 - 6.5 - 7 - 40 - 25 - 65 - 50	200	115	2.87	2.72	4.33	5.51

Continued on the next page

	STRUCTURE	**$L_{D,C60}$**	**$L_{D,CuPc}$**	**j_{SC} Modeled**	**j_{SC} Exp.**	**j_{SC} Coating**	**Error, % model v exp**
	Enhanced devices						
10 PLANAR	Ag-BCP-C60-CuPc-TiOx-Ag-polyimide 100 - 300 - 300 - 150 - 200 - 1000	200	115	8.06	NA	8.97	NA
11 FIBER	Ag-BCP-C60-CuPc-TiOx-Ag-polyimide 100 - 300 - 300 - 150 - 200 – 1000	200	115	7.22	NA	7.97	NA
12 PLANAR	glass-ITO-CuPc-C60-BCP-Ag inf - 1500 - 150 - 300 - 400 - 1000	200	115	8.42	NA	8.7	NA
	Bundled Fibers						
FIBERS	**Device structure - No. 9**						
13	1 row	200	115	3.58	NA	4.86	NA
14	2 rows	200	115	4.36	NA	5.43	NA
15	3 rows	200	115	4.47	NA	5.47	NA
16	10 rows	200	115	5.31	NA	5.82	NA
	Device structure - No. 11						
17	1 row	200	115	8.66	NA	9.42	NA
18	2 rows	200	115	10.31	NA	11.04	NA
19	3 rows	200	115	10.54	NA	11.23	NA
20	10 rows	200	115	12.27	NA	12.64	NA
Chapter 7	Fiber OLED – No OPV cells						
Chapter 8	Conclusions - No new OPV cells						

REFERENCES

Agrawal, M. (2008). *Photonic Design for Efficient Solid-State Energy Conversion*. Stanford University, Stanford. *Thesis*

Agrawal, M. & Peumans, P. (2008). Broadband optical absorption enhancement through coherent light trapping in thin-film photovoltaic cells. *Optics Express*, *16*(8), 5385-5396.

Ahlswede, E., Muhleisen, W., Wahi, M. W. B. M., Hanisch, J., & Powalla, M. (2008). Highly efficient organic solar cells with printable low-cost transparent contacts. *Applied Physics Letters*, *92*(14), 143307.

Al-Ibrahim, M., Sensfuss, S., Uziel, J., Ecke, G., & Ambacher, O. (2005). Comparison of normal and inverse poly(3-hexylthiophene)/fullerene solar cell architectures. *Solar Energy Materials and Solar Cells*, *85*(2), 277-283.

An, K. H., B., O. C., Pipe, K. P., & M., S. (2009). Organic photodetector with spectral response tunable across the visible spectrum by means of internal optical microcavity. *Organic Electronics*, *In Press*.

Anderson., K. (2008). Import Trends in the U.S. Textile and Apparel Industries. http://www.techexchange.com/thelibrary/importtrends.html

Ashcroft, N. M., D. (1976). *Solid State Physics*. Philadelphia: WB Saunders.

Baldo, M. A. & Forrest, S. R. (2001). Interface-limited injection in amorphous organic semiconductors. *Physical Review B*, *64*(8), 085201.

Bayindir, M., Sorin, F., Abouraddy, A. F., Viens, J., Hart, S. D., Joannopoulos, J. D., et al. (2004). Metal-insulator-semiconductor optoelectronic fibres. *Nature*, *431*(7010), 826-829.

Bernede, J. C., Berredjem, Y., Cattin, L., & Morsli, M. (2008). Improvement of organic solar cell performances using a zinc oxide anode coated by an ultrathin metallic layer. *Applied Physics Letters*, *92*(8), 083304.

Bishop, C. A. (2007). *Vacuum Deposition onto Webs, Films, and Foils*. Norwich: William Andrew Publishing.

Brabec, C. J. & Durrant, J. R. (2008). Solution-processed organic solar cells. *MRS Bulletin*, *33*(7), 670-675.

Bulovic, V., Khalfin, V. B., Gu, G., Burrows, P. E., Garbuzov, D. Z., & Forrest, S. R. (1998). Weak microcavity effects in organic light-emitting devices. *Physical Review B*, *58*(7), 3730-3740.

Burrows, P. E., Graff, G. L., Gross, M. E., Martin, P. M., Shi, M. K., Hall, M., et al. (2001). Ultra barrier flexible substrates for flat panel displays. *Displays*, *22*(2), 65-69.

Cairns, D. R. & Crawford, G. P. (2005). Electrochemical properties of transparent conducting substrates for flexible electronic displays. *Proceedings Of The Ieee*, *93*(8), 1451-1458.

Camacho, J. M. & Oliva, A. I. (2006). Surface and grain boundary contributions in the electrical resistivity of metallic nanofilms. *Thin solid films*, *515*(4), 1881-1885.

Cerac, Inc. www.cerac.com/. Retrieved 2008.

Cheung, C. H., Djurisic, A. B., Kwong, C. Y., Tam, H. L., Cheah, K. W., Liu, Z. T., et al. (2004). Change of the emission spectra in organic light-emitting diodes by layer thickness modification. *Applied Physics Letters*, *85*(14), 2944-2946.

Cheyns, D., Poortmans, J., Heremans, P., Deibel, C., Verlaak, S., Rand, B. P., et al. (2008a). Analytical model for the open-circuit voltage and its associated resistance in organic planar heterojunction solar cells. *Physical Review B*, *77*(16).

Cheyns, D., Rand, B. P., Verreet, B., Genoe, J., Poortmans, J., & Heremans, P. (2008b). The angular response of ultrathin film organic solar cells. *Applied Physics Letters*, *92*(24), 243310.

Choi, S. H., Park, Y. H., Lee, C. J., Moon, D. G., Kang, J., Oh, M. H., et al. (2007). Hybrid Passivation for a Flim-like Organic Light-Emitting Diode using Parylene and Silicon Dioxide. *Japanese Journal Of Applied Physics*, *46*(2), 810-814.

Coakley, K. M. & McGehee, M. D. (2004). Conjugated polymer photovoltaic cells. *Chemistry Of Materials*, *16*(23), 4533-4542.

Crispin, X. (2004). Interface dipole at organic/metal interfaces and organic solar cells. *Solar Energy Materials and Solar Cells*, *83*(2-3), 147-168.

Dennler, G., Forberich, K., Scharber, M. C., Brabec, C. J., Tomis, I., Hingerl, K., et al. (2007). Angle dependence of external and internal quantum efficiencies in bulk-heterojunction organic solar cells. *Journal of Applied Physics*, *102*(5), 054516.

Devries, J. W. C. (1988). Temperature and thickness dependence of the resistivity of thin polycrystalline aluminum, cobalt, nickel, palladium, silver and gold films. *Thin Solid Films*, *167*(1-2), 25-32.

Dobrowolski, J. A., Tikhonravov, A. V., Trubetskov, M. K., Sullivan, B. T., & Verly, P. G. (1996). Optimal single-band normal-incidence antireflection coatings. *Applied Optics*, *35*(4), 644-658.

El-Nahass, M. M. & Yaghmour, S. (2008). Effect of annealing temperature on the optical properties of thermally evaporated tin phthalocyanine thin films. *Applied Surface Science*, *255*(5), 1631-1636.

Fan, X., Chu, Z. Z., Wang, F. Z., Zhang, C., Chen, L., Tang, Y. W., et al. (2008). Wire-shaped flexible dye-sensitized solar cells. *Advanced Materials*, *20*(3), 592.

Filmetrics Corporation (2002). Filmetrics Corporation, San Diego.

Forrest, S. R. (1997). Ultrathin organic films grown by organic molecular beam deposition and related techniques. *Chemical Reviews Chem. Rev*, *97*(6), 1793-1896.

Forrest, S. R. (2005). The limits to organic photovoltaic cell efficiency. *Mrs Bulletin*, *30*(1), 28-32.

Forrest, S. R., Bradley, D. D. C., & Thompson, M. E. (2003). Measuring the efficiency of organic light-emitting devices. *Advanced Materials*, *15*(13), 1043-1048.

Fortunato, E., Ginley, D., Hosono, H., & Paine, D. C. (2007). Transparent conducting oxides for photovoltaics. *MRS Bulletin*, *32*(3), 242-247.

Ghosh, A. P., Gerenser, L. J., Jarman, C. M., & Fornalik, J. E. (2005). Thin-film encapsulation of organic light-emitting devices. *Applied Physics Letters*, *86*(22).

Gorgoi, M. & Zahn, D. R. T. (2006). Charge-transfer at silver/phthalocyanines interfaces. *Applied Surface Science*, *252*(15), 5453-5456.

Grzadziel, L., Zak, J., & Szuber, J. (2003). On the correlation between morphology and electronic properties of copper phthalocyanine (CuPc) thin films. *Thin Solid Films*, *436*(1), 70-75.

Harold, P. (2006). Creating a magic lighting experience with textile. *Password: Philips Research technology magazine* 28(7).

Hatton, R. A., Willis, M. R., Chesters, M. A., & Briggs, D. (2003). A robust ultrathin, transparent gold electrode tailored for hole injection into organic light-emitting diodes. *Journal of Materials Chemistry*, *13*(4), 722-726.

Heavens, O. S. (1965). *Optcal properties of thin solid flms*. New York: Dover Publication, Inc.

Ishikawa, K., Wen, C. J., Yamada, K., & Okubo, T. (2004). The photocurrent of dye-sensitized solar cells enhanced by the surface plasmon resonance. *Journal Of Chemical Engineering Of Japan*, *37*(5), 645-649.

Kazmerski, L., Gwinner, D., Hicks, A., NREL (2007): www.nrel.gov/pv/thin_film/docs/kaz_best_research_cell.ppt

Kanno, H., Sun, Y., & Forrest, S. R. (2005). High-efficiency top-emissive white-light-emitting organic electrophosphorescent devices. *Applied Physics Letters*, *86*(26).

Kang, M.G., Kim, M.S., Kim, J., Guo J.L. (2008). Organic solar cells using nanoimprinted transparent metal electrodes. *Advanced Materials*, 20, 4408-4413.

Kawano, K., Pacios, R., Poplavskyy, D., Nelson, J., Bradley, D. D. C., & Durrant, J. R. (2006). Degradation of organic solar cells due to air exposure. *Solar Energy Materials and Solar Cells*, *90*(20), 3520-3530.

Kim, C. & Kim, J. (2008). Organic photovoltaic cell in lateral-tandem configuration employing continuously-tuned microcavity sub-cells. *Optics Express*, *16*(24), 19987-19994.

Kim, J. Y., Kim, S. H., Lee, H. H., Lee, K., Ma, W. L., Gong, X., et al. (2006). New architecture for high-efficiency polymer photovoltaic cells using solution-based titanium oxide as an optical spacer. *Advanced Materials*, *18*(5), 572.

Kim, J. Y., Lee, K., Coates, N. E., Moses, D., Nguyen, T. Q., Dante, M., et al. (2007). Efficient tandem polymer solar cells fabricated by all-solution processing. *Science*, *317*(5835), 222-225.

Klauk, H., Huang, J. R., Nichols, J. A., & Jackson, T. N. (2000). Ion-beam-deposited ultrathin transparent metal contacts. *Thin Solid Films*, *366*(1-2), 272-278.

Kuraseko, H., Nakamura, T., Toda, S., Koaizawa, H., Jia, H., & Kondo, M. (2006). Development of flexible fiber-type poly-Si solar cell. *Conference Record of the 2006 IEEE 4th World Conference on Photovoltaic Energy Conversion, Vols 1 and 2,* 1380-1383.

Lee, J. B. & Subramanian, V. (2005). Weave patterned organic transistors on fiber for e-textiles. *Ieee Transactions On Electron Devices*, *52*(2), 269-275.

Lee, J. Y., Connor, S. T., Cui, Y., & Peumans, P. (2008). Solution-processed metal nanowire mesh transparent electrodes. *Nano Letters*, *8*(2), 689-692.

Lee, M. R., Eckert, R. D., Forberich, K., Dennler, G., Brabec, C. J., & Gaudiana, R. A. (2009). Solar Power Wires Based on Organic Photovoltaic Materials. *Science*, *324*(5924), 232-235.

Lewis, J., Grego, S., Chalamala, B., Vick, E., & Temple, D. (2004). Highly flexible transparent electrodes for organic light-emitting diode-based displays. *Applied Physics Letters*, *85*(16), 3450-3452.

Lewis, N. Accessed 2009, http://nsl.caltech.edu/energy.html

Li, Y. Q., Tang, J. X., Xie, Z. Y., Hung, L. S., & Lau, S. S. (2004). An efficient organic light-emitting diode with silver electrodes. *Chemical Physics Letters*, *386*(1-3), 128-131.

Lissberger, P.H. (1970). Optical applications of dielectric thin films. Reports on Progress in physics *33*(3), 197.

Liu, J. W., Namboothiry, M. A. G., & Carroll, D. L. (2007). Fiber-based architectures for organic photovoltaics. *Applied Physics Letters*, *90*(6), 063501.

Lopez-Hernandez, F. J., Perez-Jimenez, R., & Santamaria, A. (2000). Ray-tracing algorithms for fast calculation of the channel impulse response on diffuse IR wireless indoor channels. *Optical Engineering*, *39*(10), 2775-2780.

Lu, M. H. & Sturm, J. C. (2002). Optimization of external coupling and light emission in organic light-emitting devices: modeling and experiment. *Journal Of Applied Physics*, *91*(2), 595-604.

Lupton, J. M., Matterson, B. J., Samuel, I. D. W., Jory, M. J., & Barnes, W. L. (2000). Bragg scattering from periodically microstructured light emitting diodes. *Applied Physics Letters*, *77*(21), 3340-3342.

Mapel, J. K., Singh, M., Baldo, M. A., & Celebi, K. (2007). Plasmonic excitation of organic double heterostructure solar cells. *Applied Physics Letters*, *90*(12), 121102.

Marculescu, D., Marculescu, R., Zamora, N. H., Stanley-Marbell, P., Khosla, P. K., Park, S., et al. (2003). Electronic textiles: A platform for pervasive computing. *Proceedings Of The IEEE*, *91*(12), 1995-2018.

Mayadas, A. F., Shatzkes, M., & Janak, J. F. (1969). Electrical Resistivity Model For Polycrystalline Films - Case Of Specular Reflection At External Surfaces. *Applied Physics Letters*, *14*(11), 345-&.

Molodtsova, O. V., Aristov, V. Y., Zhilin, V. M., Ossipyan, Y. A., Vyalikh, D. V., Doyle, B. P., et al. (2007). Silver on copper phthalocyanine: Abrupt and inert interfaces. *Applied Surface Science*, *254*(1), 99-102.

Navigant Consulting Inc., R. A., Inc. and SSLS, Inc. (2009). Solid State Lighting Research and Development, Multi-Year Program Plan., 193.

Nelson, J. (2003). *The Physics of Solar Cells*. London: Imperial College Press.

Neyts, K. (2005). Microcavity effects and the outcoupling of light in displays and lighting applications based on thin emitting films. *Applied Surface Science*, *244*(1-4), 517-523.

Noge, S., Ueno, H., Hohkawa K., Yoshikawa S., (1995). Low resistance thin Al film simple sputtering deposition. *IEEE Ultrasonic Symposium,* 379.

O'Connor, B., An, K. H., Pipe, K. P., Zhao, Y., & Shtein, M. (2006). Enhanced optical field intensity distribution in organic photovoltaic devices using external coatings. *Applied Physics Letters*, *89*(23), 233502.

O'Connor, B., An, K. H., Zhao, Y., Pipe, K. P., & Shtein, M. (2007). Fiber shaped organic light emitting device. *Advanced Materials*, *19*, 3897.

O'Connor, B., Haughn, C., An, K. H., Pipe, K. P., & Shtein, M. (2008a). Transparent and conductive electrodes based on unpatterned, thin metal films. *Applied Physics Letters*, *93*(22), 223304.

O'Connor, B., Pipe, K. P., & Shtein, M. (2008b). Fiber based organic photovoltaic devices. A*pplied Physics Letters 92*(19), 193306.

Ohta, K., Ishida, H. (1990). Matrix formulism for calculation of electric-field intensity of light in stratified multilayered films. *Applied Optics*, *29*(13), 1952-1959.

Oyamada, T., Sugawara, Y., Terao, Y., Sasabe, H., & Adachi, C. (2007). Top light-harvesting organic solar cell using ultrathin Ag/MgAg layer as anode. *Japanese Journal of Applied Physics, Part 1 - Regular Papers, Brief Communications, and Review Papers*, *46*(4A), 1734-1735.

Panoliaskos, A., Hallett, W.L. H., Garis, I. (1985). Prediction of optical fiber coating thickness. *Applied Optics*, *24*(15), 2309-2312.

Park, S. & Jayaraman, S. (2003). Smart textiles: Wearable electronic systems. *MRS Bulletin*, *28*(8), 585-591.

Pettersson, L. A. A., Roman, L. S., & Inganas, O. (1999). Modeling photocurrent action spectra of photovoltaic devices based on organic thin films. *Journal Of Applied Physics*, *86*(1), 487-496.

Peumans, P. & Forrest, S. R. (2004). Separation of geminate charge-pairs at donor-acceptor interfaces in disordered solids. *Chemical Physics Letters*, *398*(1-3), 27-31.

Peumans, P., Bulovic, V., & Forrest, S. R. (2000). Efficient photon harvesting at high optical intensities in ultrathin organic double-heterostructure photovoltaic diodes. *Applied Physics Letters*, *76*(19), 2650-2652.

Peumans, P. & Forrest, S. R. (2001). Very-high-efficiency double-heterostructure copper phthalocyanine/C-60 photovoltaic cells. *Applied Physics Letters*, *79*(1), 126-128.

Peumans, P., Uchida, S., & Forrest, S. R. (2003a). Efficient bulk heterojunction photovoltaic cells using small-molecular-weight organic thin films. *Nature*, *425*(6954), 158-162.

Peumans, P., Yakimov, A., & Forrest, S. R. (2003b). Small molecular weight organic thin-film photodetectors and solar cells. *Journal Of Applied Physics*, *93*(7), 3693-3723.

Pode, R. B., Lee, C. J., Moon, D. G., & Han, J. I. (2004). Transparent conducting metal electrode for top emission organic light-emitting devices: Ca-Ag double layer. *Applied Physics Letters*, *84*(23), 4614-4616.

Qin, Y., Wang, X. D., & Wang, Z. L. (2008). Microfibre-nanowire hybrid structure for energy scavenging. *Nature*, *451*(7180), 809-U5.

Qiu, C. F., Peng, H. J., Chen, H. Y., Xie, Z. L., Wong, M., & Kwok, H. S. (2004). Top-emitting OLED using praseodymium oxide coated platinum as hole injectors. *IEEE Transactions On Electron Devices*, *51*(7), 1207-1210.

Quaschning, V. & Hanitsch, R. (1996). *Influence of Shading on Electrical Parameters of Solar Cells*. Paper presented at the PVSC.

Rand, B. P., Li, J., Xue, J. G., Holmes, R. J., Thompson, M. E., & Forrest, S. R. (2005). Organic double-heterostructure photovoltaic cells employing thick tris(acetylacetonato)ruthenium(III) exciton-blocking layers. *Advanced Materials*, *17*(22), 2714.

Rand, B. P., Peumans, P., & Forrest, S. R. (2004). Long-range absorption enhancement in organic tandem thin-film solar cells containing silver nanoclusters. *Journal Of Applied Physics*, *96*(12), 7519-7526.

Reilly, T. H., van de Lagemaat, J., Tenent, R. C., Morfa, A. J., & Rowlen, K. L. (2008). Surface-plasmon enhanced transparent electrodes in organic photovoltaics. *Applied Physics Letters*, *92*(24), 243304.

Rentenberger, S., Vollmer, A., Zojer, E., Schennach, R., & Koch, N. (2006). UV/ozone treated Au for air-stable, low hole injection barrier electrodes in organic electronics. *Journal of Applied Physics*, *100*(5), 053701.

Rhee, J. & Lee, H. H. (2002). Patterning organic light-emitting diodes by cathode transfer. *Applied Physics Letters*, *81*(22), 4165-4167.

Riede, M., Mueller, T., Tress, W., Schueppel, R., & Leo, K. (2008). Small-molecule solar cells - status and perspectives. *Nanotechnology*, *19*(42), 424001.

Riel, H., Karg, S., Beierlein, T., Ruhstaller, B., & Riess, W. (2003). Phosphorescent top-emitting organic light-emitting devices with improved light outcoupling. *Applied Physics Letters*, *82*(3), 466-468.

Rim, S.B., and Peumans, P. (2008). The effect of optical interference on exciton diffusion length measurements using photocurrent spectroscopy. *Journal Of Applied Physics*, *101*(12), 124515.

Romanyuk, A., Steiner, R., Mack, I., Oelhafen, P., & Mathys, D. (2007). Growth of thin silver films on silicon oxide pretreated by low temperature argon plasma. *Surface Science*, *601*(4), 1026-1030.

Rowell, M. W., Topinka, M. A., McGehee, M. D., Prall, H. J., Dennler, G., Sariciftci, N. S., et al. (2006). Organic solar cells with carbon nanotube network electrodes. *Applied Physics Letters*, *88*(23), 233506.

Salzman, R. F., Xue, J. G., Rand, B. P., Alexander, A., Thompson, M. E., & Forrest, S. R. (2005). The effects of copper phthalocyanine purity on organic solar cell performance. *Organic Electronics*, *6*(5-6), 242-246.

Schoeser, M. (2003). *World Textiles, A Consise History*. London: Thames & Hudson Ltd.

Schubert, M. B. & Werner, J. H. (2006). Flexible solar cells for clothing. *Materials Today*, *9*(6), 42-50.

Scott, J. C. (2003). Metal-organic interface and charge injection in organic electronic devices. *Journal of Vacuum Science and Technology A*, *21*(3), 521-531.

Shao, Y. & Yang, Y. (2005). Efficient organic heterojunction photovoltaic cells based on triplet materials. *Advanced Materials*, *17*(23), 2841.

Shtein, M., Gossenberger, H. F., Benziger, J. B., & Forrest, S. R. (2001). Material transport regimes and mechanisms for growth of molecular organic thin films using low-pressure organic vapor phase deposition. *Journal Of Applied Physics*, *89*(2), 1470-1476.

Shtein, M., Peumans, P., Benziger, J. B., & Forrest, S. R. (2003). Micropatterning of small molecular weight organic semiconductor thin films using organic vapor phase deposition. *Journal Of Applied Physics*, *93*(7), 4005-4016.

So, F., Kido, J., & Burrows, P. (2008). Organic light-emitting devices for solid-state lighting. *MRS Bulletin*, *33*(7), 663-669.

Sokolik, I., Priestley, R., Walser, A. D., Dorsinville, R., & Teng, C. W. (1996). Bimolecular reactions of singlet excitons in tris(8-hydroxyquinoline) aluminum. *Applied Physics Letters*, *69*(27), 4168-4170.

Song, Q. L., Li, F. Y., Yang, H., Wu, H. R., Wang, X. Z., Zhou, W., et al. (2005). Small-molecule organic solar cells with improved stability. *Chemical Physics Letters*, *416*(1-3), 42-46.

Sullivan, B. T. & Dobrowolski, J. A. (1996). Implementation of a numerical needle method for thin-film design. *Applied Optics*, *35*(28), 5484-5492.

Tachibana, Y., Akiyama, H. Y., & Kuwabata, S. (2007). Optical simulation of transmittance into a nanocrystalline anatase TiO2 film for solar cell applications. *Solar Energy Materials and Solar Cells*, *91*(2-3), 201-206.

Tang, C. W. (1986). 2-Layer Organic Photovoltaic Cell. *Applied Physics Letters*, *48*(2), 183-185.

Terao, Y., Sasabe, H., & Adachi, C. (2007). Correlation of hole mobility, exciton diffusion length, and solar cell characteristics in phthalocyanine/fullerene organic solar cells. *Applied Physics Letters*, *90*(10), 103515.

Tong, X. R., Bailey-Salzman, R. F., Wei, G. D., & Forrest, S. R. (2008). Inverted small molecule organic photovoltaic cells on reflective substrates. *Applied Physics Letters*, *93*(17), 173304.

Tvingstedt, K. & Inganas, O. (2007). Electrode grids for ITO-free organic photovoltaic devices. *Advanced Materials*, *19*(19), 2893.

Vazquez, H., Flores, F., & Kahn, A. (2007). Induced Density of States model for weakly-interacting organic semiconductor interfaces. *Organic Electronics*, *8*, 241-248.

Wang, J., Wang, C. Y., Too, C. O., & Wallace, G. G. (2006). Highly-flexible fibre battery incorporating polypyrrole cathode and carbon nanotubes anode. *Journal of Power Sources*, *161*(2), 1458-1462.

Wang, X., Zhi, L. J., Tsao, N., Tomovic, Z., Li, J. L., & Mullen, K. (2008). Transparent carbon films as electrodes in organic solar cells. *Angewandte Chemie-international Edition*, *47*(16), 2990-2992.

Wasey, J. A. E. & Barnes, W. L. (2000). Efficiency of spontaneous emission from planar microcavities. *Journal Of Modern Optics*, *47*(4), 725-741.

Worthing, P. T., Amos, R. M., & Barnes, W. L. (1999). Modification of the spontaneous emission rate of Eu3+ ions embedded within a dielectric layer above a silver mirror. *Physical Review A*, *59*(1), 865-872.

Wu, J. B., Becerril, H. A., Bao, Z. N., Liu, Z. F., Chen, Y. S., & Peumans, P. (2008). Organic solar cells with solution-processed graphene transparent electrodes. *Applied Physics Letters*, *92*(26), 263302.

Xue, J. G., Uchida, S., Rand, B. P., & Forrest, S. R. (2004). 4.2% efficient organic photovoltaic cells with low series resistances. *Applied Physics Letters*, *84*(16), 3013-3015.

Yadav, A., Shtein, M., & Pipe, K. P. (2008). Fiber-based flexible thermoelectric power generator. *Journal of Power Sources*, *175*, 909-913.

Yamashita, K., Mori, T., & Mizutani, T. (2001). Encapsulation of organic light-emitting diode using thermal chemical-vapour-deposition polymer film. *Journal Of Physics D-Applied Physics*, *34*(5), 740-743.

Yang, F. & Forrest, S. R. (2006). Organic solar cells using transparent SnO2-F anodes. *Advanced Materials*, *18*(15), 2018.

Zhang, W., Brongersma, S. H., Richard, O., Brijs, B., Palmans, R., Froyen, L., et al. (2004). Influence of the electron mean free path on the resistivity of thin metal films. *Microelectronic Engineering*, *76*(1-4), 146-152.

Zhou, Y. H., Zhang, F. L., Tvingstedt, K., Barrau, S., Li, F. H., Tian, W. J., et al. (2008). Investigation on polymer anode design for flexible polymer solar cells. *Applied Physics Letters*, *92*(23), 233308.